This electronic thesis or dissertation has been downloaded from the King's Research Portal at https://kclpure.kcl.ac.uk/portal/

Single Molecule Interferometric Imaging of Molecular Assembly

Guo, Yujie

Awarding institution:
King's College London

The copyright of this thesis rests with the author and no quotation from it or information derived from it may be published without proper acknowledgement.

END USER LICENCE AGREEMENT

Unless another licence is stated on the immediately following page this work is licensed under a Creative Commons Attribution-NonCommercial-NoDerivatives 4.0 International licence. https://creativecommons.org/licenses/by-nc-nd/4.0/

You are free to copy, distribute and transmit the work

Under the following conditions:

- Attribution: You must attribute the work in the manner specified by the author (but not in any way that suggests that they endorse you or your use of the work).
- Non Commercial: You may not use this work for commercial purposes.
- No Derivative Works - You may not alter, transform, or build upon this work.

Any of these conditions can be waived if you receive permission from the author. Your fair dealings and other rights are in no way affected by the above.

Take down policy

If you believe that this document breaches copyright please contact librarypure@kcl.ac.uk providing details, and we will remove access to the work immediately and investigate your claim.

Download date: 13. Jan. 2025

King's College London
Department of Chemistry

Single Molecule Interferometric Imaging of Molecular Assembly

Yujie Guo

Submitted in part fulfilment of the requirements
for the degree of Doctor of Philosophy at
King's College London, December 2023

I composed this thesis in its entirety and have not submitted it for any other academic or professional qualification. I confirm the disclosed research is all my own work, except for instances of jointly-performed experiments for coauthored publications. Information obtained from other sources is acknowledged in each chapter with a list of references.

Yujie Guo (2023)

Acknowledgements

Four years ago, I embarked on a solo journey to the UK, completely unaware that as time unfolded, I would steadily make substantial progress in both my research and life. I owe my deepest thanks to the many incredible people who supported and guided me along the way. This thesis is my way of expressing gratitude and celebrating the friendships I've made, as well as acknowledging the support from the K-CSC program that paved the way for this remarkable journey.

I want to begin by expressing my profound gratitude to my supervisor, Professor Mark Wallace. Throughout my journey, he not only provided invaluable guidance and engaging research projects but also fostered an environment of creativity and freedom. His ability to 'magically turn the lemons given by the research into lemonade' is truly remarkable. From him, I also gained the insight that humor can be a powerful tool in tackling even the most daunting challenges.

I would also like to extend my heartfelt gratitude to Professor Rachel O'Reilly, an outstanding collaborator who has provided me with unwavering support and acknowledged my modest achievements generously.

I also want to acknowledge a group of remarkable colleagues who have not only become cherished friends but have also played indispensable roles in my PhD journey. Dr. Vivien Walter introduced me to the world of iSCAT and Python, generously sharing his knowledge and patiently guiding me through this Ph.D. Beyond our work, I've found great joy in our conversations about sharing and learning about each other's cultures. I have gained valuable insights into French culture, and I am equally excited to share the richness of Chinese culture with him. I would also like to thank Dr. Joanne Carniello, affectionately known as 'Mama Jo,' who kindly took me under her wing when I first joined the lab and continued to do so ever since. I enjoyed our time together, which was the shining day of my research life. Jo also introduced me to my dear dog friend, Harper, who has been a constant source of comfort during challenging times. My gratitude also extends to Dr. Steven Vanuytsel, a delightful and fun person to be around, who has been a reliable friend providing valuable advice. Even though our fields are different, I deeply appreciate the time he willingly invests in discussing my project and helping me overcome challenges. And I want to thank my 'panic buddy', Dr. Daisy Rogers-Simmonds. We supported and encouraged each other through all the challenging times, consistently reassuring one another that everything was fine. Dr. Jason Sengel and Dr.

Eve Weatherill have been instrumental not only in shaping my research experiences but also in acquainting me with British culture, enriching my overall experience in the UK. I want to express my thanks to Dr. Christopher Parperis, who not only made me feel welcomed and included from day one but also offered unwavering support for my project. I would also like to extend my thanks to Lucian Heeler and Kharina Fenton, who have been supportive and inspiring friends. Dr. Pantelitsa Dimitriou and Dr. Christian Bortolini deserve my thanks for their help during the final phases of my PhD, as well as for the enjoyable after-work activities we've shared. I would also like to express my gratitude to Tianlai Xia from Professor O'Reilly's group at the University of Birmingham, who provided invaluable support and advice. My appreciation also extends to every other member of the group for their assistance and support throughout my journey.

My parents are the source of my braveness, they encourage me to explore the best version of myself, to learn more, and to open my mind to embrace the whole world. Because of the effect of COVID-19, I have been away from home for the entire four years, but my parents made me feel home is always close by my side, their support and guidance are always with me from the early morning till the darkest night. My roommate Qi Lin also deserves a special mention for making London feel like home, finishing a Ph.D. overseas takes great courage but her companionship and support made the whole process less hard. In the end, I want to express my gratitude to Yue Yang, Xuemei Ma, and Guiming Han, who have been extraordinary friends over the past few years, infusing my life with happiness and surprises.

Abstract

Single-molecule/particle detection avoids ensemble averaging, providing heterogeneous information that is commonly inaccessible by conventional techniques. For decades, fluorescence microscopy has served as the workhorse for single-molecule/particle detection. However, despite its great ability to push the limits of detection sensitivity down to the nanoscale, this technique is also accompanied by several inherent restrictions. Interferometric scattering (iSCAT) microscopy offers an alternative approach for single-molecule detection without requiring extrinsic labels, with the current research focus primarily on protein biomolecules. This thesis details the implementation of iSCAT as a novel single-molecule technique to study nanoscopic structure and dynamics across different non-biological systems, including polymers and metal nanoparticles.

Chapter 1 introduces single-molecule techniques, summarizing their mechanisms, advantages, and limitations. In this chapter, iSCAT is explicitly reviewed to provide a general background for my study. In Chapter 2, to demonstrate the capability of iSCAT in single particle detection, gold nanoparticles with known size were chosen as an example for iSCAT imaging. A calibration curve (iSCAT contrast *vs.* particle size) was developed, mapping the contrast of individual objects to their properties, such as diameter and mass. With this relationship established, Chapter 3 aims to investigate the kinetics of single polymer chain growth through real-time monitoring of its contrast evolution. Based on the same concept, in Chapter 4, the growth kinetics of individual gold nanoparticles are explored using iSCAT with a distribution of individual nanoparticle rate constants can be extracted. Following this, in Chapter 5, iSCAT was used to successfully observe the self-assembly process of crystallizable polymeric materials and served as a sensitive refractive index microscope to report changes in the optical properties within single nanoplatelets. Finally, Chapter 6 summarizes the work conducted in this thesis and discusses the future applications of iSCAT.

Dedicated to my parents and my dear grandmother

Contents

List of Figures

Nomenclature

List of abbreviations

Đ	dispersity
$M_{\mathbf{n}}$	number average molecular weight
$M_{\mathbf{w}}$	weight average molecular weight
ACM	aminochloromaleimide
AFM	atomic force microscopy
ATRP	atom transfer radical polymerization
AuNP	gold nanoparticle
BCP	block copolymer
BFP	back focal plane
CDSA	crystallization-driven self-assembly
CLSM	confocal laser scanning microscopy
CMOS	complementary metal oxide semiconductor
CRP	controlled radical polymerization
CTA	chain transfer agent
DMA	*N,N*-dimethylacrylamide
HP	homopolymer
iSCAT	interferometric scattering microscope
kDa	kilodalton
LED	light emitting diode
MWD	molecular weight distribution
NIPAM	*N*-isopropylacrylamide
NMR	nuclear magnetic resonance spectroscopy

NP	nanoparticle
P2VP	poly(ε-caprolactone)-*b*-poly(2-vinylpyridine)
Br-PBS	phosphate-buffered saline solution with bromide anions added
PBS	polarizing beam splitter
PCL-*b*-PDMA	poly(ε-caprolactone)-*b*-poly(N,N-dimethylacrylamide)
PCL	poly(ε-caprolactone)
PCPV	poly(cyclopentenylene-vinylene)
PDMA	poly(*N,N*-dimethylacrylamide)
PEG	polyethylene glycol
PICRA	photoinduced initiators for continuous activator regeneration
PNIPAM	poly(*N*-isopropylacrylamide)
QWP	quarter-wave plate
RAFT	reversible addition-fragmentation chain transfer polymerization
ROI	region of interest
SEC	size exclusion chromatography
SLM	spatial light modulator
SNR	signal-to-noise ratio
SP	sodium pyruvate
TEM	transmission electron microscope
THF	tetrahydrofuran
UV	ultraviolet

Chapter 1

Introduction

1.1 Ensemble *vs.* single-molecule techniques

Conventional ensemble techniques, such as spectroscopy and chromatography, have long served as the dominant tools for characterizing a broad range of fundamental processes in physics, chemistry, and biology. However, a significant challenge arises when detecting nanoscopic objects due to the considerable mismatch between object size and the wavelength of detection light, which yields a weak interaction between electromagnetic radiation and matter. Consequently, conventional techniques often hinge on measuring the collective signal produced by a large number of molecules [1]. Unfortunately, this approach suppresses crucial molecular details, such as size variations, kinetic disparities, conformational diversity, and binding affinity heterogeneity, all of which provide deeper insights into the system and remain concealed behind the ensemble averages.

The development of single-molecule techniques enables the detection of physical, chemical as well as biological entities at the nanoscale with extraordinary sensitivity, offering a new approach for these previously 'unanswerable' questions [2]. The broad impact of these advances is clear, with applications in a wide range of topics, including structural information of individual molecules [3–5], single particle tracking [6–8], molecular force and potential measurement [9–11] and molecular dynamics monitoring [12–14].

Although, compared to transmission electron microscopy with a resolution down to a fraction of nanometer, or atomic force microscopy with a resolution determined by its atomic-sized tip, the spatial resolution of optical methods for single-molecule detection is confined by the diffraction to around 200 nm. This barrier can be lifted via ingenious experiment design to achieve super-resolved resolution [15–18]. Meanwhile, as non-invasive optical methods, they are also compatible with a wide variety of observation conditions and have been successfully applied to complex materials varying from living matter to metal nanoparticles. In addition, they exhibit excellent temporal resolution, which allows monitoring of chemical or biological processes in real-time.

The focus of this chapter is to provide a summary of the recent optical techniques that have demonstrated single-molecule detection, with their mechanism, advantages, limitations as well as applications discussed below.

1.2 Fluorescence detection

Using fluorescence as a contrast mechanism allows the first optical detection of single molecules to be achieved at cryogenic temperatures inside a crystalline matrix [19]. Since then, fluorescence microscopy has served as the essential tool for investigating optical phenomena at the single-molecule level. As shown in Fig. 1.1, when an incident light with a specific wavelength encounters a fluorescent object, a specific quantum of light is absorbed, which pushes a valence electron at the ground state (S_0) into a higher energy state (S_1, S_2,..., S_n) for a short time period. Then the electron will undergo vibrational relaxation to reach the lowest level of the excited state (S_1) through a nonradiative process termed as internal conversion. Then the electron returns from S_1 to S_0 via two processes: Radiative and nonradiative, of which the energy is released through light and heat, respectively. As some energy has been consumed during the vibrational relaxation, the emitted fluorescent photon has a lower energy compared to the excitation photon. As a result, the emitted light would exhibit a red shift in its emission profile compared to the excitation profile, which is known as Stokes shift [20–23]. Together with volume reduction, it creates an advantageous opportunity for separating the weak signal produced by a single molecule from the overwhelming background. By applying suitable optical filters, it is possible to achieve a high excitation light rejection ratio of 6 to 10 magnitudes, enabling background-free detection [21, 23, 24].

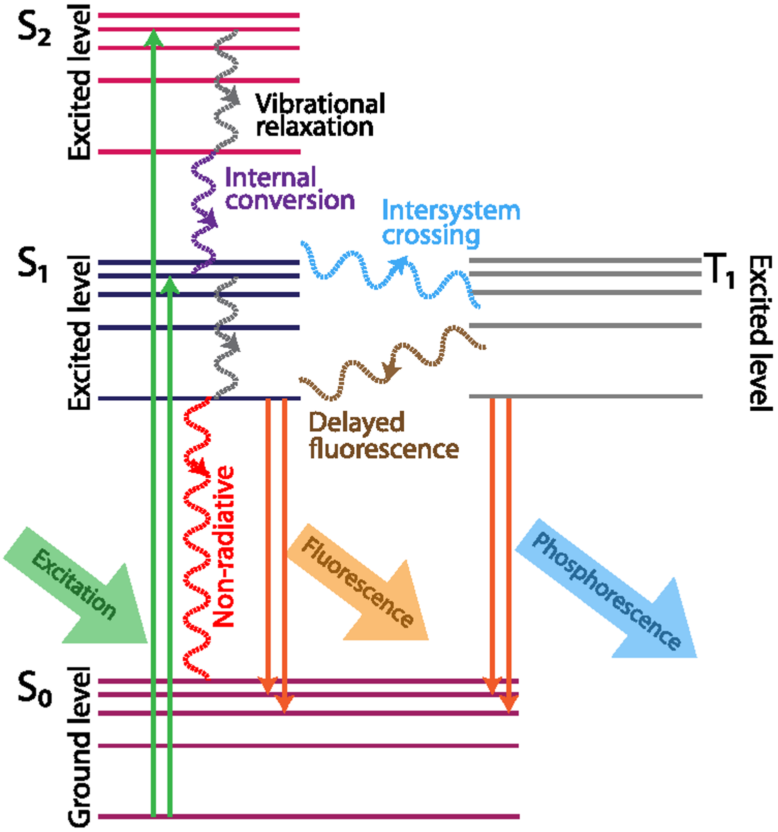

Figure 1.1: **Schematic of Jablonski diagram [20].**

The most common approaches to enhance the signal-to-noise ratio (SNR) are via increasing incident power or prolonging the exposure time to maximize the total number of detected photons. However, these approaches pose hard limits for fluorescence imaging, as photochemically induced photobleaching can cause the fluorescent molecules to be permanently converted to a dark state. These phenomena present great challenges for continuous observations and long-term measurements, making particle tracking and monitoring of dynamic processes problematic. Moreover, optical saturation imposes a hard limit on the maximum rate of photon emission, impacting imaging speed and consequently hindering the applicability of fluorescence imaging in observing dynamic processes. Furthermore, most molecules (e.g., polymers, proteins, and amino acids) are intrinsically non- or weakly fluorescent, requiring laborious fluorescent marker labeling. Most importantly, the use of the label itself may cause changes to the intrinsic properties of the target molecule and interrupt the underlying dynamics of the system under study. In order to overcome these limitations, a range of optical label-free single-molecule techniques have gradually come to the fore.

1.3 Scattering and absorption as a contrast mechanism

Using scattering as a contrast mechanism provides many advantages compared to fluorescent emission, scattering occurs when the refractive index of the object is different from its surrounding medium, thus instead of relying on extrinsic labels, the generation of signals only depends on the inherent properties of the object. This opens up single-molecule detection to a broader spectrum of molecules and effectively circumvents the label-induced limitations (e.g., photobleaching and photon saturation), which are now mainly constrained by light-induced heating.

Dark-field microscopy is a representative technique that is based on using scattering as the imaging scheme. Its efficient signal isolation from the excitation light is based on orthogonal illumination and detection pathways. To be more specific, as shown in Fig. 1.2A, by applying a dark-field condenser lens in the light path, the cone of light can be directed away from the objective lens (this can also be achieved via total-internal reflection mode) [25]. With this setup, dark-field microscopy can generate images with a similar quality as fluorescence microscopy. As shown in Fig. 1.2A and B, both techniques can image the structure of single microtubules [26].

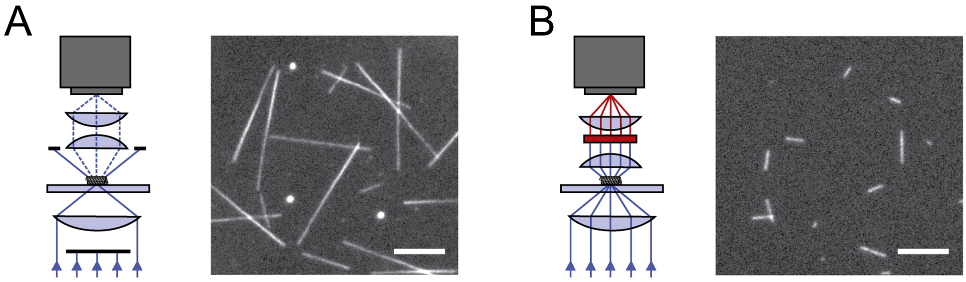

Figure 1.2: **Dark-field and fluorescence microscopy detection of individual microtubules.**
(A) Schematic of a typical dark-field microscope and an example image of individual microtubules acquired using such technique (scale bar: 5 µm). **(B)** Schematic of a fluorescence microscope operating in transmission mode and an example image of fluorescently labeled microtubule seeds (scale bar: 5 µm) [26, 27].

However, due to the variation in the reduction of signal magnitude with object size dark-field microscopy cannot reach similar single-molecule detection sensitivity as fluorescence microscopy does. As in pure scattering-based detection, the scattering cross section drops as the sixth power of the particle diameter [24, 27, 28]. To be more straightforward, assuming each tubulin dimer is labeled with a fluorescent tag, the fluorescence intensity of a microtubule (comprising approximately 300 tubulin dimers) would be 300 times stronger than a single tubulin dimer. But in the dark-field detection, the signal of a single tubulin dimer would drop around 10^5 compared to a microtubule. It is also challenging to pick up such weak signals with the presence of stray light from the sample or any imperfections in the optics.

Besides scattering, light absorption is also a promising imaging scheme to achieve single-molecule/particle detection [29–31]. Among various techniques, photothermal microscopy is the most commonly used method, offering sensitive detection via optically measuring the photothermal heating of single molecules. It is a two-color technique that employs two laser beams in the setup: A heating laser is directed at the absorber, which triggers its transition to an excited state. Then the relaxation of this absorber produces heat, which then diffuses into the local medium environment, creating a thermal lens. The heat-induced local refractive index gradient will be detected through the scattering of the second probe beam [32–35]. The intensity of the heating laser is limited by the photodamage and saturation of the sample, meanwhile, the probe beam is primarily affected by the broadband refractive index variation. As a result, high probe intensities with low photon noise can be attained by selecting a wavelength outside of the spectral absorption range of the absorbing object [33]. To differentiate the signal from the background, the heating laser beam is modulated at a high frequency (in excess of 100 kHz) and the interference signal can be extracted via a lock-in amplifier [32]. In the early 2000s, photothermal microscopy successfully detected single AuNPs down to 2.5 nm [32], followed by the first single-molecule detection a few years after [30]. However, this technique still faces some limitations, as its detection relies on the object of interest absorbing light, the detection of weak/non-absorbing samples is challenging. Additionally, it is commonly used in a confocal configuration, which means its temporal resolution is limited by the scanning rate (integration times of the order of the millisecond per pixel). This significantly limits its applications in real-time monitoring of dynamic processes [28, 36, 37]. Wide-field photothermal microscopy has improved the acquisition rate, but to date, at the expense of some sensitivity [38–40].

1.4 Interference-based microscopy

Introducing another probe beam to interfere with the scattering signal can effectively mitigate the rapid signal loss seen in dark-field microscopy imaging. This is because an interferometric signal scales linearly with object volume, in contrast to the square dependence of pure scattering (signal detected by dark-field microscopy) [41].

Interferometric scattering (iSCAT) microscopy was developed based on this scheme. iSCAT's origins are in interference reflection microscopy developed during the 1960s [42] and was then first coined as iSCAT in the early 2000s [43]. As shown in Fig. 1.3A, a sample supported by a transparent glass coverslip is illuminated by a coherent light source, commonly a laser beam. Some of the incident light is reflected back from the interface between the sample solution and the substrate, which acts as the reference field. The majority of incident light passes through the interface and reaches to the sample. Due to the refractive index difference between the sample and its surrounding medium, a scattering signal is then generated. The signal detected and imaged by the detector is the result of these reflected and scattered signals, which can be expressed as:

$$I_{\mathrm{det}} = |E_{\mathrm{r}} + E_{\mathrm{s}}|^2 = |E_{\mathrm{i}}|^2\{r^2 + |s|^2 - 2r|s|\sin(\varphi)\}, \tag{1.1}$$

where I_{det} represents the detected intensity, E_{i}, E_{s} and E_{r} represent incident, scattered and reflected fields, respectively. r^2 is the reflectivity of the glass-sample interface, φ is the phase shift between scattered and reflected signals. For a spherical particle, the scattering amplitude, s, can be further defined as:

$$s = \eta\alpha = \eta\frac{\pi D^3}{2}\left(\frac{n_{\mathrm{p}}^2 - n_{\mathrm{m}}^2}{n_{\mathrm{p}}^2 + 2n_{\mathrm{m}}^2}\right), \tag{1.2}$$

where η takes into account the detection efficiency, α represents the particle polarizability and can be further expressed by the particle diameter (D), refractive indices of the particle (n_{p})

and the surrounding medium (n_m). By combining these two equations, the advantage of the interferometric detection scheme stands out: the pure scattering term, s^2, which constitutes the dominant signal in dark-field microscopy detection, decreases significantly with the sixth power of the particle diameter. In contrast, iSCAT detection experiences a slower signal drop due to the presence of a cross-term in the Eq. 1.1, which scales linearly with the scattering amplitude (s), thus only drops with the square of particle diameter [27, 44–48]. The advantage of iSCAT becomes particularly pronounced when the detection regime reaches below 50 nm in diameter. As demonstrated in Eq. 1.1, when the size of the detected particle is small, the pure scattering term (s^2) is significantly smaller than both the reflectivity of the interface (r^2) and the cross-term. While s^2 scales with the square of the volume of the scattering particle, the cross-term scales linearly. Consequently, this leads to a much slower signal drop with decreasing particle diameter. As a result, this interferometric contribution is especially compelling for ultrasensitive imaging.

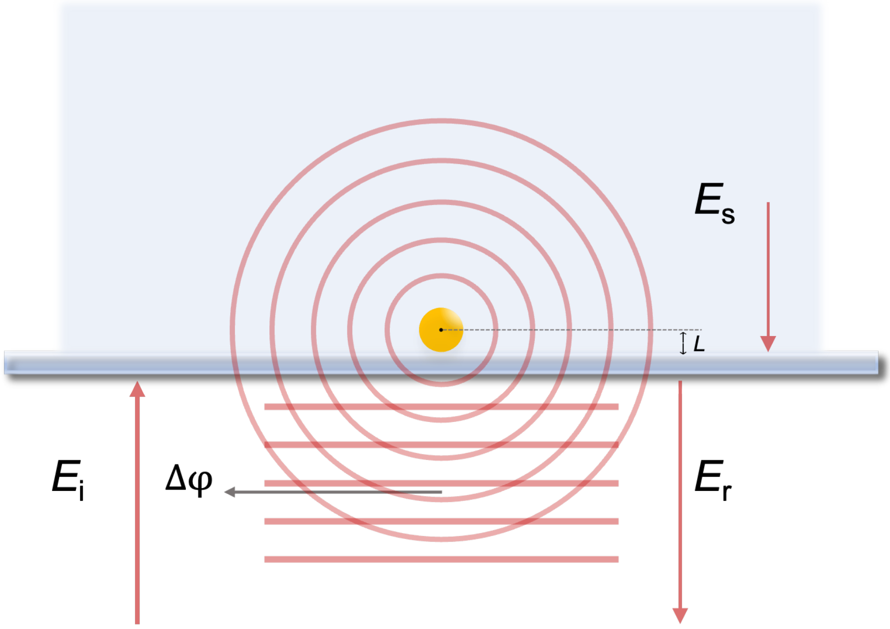

Figure 1.3: **Principles and performance of iSCAT for single-particle detection.** **(A)** Schematic view of interferometric scattering microscopy. E_i, E_s and E_r represent incident, scattered and reflected fields, respectively. $\Delta\varphi$ is the phase shift between the scattered and reflected signals and L is optical path lengths.

To obtain information about objects of interest in iSCAT detection, one can define the contrast as the ratio of the signal generated from the object of interest and the background.

It can be determined by comparing the detected signal before and after the presence of the object [44]. For objects smaller than 50 nm, the scattering intensity is very weak and thus can be ignored. In such cases, the signal contrast can be expressed as:

$$c = \frac{I_{\text{particle}}}{I_{\text{background}}} = 1 - \frac{2r|s|\sin(\varphi)}{r^2}. \tag{1.3}$$

The expression of iSCAT contrast, c (Eq. 1.3), also recapitulates the linear relation between the signal contrast and scattering amplitude, with the latter being linearly related to the volume of the object. iSCAT observation is diffraction-limited, the geometric shape and size of the diffraction-limited object (in this case, 50 nm gold nanoparticles) are limited by the point spread function (PSF) of the microscope. As shown in Fig. 1.4A, the PSF of individual 50 nm nanoparticles is surrounded by concentric rings caused by the interference between the plane (reflected) and spherical waves (scattered) and appears as dark (negative) on top of a bright background. In Fig. 1.4B, the contrast profile of the cross-section of a 50 nm AuNP depicted in Fig. 1.4A is presented. It's worth noting that in this instance, the size of the AuNPs is 50 nm, resulting in strong scattering signals which are also detectable in dark-field microscopy.

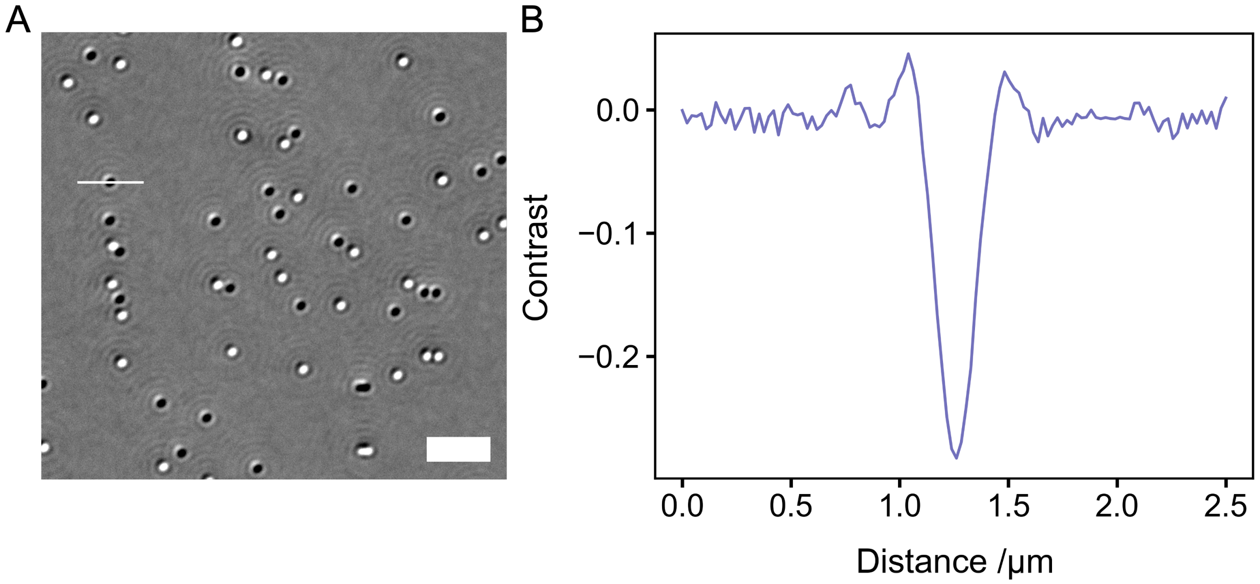

Figure 1.4: **iSCAT observation of 50 nm AuNPs.**
(A) Background corrected iSCAT image of 50 nm gold nanoparticles (the bright spots appeared in the image are due to the subtraction of the median averaged of stacks before movement, scale bar: 2 μm). **(B)** Contrast profile of the linecut across the particle in **A**.

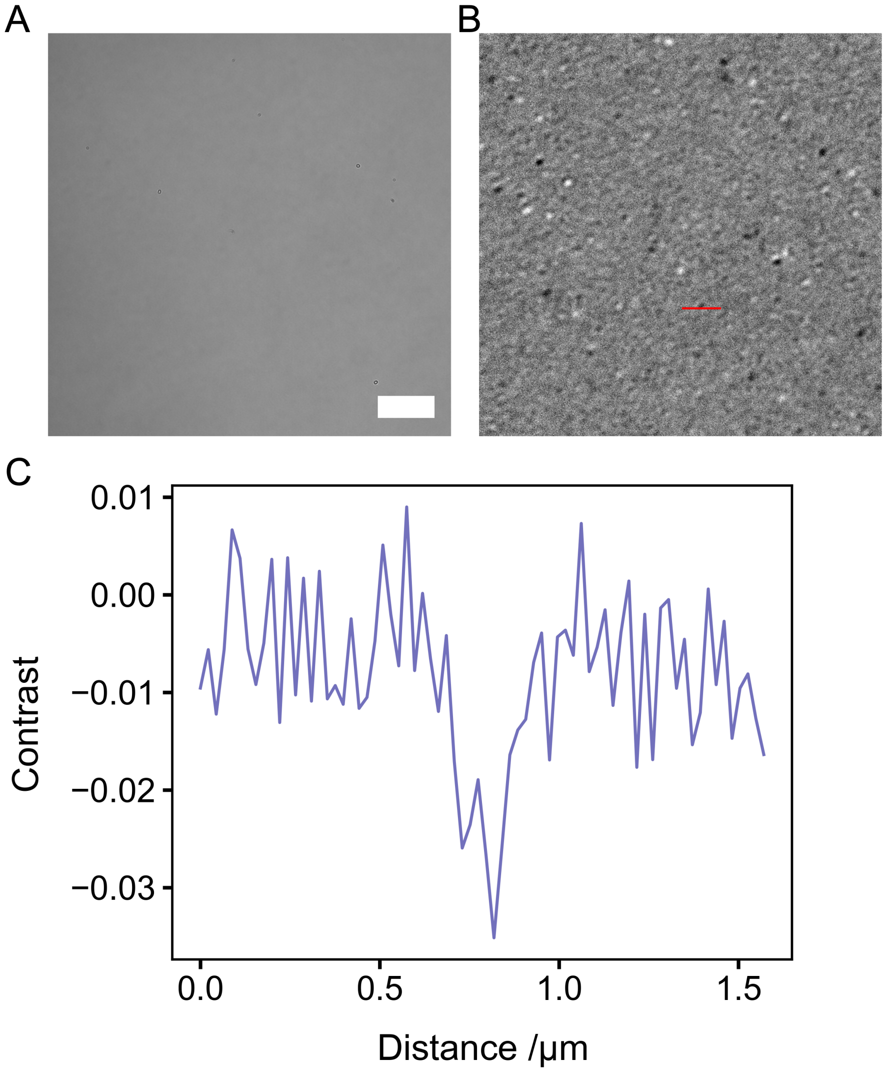

Figure 1.5: **iSCAT observation of 10 nm AuNPs.**
(A) Raw iSCAT image of 10 nm AuNPs (scale bar: 2 µm). **(B)** Background corrected iSCAT image of 10 nm gold nanoparticles (the bright spots appeared in the image are due to the subtraction of the median averaged of stacks before movement). **(C)** Contrast profile of the linecut across the particle in **B**.

AuNPs with smaller diameter were also measured by iSCAT. Former studies reported the successful detection of 2 nm [49] and 5 nm [43] AuNPs, with the detected contrast at least 3 times higher than the standard deviation of background noise. In our study, 10 nm AuNPs were spin-coated onto the coverslip, with water used as the imaging medium. As depicted in Fig. 1.5A, the 10 nm AuNPs exhibit very low contrast, making them imperceptible to the naked eye. Following background correction, faint dark particles become observable, as illustrated in Fig. 1.5B. The contrast of 10 nm AuNP (mean contrast: -0.024) is much higher than the standard deviation of background noise (0.001) which indicates we successfully detected 10 nm AuNPs.

One NP was selected with its contrast shown in Fig. 1.5C. From the contrast profile we can know that the 10 nm AuNPs produce much lower signal compared to 50 nm (mean contrast: -0.31, Fig. 1.4B), this can be problematic for dark-field detection. In terms of detecting softer materials such as proteins and polymers, they exhibit lower refractive indices compared to metal nanoparticles, resulting in much weaker scattering signals. Consequently, the current capability to resolve proteins extends to a molecular weight of around 40 kDa [50]. In our system, the detection limit for soft materials is approximately 70 kDa.

1.4.1 Fundamental concepts

Sensitivity

Imaging sensitivity describes the ability to reveal a subtle signal or the ability to differentiate that signal from the background. Currently, iSCAT can successfully detect single protein molecules with molecular weight down to 40 kDa [50], and with the assistance of unsupervised machine learning, the detection mass sensitivity limit can be pushed down to 10 kDa [51]. Detection sensitivity can be affected by signal variations, which include slow changes caused by thermal or mechanical drifts, as well as rapid, unpredictable variations commonly referred to as noise. During iSCAT observation, the main source of noise includes laser intensity noise, detector background noise, dynamic range and analogue-to-digital conversion noise, and mechanical stability [45]. Under the most optimized conditions, the shot noise can be the only noise source associated with the counting of discrete photons arriving at the detector. The SNR for a shot-noise-limited iSCAT experiment scales with the square root of the number of photons, which means a greater SNR can be acquired by increasing laser input or integration times.

Resolution

Spatial resolution describes the ability to distinguish two closely spaced objects or to reveal fine details in a sample, which can be further divided into lateral and axial resolution. Temporal resolution represents the ability of an imaging system to capture rapidly occurring events. There exists a trade-off relation between temporal and spatial resolution. For example, the increase in temporal resolution leads to a reduced number of photons that can be collected per frame, resulting in decreased precision. Compared to fluorescence imaging, in which the number of protons that can be detected per unit of time is constrained by fluorescence saturation, iSCAT is not limited by the photon budget, thus allowing high temporal resolution to be reached. The main limitations are from the saturation of the camera or the sample/optical damage thresholds.

1.4.2 Modes of iSCAT microscopy

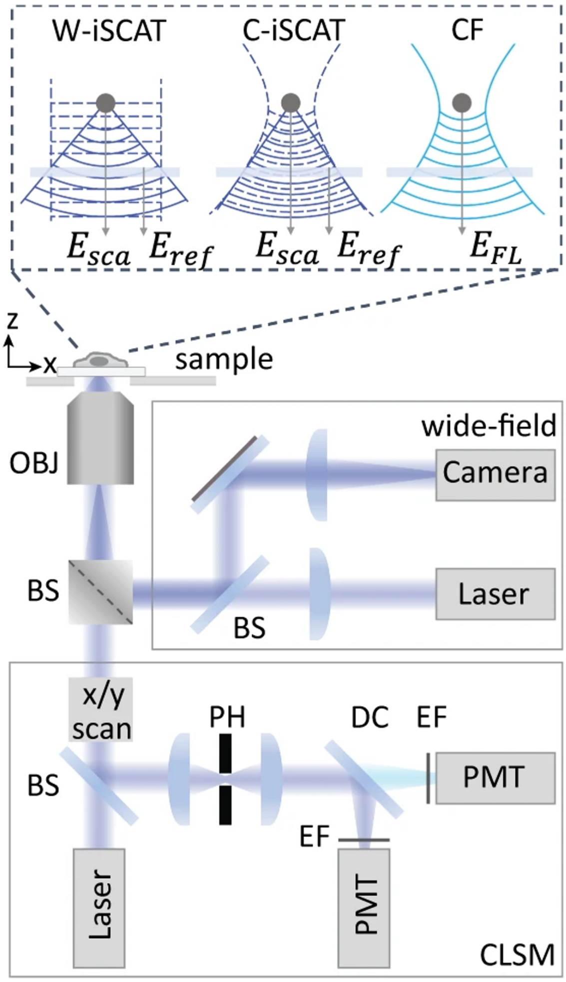

Figure 1.6: **iSCAT operates in wide-field and confocal modes and in combination with a confocal laser scanning microscope.**
iSCAT imaging can be conducted in both wide-field (W-iSCAT) and confocal (C-iSCAT) modes, alongside confocal fluorescence (CF) microscopy. E_{ref}, E_{sca} and E_{FL} represent electric fields of the light reflected back from the sample glass interface and that scattered by the object of interest and fluorescence emission, respectively. OBJ, objective; BS, beam splitter; PH, pinhole; DC, dichroic mirror; EF, emission filter; PMT, photomultiplier tube. Inset: Dashed lines represent wavefronts of laser illumination and solid lines represent sample radiation [52].

Wield-field illumination as shown in Fig. 1.3A and Fig. 1.6 (the first mode in the inset), is a commonly used modality in iSCAT imaging. The laser beam is focused at the back focal plane (BFP) of the objective, a nearly-collimated illumination can be achieved. It not only provides large fields of view (up to hundreds of µm^2) but also enables fast imaging speed to be achieved (up to 1 MHz) [53]. However, the standard wide-field illumination produces somewhat poorer image quality because of the strong reflections produced by the focused beam. Thus, by performing beam scanning, a uniform illumination can be produced without the presence of interference fringes [54]. Furthermore, iSCAT can also be operated in confocal mode (the second mode in the inset). By using a focused Gaussian beam to scan across the sample, the confocal mode of iSCAT provides access to the nanoscopic displacements in the axial direction with high resolution, meanwhile minimizes out-of-focus scattering background [43, 52]. However, the laser intensity fluctuations would contribute to the background noise and limit the sensitivity. Inherently, this mode limits the imaging speed, posing a significant challenge in monitoring fast dynamics. A recent study has successfully demonstrated that the image acquisition rate can be improved to hundreds of frames per second (up to 1000 frames per second with reduced fields of view) with high sensitivity (10 nm gold nanoparticles can be detected) by using an iSCAT confocal microscopy modified from a spinning disk confocal fluorescence microscopy [55]. Moreover, as shown in Fig. 1.6, iSCAT modality is compatible with fluorescence microscopes setup, which can be seamlessly integrated to mutually enhance their capabilities [52, 56]. It is worth mentioning that while there are plans to develop iSCAT with more complex modalities for future research, the wide-field iSCAT developed by Dr. Vivien Walter constituted the sole modality available during the course of my study and was consequently utilized in my research.

1.4.3 Applications

Label-free single-molecule/nanoparticle detection and imaging

Proteins: iSCAT has been successfully applied to detect, track and image single protein in a label-free manner [18, 57, 58]. By combining Eq. 1.2 and Eq. 1.3, it can be noted that the detected contrast depends on three factors: The refractive indices of the protein and its surrounding medium, as well as the volume of the protein. Given that the imaging medium remains constant, and proteins are composed of amino acids with similar refractive indices [59], the contrast of individual protein molecules can be attributed to their volume, and as a result, their mass, due to their comparable (fixed) density. This fosters the development of mass photometry, which is able to provide mass information about individual molecules and thereby determines mass distributions of biomolecule samples in solution [50]. Synthetic polymers show a great analogy to proteins, and we reasoned that the relationship between molecular weight and iSCAT contrast is also applicable to polymeric systems. In Chapter 3, iSCAT is applied to study the kinetics of individual polymer chain growth by monitoring their contrast evolution.

Gold nanoparticles: Gold nanoparticles (AuNPs) play an essential role in iSCAT development. The introduction of iSCAT to the research community occurred with the detection of AuNPs with sizes varying from 5 nm to 60 nm. To date, iSCAT is capable of detecting 2 nm AuNPs, which are even smaller than a single protein molecule, with a spatial resolution of 8 nm [49]. Due to their excellent scattering efficiency and biocompatibility, AuNPs have been served as scattering labels detected and tracked by iSCAT, providing insights into various systems [6, 53, 60–63]. In this study, we applied iSCAT to monitor the formation of AuNP itself, with their kinetics heterogeneity being extracted [13].

Virus: Viruses (20-200 nm) are able to provide substantial iSCAT contrast for imaging, making them one of the most extensively studied subjects in iSCAT research [52]. For instance, in combination with fluorescence imaging, iSCAT was used to detect single viruses bound to receptors on a supported lipid bilayer, allowing the information regarding virus position and orientation to be extracted [54]. In addition, by monitoring the evolution of iSCAT contrast, the stimulated ejection of DNA from individual bacteriophages was visualized with a shot-noise-limited precision (4200 base pairs) [64].

Dynamics monitoring

Single-particle tracking: Single-particle tracking allows the visualization of the trajectory of individual nanoparticles or molecules. When small objects such as AuNPs are used as probes and tracked, the commonly inaccessible nanoscopic dynamics can be easily revealed. As introduced before, the image of a subwavelength object is shown as the PSF. By fitting its PSF with a 2D Gaussian function, the mass center of this object can be localized with high precision [65]. For example, 20 nm AuNPs attached to lipid molecules on a membrane can be tracked with a spatial precision down to 2 nm within microseconds [66]. Studies also tried to further improve the temporal resolution for high-speed tracking. A 913 kHz acquisition rate was reached to track 20 nm AuNPs diffusing on the membrane with 10 nm spatial resolution [53]. Besides using tags, label-free tracking was also successfully achieved by tracking individual microtubules (producing signals close to 20 nm AuNPs) with a localization precision of 0.4 nm at 100 Hz [67]. Furthermore, the amplitudes as well as the radial positions of the PSF rings contain the axial position information, thus allowing tracking to be extended from 2D to 3D. As an example, transmembrane epidermal growth factor receptors were tracked in 3D with nanometer precision at speeds of up to microseconds, enabling observations lasting for minutes [8].

Assembly dynamics: iSCAT can be considered as a refractive index microscope, it is sensitive to the changes in the optical properties of the objects [68]. Using our study as an example, when utilizing iSCAT to monitor the growth of individual AuNPs (see more details in Chapter 4), in a diffraction-limited volume, before the initiation of the reaction (in the absence of the AuNP), the optical properties of that volume equal to its surroundings, and no scattering signal can be produced. This situation would change once the particle appears and grows. As a result, iSCAT can be used to report such size evolution with high spatiotemporal resolution [13]. Similarly, iSCAT was used to study the actin polymerization [50], the formation of lipid bilayers [69] and nanoscopic lipid phase transitions [70]. In Chapter 5, we successfully used iSCAT to observe the nonuniform distribution of polymeric materials during the formation of nanoplatelets and directly visualized the composition variation within a single multilayered platelet based on iSCAT contrast.

1.5 Summary and outlook

Over the past few decades, significant progress has been made in advancing optical single-molecule techniques, empowering researchers across diverse fields to explore and control individual molecules with unparalleled accuracy and sensitivity. This chapter has provided an overview of several widely employed optical single-molecule techniques, offering insights into their underlying physical mechanism, as well as their respective strengths, weaknesses, and applications. The main focus has been given to interferometric scattering microscopy which served as the key technique for my study. The enhanced sensitivity of iSCAT compared to dark-field microscopy was discussed in depth and the relation between iSCAT contrast and the size of the observed objects was established. Furthermore, the applications of iSCAT in optical detection, imaging, and characterizations as well as dynamic process monitoring were summarized.

The current state of the art in iSCAT achieves sensing of single protein molecule with molecular weight down to 40 kDa [50]. Gold nanoparticles as small as 20 nm can be tracked with 10 nm spatial precision at nearly 1 MHz imaging rate [53]. Innovations in detector technologies, data analysis techniques, image process as well as machine learning will undoubtedly push its sensitivity and resolution further, which will open up new horizons for studying a broader range of biological, chemical, and physical phenomena. While iSCAT offers notable advantages and capabilities, the realization and adoption of this technology are still in their infancy with their application mainly concentrated on the field of biology. However, we are confident that with more attention being given to iSCAT, it will likely become a transformative method for providing quantitative information across various research fields.

Chapter 2

iSCAT microscope construction and preliminary investigations

2.1 Introduction

In fluorescence detection, spectral filtering allows for the efficient isolation of the signal of interest from background illumination, enabling single-molecule detection sensitivity to be achieved [21]. Similarly, in the context of scattering imaging, commonly referred to as dark-field microscopy, spatial filtering was applied to achieve background rejection. By taking advantage of the fact that any object with a refractive index that varies from its surrounding medium can generate scattering signals, the need for extrinsic labels is unnecessary, offering distinct advantages over fluorescence imaging [45, 48]. However, the detection of pure scattering signal from ever smaller objects becomes problematic, as the scattered signal drops dramatically with particle volume which can be easily overwhelmed by stray light produced from the sample or imperfections in the optics. By introducing a reference signal to interfere with the scattering signal, iSCAT is able to counteract the rapid decrease in scattered intensity seen in dark-field microscopy.

To apply iSCAT to my study, I initiated this project with the development of an instrument calibration procedure. Monodispersed gold nanoparticles with sizes ranging from 10 to 60 nm were spin-coated onto the plasma-cleaned glass coverslip, separately, with water chosen as the medium for imaging. The contrast distribution of AuNPs for each size was then extracted, which generated a contrast *vs.* particle diameter calibration curve. AuNP has been widely used in optical imaging and plays an essential role in iSCAT development [6, 71]. In the visible regime, AuNPs exhibit strong plasmon resonances caused by the collective oscillations induced by the interactions between AuNPs and the oscillating electric field. This effectively enhances its scattering efficiency, allowing the light to be scattered from a much larger cross-section than its actual physical size. For example, under 532 nm irradiation, a 40 nm AuNP can produce a similar signal as a 160 nm silica bead.

2.2 Instrument calibration

2.2.1 Instrument construction

In this study, a wide-field iSCAT was built by Dr. Vivien Walter in our laboratory. In addition to the existing setup, a 405 nm single-mode diode laser was introduced into the light path for the patterned nanoparticle growth discussed in Chapter 4. No further modifications were made beyond this addition. A detailed depiction of the setup is presented in Fig. 2.1A. A 637 nm multimode diode laser (RLMjup-6000L, Kvant lasers, Slovakia) is directed through a lens (L1) and focused to a port of an optical fiber. Once it traverses the beam homogenizer (Albedo system, Errol, France), a top hat beam profile is generated. Upon passing through a second optical fiber, further followed by a collimation telescope, the homogenized light field then undergoes resizing and collimation. Subsequently, the collimated beam passes through a lens (L2) placed at a distance equal to one focal length from the back focal plane (BFP) of the objective. The incorporation of a polarizing beam splitter (PBS) permits the transmission of plane-polarized light with a specific orientation, which subsequently reaches the quarter-wave plate (QWP). When used in combination, these two components commonly serve as an optical isolator, which allows the signal of interest to be efficiently separated from the illuminated light, as depicted in detail in Fig. 2.1B. Following its passage through the QWP, the plane-polarized light undergoes conversion into circularly polarized light, ultimately being focused at the BFP of a 100× objective (Plan-Apo 1.45 NA, Nikon, Japan). The light then be collimated again by the objective and achieves epi-illumination at the sample, providing a 20 × 20 µm field of view. As mentioned earlier, a portion of light reflected back from the sample-glass interface travels alongside the light scattered by the objects within the sample, eventually reaching the QWP. The QWP converts them back into plane-polarized light with 90° rotation relative to the incident beam. After passing through the PBS, the signal is separated from the incident light and directed toward a high-speed CMOS camera (PCO.dimax CS1, ExcelitasPCO GmbH, Germany). A CMOS camera was chosen here as it shows great advantages in iSCAT imaging due to its high frame rates, flexibility in selecting regions of interest, and large full-well capacities [56]. Furthermore, focus control was provided by a piezo-stage (P-545-3R8S, Physik Instrumente, Germany). The camera, laser, and piezo-stage are controlled using a custom LabVIEW program (National Instruments, USA).

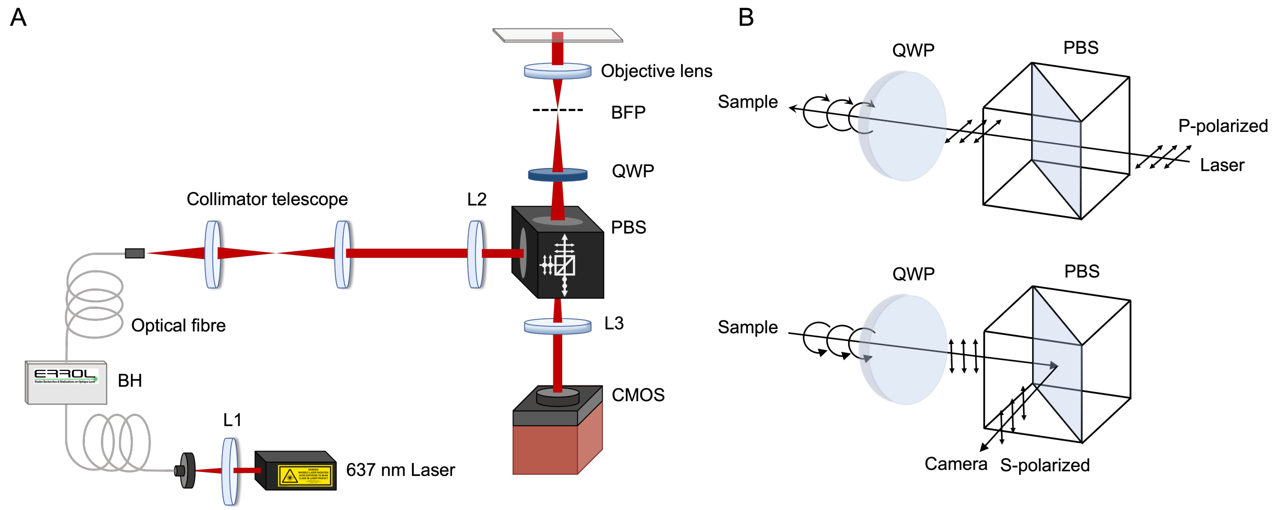

Figure 2.1: **iSCAT setup**
(A) BH, beam homogenizer; PBS, polarizing beam splitter; QWP, quarter-wave plate; BFP, back focal plane; CMOS, complementary metal oxide semiconductor sensor. **(B)** An example of a polarization-dependent optical isolator: P-polarized incident light is transmitted through the PBS, passes through the QWP (which converts it to a circularly polarized light), interacts with the sample, generating a signal with the opposite-handed circular polarization (upper figure). This signal passes through the QWP again, converting it to a S-polarized light which is then reflected by the PBS and directed toward the detector (lower figure) [72].

2.2.2 Contrast calibration

Materials

10, 20, 30, and 50 nm PEG-carboxyl capped monodispersed AuNPs were purchased from nanoComposix and used as received. 60 nm citrate capped AuNPs were purchased from Merck and used as received.

Sample preparation

Unless otherwise stated, the following cleaning protocol was consistently employed throughout this thesis. Glass coverslips (24×60 mm, #1.5 thickness, Epredia) were sonicated successively for 15 minutes in chloroform, acetone, and isopropanol before drying with N_2. Then the solvent-cleaned coverslips were treated with oxygen plasma for 6 minutes (Diener Electronic, Femto, Germany). Circular silicone spacers (ϕ9×2.5 mm thickness, Merck) were washed with the same protocol, and dried under vacuum.

AuNP standards were sonicated for 1 min to break the aggregates (it should be noted that longer sonication time may lead to unwanted aggregation) before a 25 µL sample solution was spin-coated onto the plasma cleaned coverslip (4000 rpm, 30 s). A cleaned spacer was mounted onto the AuNPs coated coverslip, purified water (Millipore Direct-Q UV3, Merck) was added into the reaction chamber then sealed with an additional coverslip (22×22 mm, Merck) which was solvent cleaned using the same procedure as introduced above.

Image acquisition

Data presented in this chapter was collected based on the following recording conditions: 3000 frames were collected with a laser power density of 2 µW μm^{-2} at 637 nm, a camera exposure time of 220 µs and overall time-lapsed frame rate of 3670 Hz. In order to distinguish objects of interest from the static scattering background produced from the glass surface via the post-experiment data process, the piezo stage was set to perform a 2D random walk with a fixed z axial position (objects of interest will move with the stage but the background will remain static). At each step, a random direction was selected, adhering to a random step length. This procedure is illustrated in the right-hand image of Figure 2.2A, where all particles are directed downwards, indicated by the red arrow. The dark particles are the objects of interest, which were tracked and with their contrast then extracted. The presence of bright spots is because of the background correction: The median-average of the stacks before the movement was used as the background and subtracted from the stacks after the movement, thus the particles in the former position were subtracted and shown as bright spots. The subsequent section provides detailed information about the data process and extraction.

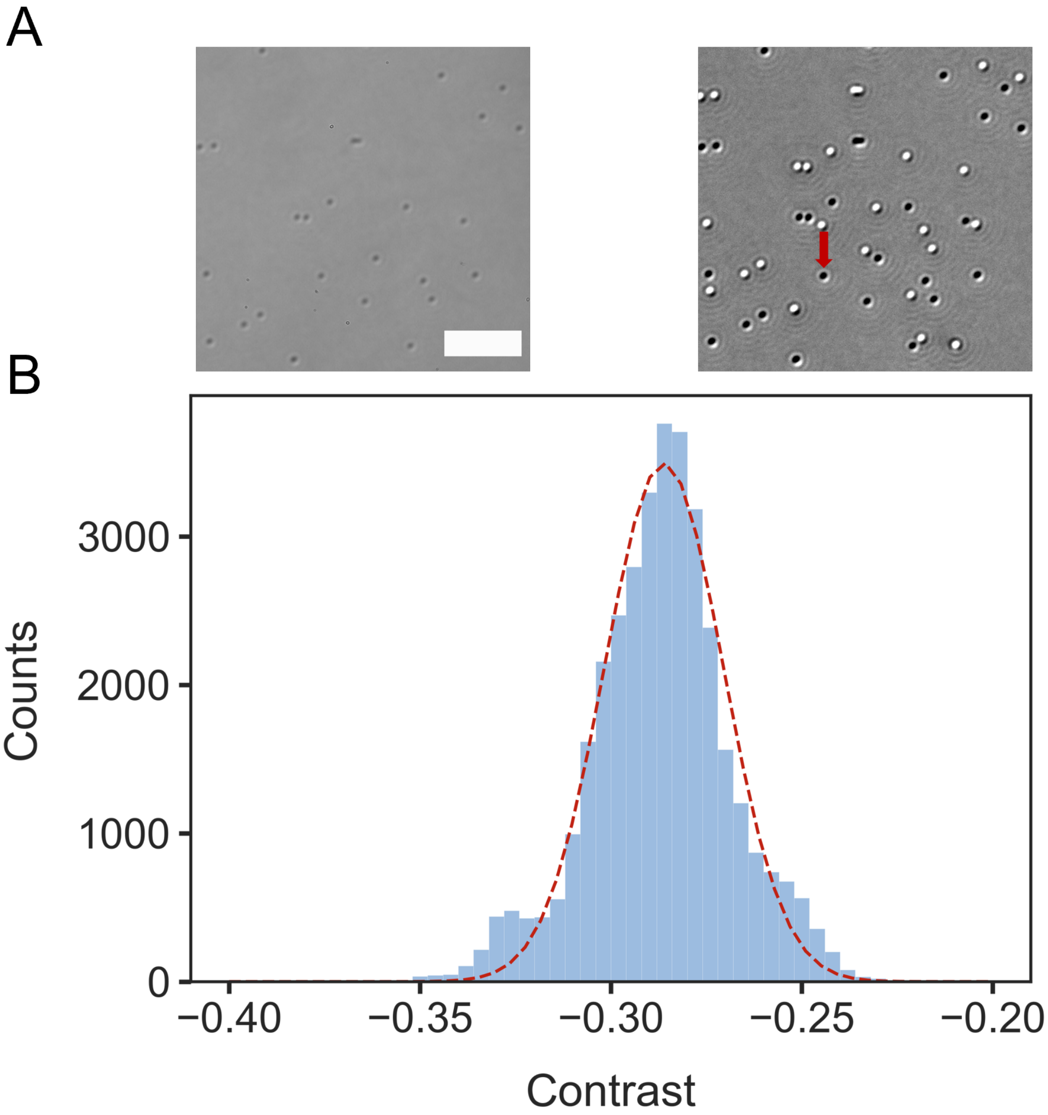

Figure 2.2: **Example of extracting the contrast of 50 nm AuNPs.**
(A) Raw (left-hand) and background corrected (right-hand) iSCAT images of 50 nm AuNPs. The red arrow indicates the particle moving direction, bright and dark particles corresponding to the same particles before and after movement, respectively. **(B)** Contrast distribution fitted with Gaussian distribution.

Image analysis

Image analysis was performed using Python scripts developed in-house, with the following steps:

1. Image stacks were first cropped to remove the non-laser illumination area (raw iSCAT image is shown in the left-hand image in Fig. 2.2A).

2. Dark counts subtraction was conducted by subtracting each frame by a frame recorded under the same conditions without laser illumination.

3. Laser spatial intensity fluctuations were suppressed by dividing each frame by its own modal pixel value.

4. The median average of the first 500 frames (frames before movement) was chosen as the background which contains the static features (e.g., glass roughness). This background was then subtracted from the raw frame sequence (stacks after movement).

5. To convert image intensities to contrast values, the background corrected stacks were then background-normalized by dividing these stacks by the background produced from median averaging. The result is shown in the right-hand image in Fig. 2.2A.

6. Particles were located using the Python module TrackPy [73]. Particles were selected based on the following filtering conditions: the diameter of the circle used to detect and analyze spots was set to 21 pixels; a minimum separation between particles of 2× this diameter was specified; the minimum integrated brightness was set to 0.01 and a threshold with the value of 0.001 was applied. TrackPy returns information including the position and the size of tracked objects. A region of interest (ROI) was then defined by using the particle position as an origin and its size as the diameter. Then within the ROI, the pixel value with the maximum absolute value was defined as the contrast of the corresponding particle.

7. For each size, around 100 AuNPs were tracked with their contrast being extracted. The contrast distribution for each size was then fitted to a Gaussian function as shown in Fig.

2.2B. From the fitting, the mean and standard deviation of the contrast for each size of AuNPs can be extracted.

2.2.3 Calibration curve

Particle contrast, c, as defined in Chapter 1 (Eq. 1.3), can also be expressed in terms of the particle scattering cross-section (σ_{scat}), a proportionality constant (β) describing the instrument sensitivity and the phase shift between reference and scattered field (φ) [68]:

$$c = \beta^2 \sigma_{\text{scat}} - 2\beta\sqrt{\sigma_{\text{scat}}}\sin\varphi. \tag{2.1}$$

The scattering cross-section (σ_{scat}) relates to the particle polarizability ($\alpha = \frac{\pi D^3}{2}\left(\frac{n_{\text{p}}^2 - n_{\text{m}}^2}{n_{\text{p}}^2 + 2n_{\text{m}}^2}\right)$), which has been introduced in Eq. 1.2 in Chapter 1. The scattering cross-section (σ_{scat}) can be expressed as:

$$\sigma_{\text{scat}} = \frac{8\pi^3}{3}\left(\frac{n_{\text{m}}}{\lambda}\right)^4 \alpha^2 = \frac{2\pi^5}{3}\left(\frac{n_{\text{m}}}{\lambda}\right)^4 \left(\frac{n_{\text{p}}^2 - n_{\text{m}}^2}{n_{\text{p}}^2 + 2n_{\text{m}}^2}\right)^2 D^6 = P_1 D^6, \tag{2.2}$$

where λ is the wavelength of illumination source, and to highlight the relation between σ_{scat} and particle diameter (D) [47], σ_{scat} can be simplified as the product of an experimental parameter 1 (P_1) and diameter raised to the power of 6 (D^6) as shown in above. As a result, the relation between iSCAT contrast and particle diameter can be established as:

$$c = \beta^2 P_1 D^6 - 2\beta\sqrt{P_1} D^3 \sin\varphi. \tag{2.3}$$

Following the data process procedure introduced before, the mean contrast of AuNPs for each size can be extracted. Fig. 2.3 displays the evolution of mean contrast as the function of particle size (hereafter as calibration curve) alongside previously reported values [49, 68, 74, 75].

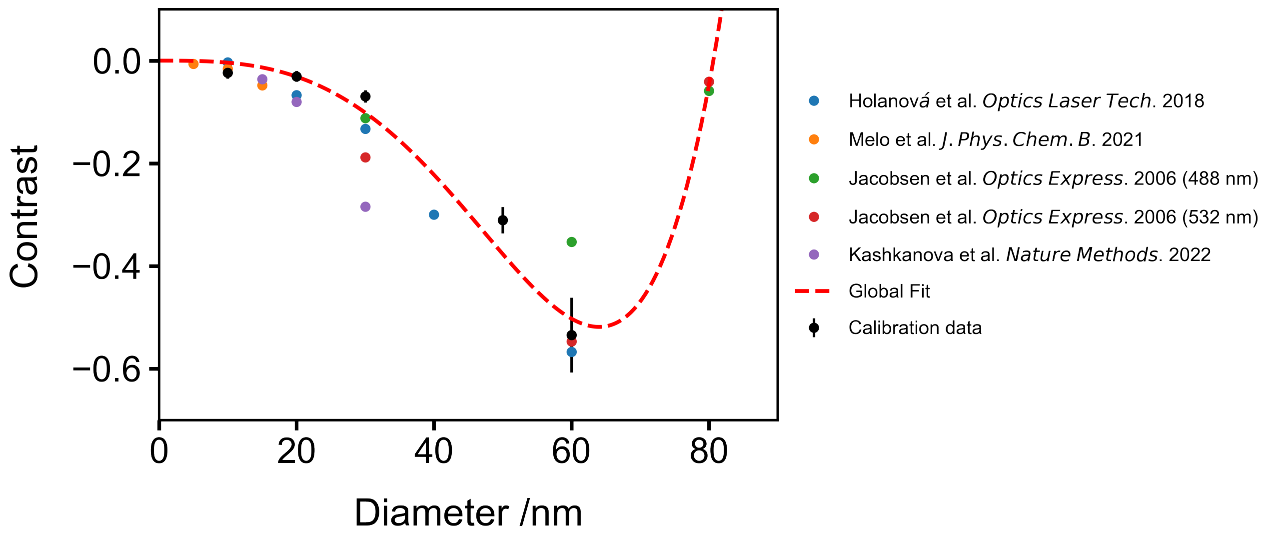

Figure 2.3: **Standard AuNPs calibration.**
The evolution of mean contrast as the function of particle size. Error bars represent the standard deviations produced from Gaussian fitting of the particle contrast distribution for each particle size. Figure is taken from reference [13].

As the relation between particle size and contrast has been established. The calibration curve was then fitted to Eq. 2.3 using Scipy.optimize [76] with fixed refractive indices corresponding to our experiment conditions ($n_{\mathrm{p}} = 0.18$ and $n_{\mathrm{m}} = 1.33$). Using this procedure, β can be determined as 9.07 $\times 10^7\,\mathrm{m}^{-1}$, similar to previously reported values [68]. It is worth mentioning that, Fig. 2.3 exhibits a contrast reversal (changes from negative towards positive), which has also been observed by former studies [43, 49]. This is related to phase shift (φ), which is affected by several factors, including the Guoy phase, the scattering phase, and the phase difference caused by the path length difference between scattered and reflected light. In this case, to observe AuNPs with different sizes on the surface, as the objective-sample distance is fixed, the Gouy phase remains constant, meanwhile, the scattering phase also remains constant, which can be calculated from the refractive index of the AuNPs. As a result, the only variable is the optical path length (L) caused by the AuNP size variation. The increase of AuNP diameter leads to the increase of the optical path length (L), eventually leads to the change of phase shift (φ) and contributes to destructive or constructive interference results. Using iSCAT to observe individual AuNPs growth in Chapter 4 vividly illustrates this phenomenon.

2.3 Summary

This chapter explicitly introduces our iSCAT setup that has been applied throughout my research. By measuring the contrast of 10-60 nm AuNPs, we successfully explained the correlation between iSCAT contrast and the size/mass of the object. The distinctive combination of sensitivity, flexible temporal range, and the ability to conduct label-free imaging allow iSCAT to report the contrast evolution of individual objects with high spatio-temporal resolution. Based on the relationship between contrast and object properties, it is possible to extract the size/mass evolution over time, which can be further translated into individual object kinetic information. This is the fundamental principle that serves as the cornerstone of my study, repeatedly applied throughout my research.

The imaging mechanism of iSCAT relies on the refractive index difference between the object of interest and its surroundings. This allows iSCAT to be applied across a wide range of systems, varying from biological molecules to metal nanoparticles. Thus, in the following chapters, iSCAT was applied to explore the nanoscopic dynamics of polymerization reactions, nanoparticle formation, and crystallizable polymeric material assembly.

Chapter 3

Interferometric imaging of molecular polymerization

The research presented in this chapter was conducted in collaboration with Dr. Amanda Pearce and Dr. Jeffrey Foster from Professor Rachel O'Reilly's group at the University of Birmingham. They played a crucial role in training me for conducting polymerization reactions and providing valuable advice throughout the project.

3.1 Introduction

3.1.1 Polymerization and molecular weight distribution.

Synthetic polymers are the backbone of modern society with widespread applications across industry, science, technology, and in our daily lives [77, 78]. Free radical polymerization plays a key role in polymer production, contributing to over 50% of annual output [79, 80]. It is generally started with the generation of primary radicals via covalent bond cleavage caused by heat, light, or a redox process. Then the primary radicals can be added to carbon–carbon double bonds in monomer (e.g., vinyl monomers), followed by successive monomer units addition, leading to the extension of the polymer chain [81, 82]. However, due to the irreversible termination and transfer process, as well as the absence of mediating species to apply control to the reaction, the polymeric products usually exhibit poor control on the molecular weight distribution (MWD)

[83, 84]. MWD describes the chain length distribution of the polymer, many physical properties of polymers are governed by their underlying molecular weight and MWD [85]. For example, the same type of polymer with different molecular weights can exhibit totally different physical properties, such as viscosity and transition temperature (i.e., the higher the molecular weight, the higher the transition temperature and viscosity [86]). In addition, studies indicate that the mechanical properties, such as Young's modulus, rheological properties, and processability are intimately related to MWD [87–90]. The statistical properties of this distribution are typically understood in terms of parameters such as the number average molecular weight (M_{n}), the weight average molecular weight (M_{w}), and the dispersity ($Đ$) [91]. M_{n} relates to the total number of molecules in a unit mass of polymer which includes all kinds of shape or size of the polymer chains. On the other hand, M_{w} depends on the molecular size, which means polymer chains with higher molecular weight may contribute more to M_{w}. $Đ$ is the ratio of the weight average and number average, which represents the width of the MWD [90, 92]. Size exclusion chromatography (SEC) is the most commonly used technique to measure M_{n} and M_{w}, and gives insight into the MWD of the polymer product.

3.1.2 Surface-initiated oxygen-tolerant controlled radical polymerization

Controlled (or living) radical polymerization, such as atom transfer radical polymerization (ATRP) [93], reversible addition-fragmentation chain transfer polymerization (RAFT) [94], and nitroxide-mediated polymerization [95] have revolutionized polymer science by providing a simple method to synthesize polymers with controlled molecular weight, architecture, end-group fidelity and dispersity [96, 97]. Among these techniques, since its first introduction in 1995, ATRP has been extensively reviewed [96, 98–100] and has become a commonly used method for implementing polymer growth on surfaces. Based on its reaction mechanism shown in Scheme 1 (Fig. 3.1), the reaction is controlled by the equilibrium between dormant and active species, with the active radicals being deactivated after one or several monomer unit additions. Growing radicals (R^*) can be intermittently generated by the periodical reaction between the dormant

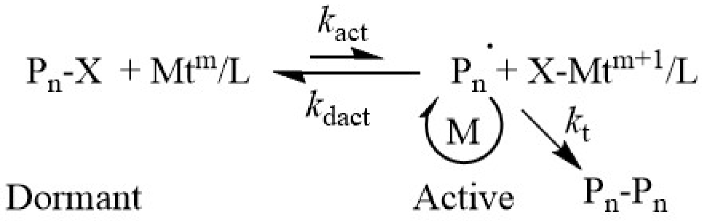

Figure 3.1: **Scheme 1. ATRP equilibrium**

form, alkyl halides/macromolecular species (P_n-X) and the activators, metal-ligand catalyst complex (Mt^m/L, where Mt^m is the transition metal species in oxidation state m, L represents ligand. The charges of ionic species and counterions are omitted here.) under the rate constant k_{act}. The growing radicals then react with transition metal complexes in their higher oxidation state (X-Mt^{m+1}/L), which act as deactivators to return to the dormant state with the rate constant k_{dact} [100–103]. Polymerization control is achieved by rapid radical deactivation, as the dynamic equilibrium is skewed to the deactivation side, which generally keeps the population of active radicals at a low level and suppresses undesirable radical-radical termination [104, 105]. This activation/deactivation process ensures that most polymer chains propagate at a similar speed, leading to control over the molecular weight [106].

In this study, we aim to use iSCAT to observe individual polymer chain growth. From the imaging mechanism introduced in the former chapters, we know that the generation of an iSCAT signal requires a reference beam generated by reflection from a surface, which means the polymer growth must occur at or near the interface. Although, ATRP is an elegant way to provide surface-initiated polymer growth by immobilizing initiators onto the surface, the limited oxygen tolerance of conventional ATRP prevents us from directly conducting ATRP under iSCAT imaging conditions. The presence of trace amounts of oxygen can lead to deactivation of the activators and inhibit the polymerization [107], and also cause termination of the reaction by attacking the propagating carbon-based radicals [108]. With our current experiment setup, rigorous oxygen-free conditions cannot be achieved. Fig. 3.2 illustrates the commonly used reaction chamber in iSCAT imaging, which is assembled using a large coverslip (24×60 mm), a rubber spacer ($\phi 9 \times 2.5$ mm thickness), and a small coverslip (22×22 mm) sandwiched together to create a reaction space (For iSCAT imaging, this reaction chamber is mounted above the microscope objective, with the focus adjusted onto the interface.). The second coverslip prevents solvent evaporation but is less effective in creating an oxygen-free condition. Thus, an oxygen-tolerant ATRP is required in this study.

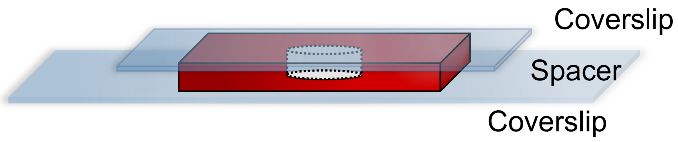

Figure 3.2: **Reaction chamber construction**

Photoinduced polymerization provides an alternative approach for the oxygen-tolerant ATRP [109–111]. Matyjaszewski and coworkers proposed a fully oxygen-tolerant method known as photoinduced initiators for continuous activator regeneration (PICRA) ATRP. It allows polymerization to occur in the presence of air, yielding polymer chains with high molecular weights ($M_\mathrm{n} > 270{,}000$) and low dispersities ($1.16 < Đ < 1.44$) in less than 30 minutes [112]. We assume this is an ideal benchmark to test our experiment. Firstly, oxygen tolerance enables the reaction to be conducted under the imaging conditions. The high achievable final molecular weight (far exceeding our detection limit of 70 kDa) enables a broader reaction range to be monitored by iSCAT. Meanwhile, the reaction kinetics is relatively fast (finished within 30 min) and can be further adjusted by varying the reaction conditions. Based on the time resolution of our setup (100 µs), iSCAT can provide real-time monitoring of individual polymer chain formation.

Sodium pyruvate (SP) plays an essential role in this reaction. It not only efficiently eliminates oxygen under ultraviolet light emitting diode (UV LED) irradiation, enabling the reaction to be conducted in the presence of air, but also serves as an exciter to facilitate activator regeneration at the same time. As depicted in Scheme 2 (Fig. 3.3), when copper is employed as the catalyst, SP undergoes a reaction with $\mathrm{Cu^{II}}$, yielding the $\mathrm{CH_3C(O)CO_2\text{-}Cu^{II}/L}$ complex through an anion dissociation/association process. With the presence of UV irradiation, the carbon-carbon bond in the pyruvate moiety undergoes homolytic cleavage, generating $\mathrm{Cu^{I}/L}$ and the acyl radical, the latter can reduce another molecule of $\mathrm{Cu^{II}/L}$ to $\mathrm{Cu^{I}/L}$. Molecular oxygen mainly reacts with the $\mathrm{Cu^{I}/L}$, as its concentration is much higher than the concentration of propagating radicals. During this process, H_2O_2 is generated, which can be harmful to the reaction because it produces unwanted hydroxyl radicals and triggers other parasitic reactions. The presence of SP inhibits this process, allowing H_2O_2 to be quenched and form the unharmful products CO_2, H_2O and sodium acetate. As a result, the reaction can be conducted under an ambient atmosphere, with the oxidized catalyst continuously being converted back to its active reduced form.

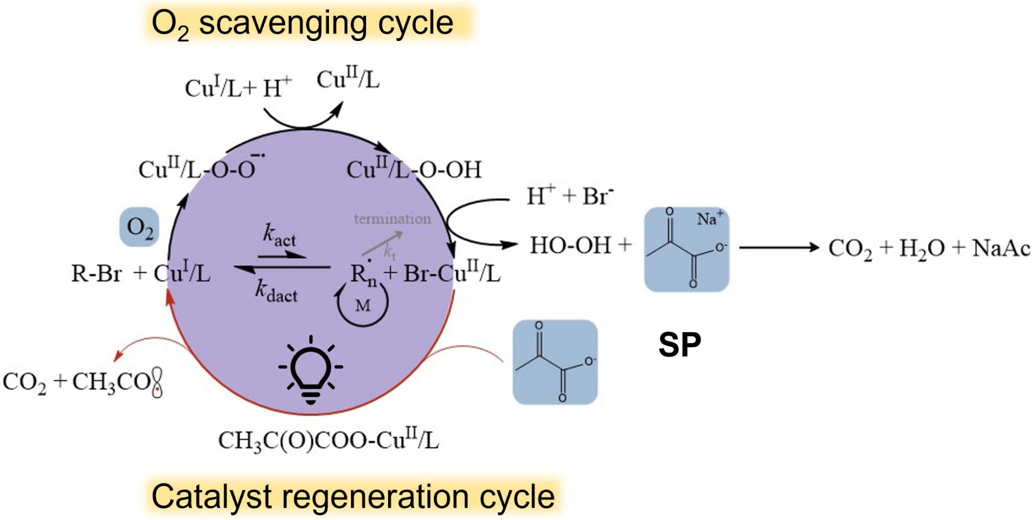

Figure 3.3: **Scheme 2. Mechanism of PICAR ATRP**

3.1.3 Techniques for polymerization characterization

Despite considerable experimental and theoretical efforts, a lot of questions regarding polymerization kinetics remain unsolved. For example, it is unknown what fraction of chains are initiated during the polymerization, what fraction of chains are growing, or the proportion of 'dead' chains at a given time. Understanding the polymerization kinetics is the first step to achieve control over the reaction. To reveal the underlying kinetics and mechanisms of a reaction, real-time monitoring of individual polymer chain growth can provide important information. However, with conventional techniques, this knowledge is limited to just the ensemble average of a particular molecular property [113]. Commonly used techniques do not provide the resolution to understand the individual molecular behavior giving rise to the bulk properties of the material

[114]. As mentioned above, traditional techniques such as SEC and UV-vis spectroscopy can only measure M_n and $Đ$, which provide information solely about the average center and breadth of the MWD, without describing the precise distribution of molecular properties associated with each chain [115–117]. Furthermore, the molecular-level heterogeneity that occurs during the polymerization process is also inaccessible [114].

Thus, techniques with improved resolution were introduced for polymerization kinetic study. For example, atomic-force microscopy (AFM) was successfully applied to monitor the growth of individual poly(hydroxyethyl methacrylate) chains synthesized by surface-initiated RAFT polymerization. As polymer chains prepared via RAFT polymerization exhibit a high end-group fidelity, the terminal RAFT moieties can be transformed into thiol groups via aminolysis, thus the AFM tip (made of gold) was able to tether to the polymer chain end and measure the contour length of individual polymer chains [12]. However, besides the low throughput, AFM characterizations can only be performed on polymers post-synthetically. To picture the whole process of the polymer formation, magnetic tweezers was applied. The polymer chain was tethered between the substrate and a magnetic bead via silane chemistry. The position evolution of the magnetic particle reflected the polymer chain extension and gave insights into the polymerization kinetics. In this study, magnetic tweezers revealed that with the presence of pulling force, the polymer chain growth exhibits wait-and-jump steps during ring-opening metathesis polymerization [118]. However, monitoring the chain prolongation with magnetic tweezers requires both ends of the growing polymer chain to be tethered, which means the polymer growth must proceed by insertion polymerization. This limits its application to other polymerization reactions [113]. In addition to the force-based techniques, fluorescence microscopy measurement provides an alternative approach to study polymerization. For example, by adding fluorescently labeled monomers with low concentration (down to 10^{-14} M) into the reaction solution, Blum and coworkers observed the incorporation of individual monomers into polymer aggregates during ring-opening metathesis polymerization, providing information on the polymerization location and dynamics [119]. The same group then further explored the catalytic kinetics change in single particles and the distribution of such behavior in the sample with the same reaction system [120]. A recently developed method known as the coupled reaction approach toward super-resolution imaging enables the real-time optical sequencing of single synthetic copolymer chains by rendering reactions effectively fluorogenic [121]. However, despite the fluorescence label pushed the sensitivity down to the molecular level, it also causes inevitable limitations. For instance, the size of fluorescent labels, ranging from 200 to 1000 Da, can induce considerable perturbations in the molecular kinetics of a polymer, given that individual monomers typically weigh only around 100 Da.

3.1.4 iSCAT monitoring of single polymer chain growth

As previously discussed, iSCAT, a label-free, non-contact imaging technique with high spatio-temporal resolution, holds considerable promise for studying polymerization at the molecular level. It has also been employed as a form of mass photometry to investigate individual protein polymerization processes, such as α-synuclein aggregation and actin filament elongation [50]. Consequently, applying iSCAT to examine polymer growth prepared via PICAR ATRP appears to be a reasonable choice. As shown in Fig. 3.4A, the initiator is immobilized onto the glass coverslip, and with the presence of SP, the polymerization is initiated upon LED irradiation. Fig. 3.4B gives a simplified illustration of observing the growth of individual poly(*N,N*-dimethylacrylamide) (PDMA) polymer chains, with the molecular weight of the polymer chain reaching the detection limitation of iSCAT (70 kDa), we should be able to observe particles gradually appear on the surface. The contrast of individual polymer chains can then be followed as the reaction proceeds. We expect to observe that the contrast evolution of individual polymer chains follows a similar trend as demonstrated in the calibration curve in Chapter 2.

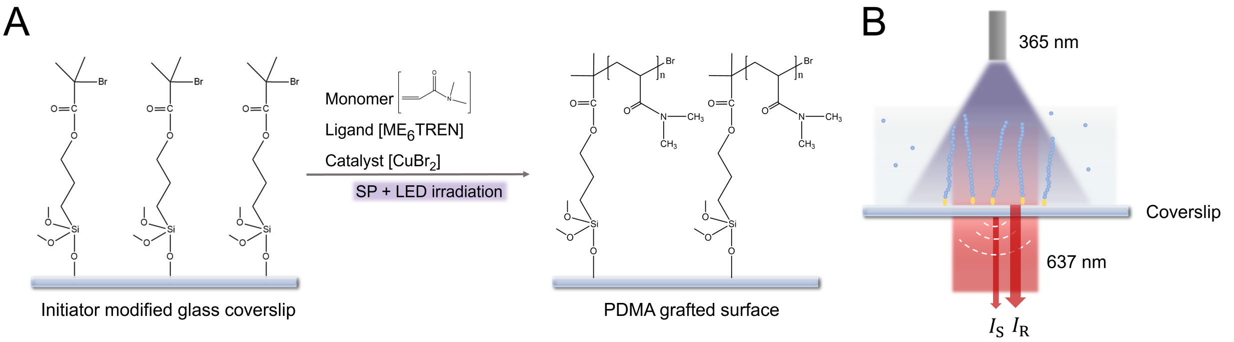

Figure 3.4: **Schematic illustration of iSCAT observation of individual polymer chain growth.**
(A) Surface-initiated PICAR ATRP of PDMA with the presence of air. **(B)** For PICAR ATRP of PDMA growth, initiators (yellow) were immobilized on the glass coverslip, with monomer (blue), catalyst, ligand and SP added. 365 nm LED illumination was delivered via a liquid light guide (pE4000/pE1906, CoolLED, UK) placed 10 mm above the reaction chamber. Interference between light scattered from a growing polymer chain (I_S) and light reflected at the reaction solution-glass interface (I_R) is detected.

In conclusion, the primary objective of this chapter is to utilize iSCAT as a mass photometry for real-time reporting of the contrast of individual polymer chains. By leveraging the relationship between contrast and the mass of the object, we can extract valuable kinetic information about the growth of individual polymer chains, revealing the heterogeneous kinetic information that is commonly inaccessible by other techniques.

3.2 Materials and methods

3.2.1 Materials

Before use, *N,N*-dimethylacrylamide (DMA, 99% pure, average molecular weight 99 g mol^{-1}) monomer was passed over a basic alumina (Al_2O_3, Brockmann I) column to remove the inhibitor. *N*-isopropylacrylamide (NIPAM, 97%), copper (II) bromide ($CuBr_2$, 99% pure), tris[2-(dimethylamino)ethyl]amine (Me_6TREN, 99%), 2-hydroxyethyl 2-bromoisobutyrate (HOBiB, 95%), sodium pyruvate (SP, $C_3H_3NaO_3$, ≥99%), sodium bromide (NaBr, ≥99.0%), sodium phosphate dibasic (Na_2HPO_4, ≥99.0%) and potassium phosphate monobasic (KH_2PO_4, ≥99.0%), dimethylformamide (DMF, 99.8%) and deuterium oxide (D_2O, 99.9 atom % D) were purchased from Merck and used as received. 3-(trimethoxysilyl)propyl 2-bromo-2-methylpropanoate (≥

95% pure) was bought from Gelest and used as received. DMA, NIPAM, ligand (Me_6TREN), and the bulk initiator (HOBiB) were sealed and kept at 4 °C, while the catalyst ($CuBr_2$), SP, and 3-(trimethoxysilyl)propyl 2-bromo-2-methylpropanoate were stored under vacuum (in a desiccator containing silica gel beads) at room temperature.

3.2.2 PICAR ATRP: polymer synthesis and characterization

Polymer synthesis in bulk

The protocol outlined in reference [112] was used in this study. As pH plays an important role in controlling the polymerization during PICAR ATRP, a phosphate-buffered saline solution containing bromide anions (Br-PBS) was used. To prepare Br-PBS solution, NaBr (14.08 g, 136.8 mM), KBr (0.32 g, 2.69 mM), Na_2HPO_4 (1.44 g, 10.14 mM) and KH_2PO_4 (0.24 g, 1.76 mM) were added into a 100 mL volumetric flask with water filled to the mark. Then the buffer was filtered with a 0.22 µm syringe filter and stored at 4 °C.

A series of reactions were conducted with different conditions using the following general protocol. HOBiB (16.9 mg, 0.08 mM in 1.0 mL of DMF) and CuBr2 (17.9 mg, 0.08 mM in 20.0 mL of DMF) stock solution were prepared, then Me_6TREN (27.6 mg, 0.12 mM) was added into 5 mL $CuBr_2$ stock solution to form $CuBr_2$/Me_6TREN stock solution. A 7 mL glass vial equipped with a magnetic stir bar was charged with SP (44.0 mg, 0.4 mM), NaBr (41.2 mg, 0.4 mM), filtered DMA/NIPAM (317/362 mg, 3.2 mM) and sealed with a rubber septum then purged with nitrogen for 5 min. 3.2 mL DI water, 0.4 mL Br-PBS solution, 0.2 mL CuBr2/Me6TREN stock solution, and 0.2 mL HOBiB stock solution were mixed and added into the vial through a syringe. The reaction was initiated with LED irradiation (365 nm, 1.17 mW cm^{-2}). Samples were taken from the reaction mixture at predefined timed intervals for nuclear magnetic resonance (NMR) spectroscopy analysis to determine the monomer conversion rate.

Proton nuclear magnetic resonance (^{1}H NMR) spectroscopy analysis

0.15 mL samples of the reaction mixture were periodically withdrawn, added into 0.5 mL D_2O, and taken for ^{1}H NMR spectroscopy analysis. All spectra were collected by a Bruker Avance

400 MHz spectrometer. The data was analyzed in Mestrenova×64 software.

iSCAT monitoring of individual PDMA chain formation

It needs to be noted that, DMA was chosen as the monomer instead of NIPAM for surface-initiated polymerization observed by iSCAT. This modification was made because the polymer poly(*N*-isopropylacrylamide) (PNIPAM) exhibits temperature-responsive behavior, with a lower critical solution temperature in water at approximately 32 °C [122]. PNIPAM undergoes a phase transition and conformational changes as the temperature exceeds its critical point. Considering that laser-induced heat during iSCAT observation could trigger this phase transition, we selected DMA as the monomer, which has a slight variation in the side chain but its polymer is more stable at elevated temperatures compared to PNIPAM.

Plasma-cleaned coverslips and spacers were prepared following the same protocol introduced in Chapter 2. To immobilize the initiator onto the surface, plasma-cleaned coverslips were soaked in the 17 nM 3-(trimethoxysilyl)propyl 2-bromo-2-methylpropanoate anhydrous toluene solution at room temperature for at least 12 h. They were then rinsed with toluene to remove the unattached initiator and dried with a stream of nitrogen before use. Then a cleaned spacer was mounted onto the initiator-modified coverslip to form the reaction chamber, and the reaction solution (prepared following the same protocol as the bulk reaction) was added into the reaction chamber with the second coverslip placed on top to seal the reaction (Fig. 3.2). Then the reaction chamber was placed above the objective with the focus adjusted onto the surface, and iSCAT recording started immediately after the LED irradiation. 365 nm LED with power set to 1.17 mW cm^{-2} was delivered via a liquid light guide (pE4000/pE1906, CoolLED, UK) placed 10 mm above the reaction chamber as shown in Fig. 3.4B. It's worth mentioning that as our observation is still constrained by the diffraction limit, the maximum surface polymer density needs to be relatively low, which means a low surface initiator concentration (17 nM) should be used. However, as reported previously, without or with insufficient initiator addition in the system, SP is able to initiate the reaction independently, leading to a loss of control over the reaction [112]. Thus, the initiator used for bulk reaction (HOBiB) was also added to the reaction solution for the surface-initiated PICAR ATRP.

3.3 Results and discussion

3.3.1 Bulk synthesis of PNIPAM

PNIPAM was synthesized in bulk following the procedure reported previously [112]. The reaction was carried out in Br-PBS buffer with molar ratios of [NIPAM]/[HOBiB]/[$CuBr_2$]/[Me_6TREN] set at 2000/1/0.5/3, with the addition of 0.4 mM of SP. Samples were withdrawn before and every 6 minutes after the initiation of the reaction, which were then mixed with D_2O and set for NMR spectroscopy analysis immediately. ^{1}H NMR spectroscopy provides quantitative information about the composition of the sample, it is a fast and convenient way for assessing the degree of polymerization and conversion. Without LED irradiation, only NIPAM monomer can be detected in the reaction solution as shown in Fig. 3.5A. Using the sample collected at 30 min of reaction as an example, the previously absent characteristic resonance peaks of PNIPAM, such as methylene (peak e, 1.2-1.7 ppm) and methine (peak f, 2.3-2.7 ppm) peaks appear on the spectra (Fig. 3.5B), indicating the successful formation of PNIPAM polymers after 30 min of LED irradiation. DMF was used in the reaction which can act as an internal standard to compare the disappearance of vinyl peaks against the DMF peak. After integration, peak 'a' was chosen to calculate the fractional monomer conversion as shown in Eq. 3.1:

$$f_{\mathrm{conv}} = \frac{I_0 - I_{\mathrm{t}}}{I_0} \times 100\%, \tag{3.1}$$

where, I_0 represents the integrated area of the monomer peak at the initial time, I_{t} represents the integrated area of the monomer peak at time t.

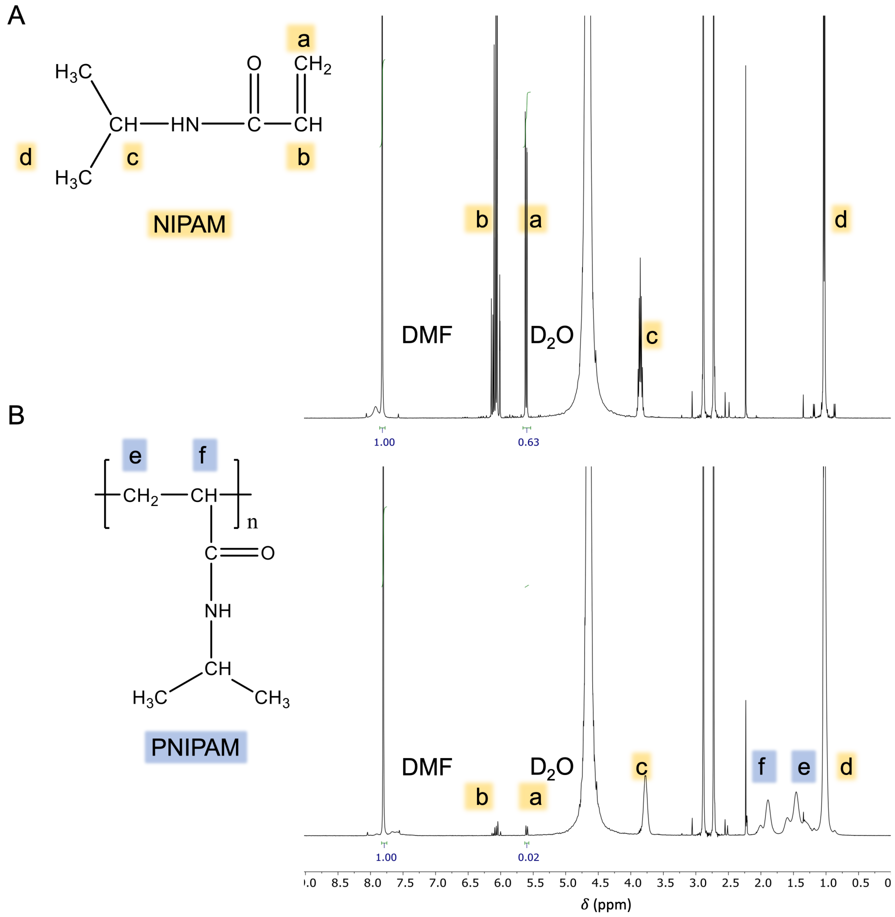

Figure 3.5: **PNIPAM formation monitored by ^{1}H NMR spectroscopy.**
The reaction was performed in a Br-PBS buffer with [NIPAM]/[HOBiB]/[$CuBr_2$]/[Me_6TREN] molar ratios of 2000/1/0.5/3, in the presence of SP (0.4 mM). Samples collected at predetermined time points were added into D_2O and then sent for NMR spectroscopy analysis immediately. **(A)** NMR spectrum of the sample collected before LED irradiation. **(B)** NMR spectrum of the sample collected after 30 min of LED irradiation.

Based on Eq. 3.1, the monomer conversion evolution as the function of time can be extracted as shown in Fig. 3.6A. It can be noted that there is a lagged period with no polymer formation in the first 6 minutes. This is because the Cu^I/L formed during this period was consumed by the oxygen in the system. After full elimination of oxygen, the monomer conversion gradually increased with time, and the reaction basically completed after 30 minutes with a fractional monomer conversion of 96.8%, closely aligning with previously reported values [112]. Based on the conversion rate the molecular weight of PNIPAM can be further estimated following the equation shown below:

$$M = \frac{[M]_0}{[I]_0} \times f_{\mathrm{conv}} \times M_{\mathrm{w}}(M), \tag{3.2}$$

herein $[M]_0$ and $[I]_0$ are the initial monomer and initiator concentration, respectively. $M_{\mathrm{w}}(M)$ is the molecular weight of the monomer, in this case, the molecular weight of NIPAM is 113.2 g mol^{-1}. Thus the molecular weight evolution as the function of time can be further generated as shown in Fig. 3.6B. As mentioned before the detection limit of our iSCAT setup is around 70 kDa (the orange dashed line), which means that with these reaction conditions, we can use iSCAT to track most of the stages involved in this polymerization.

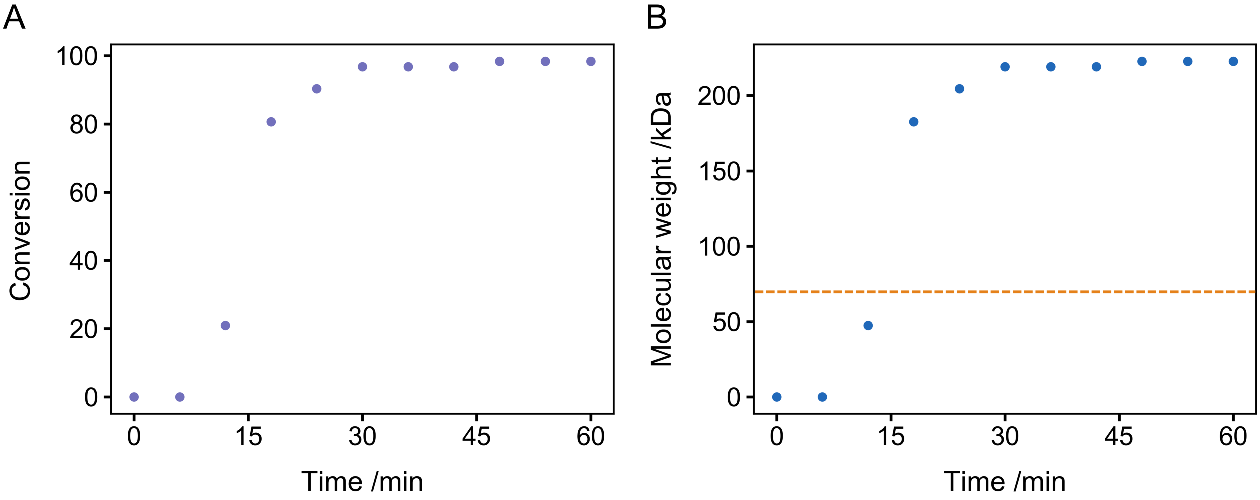

Figure 3.6: **Monomer conversion and corresponding molecular weight evolution over time.**
(A) Monomer conversion *vs.* time. **(B)** Molecular weight evolution of PNIPAM as the function of time (detection limit of our setup is marked out in the orange dashed line).

However, when the reaction was moved onto the surface and monitored with iSCAT, the 637 nm laser-induced heating made the observation problematic. PNIPAM is a temperature-responsive polymer with a lower critical solution temperature in water at approximately 32 °C [122]. Under laser illumination, it undergoes a phase transition, thus DMA with a slight side chain variation but more stable under elevated temperature was chosen for the following studies.

3.3.2 Bulk synthesis of PDMA

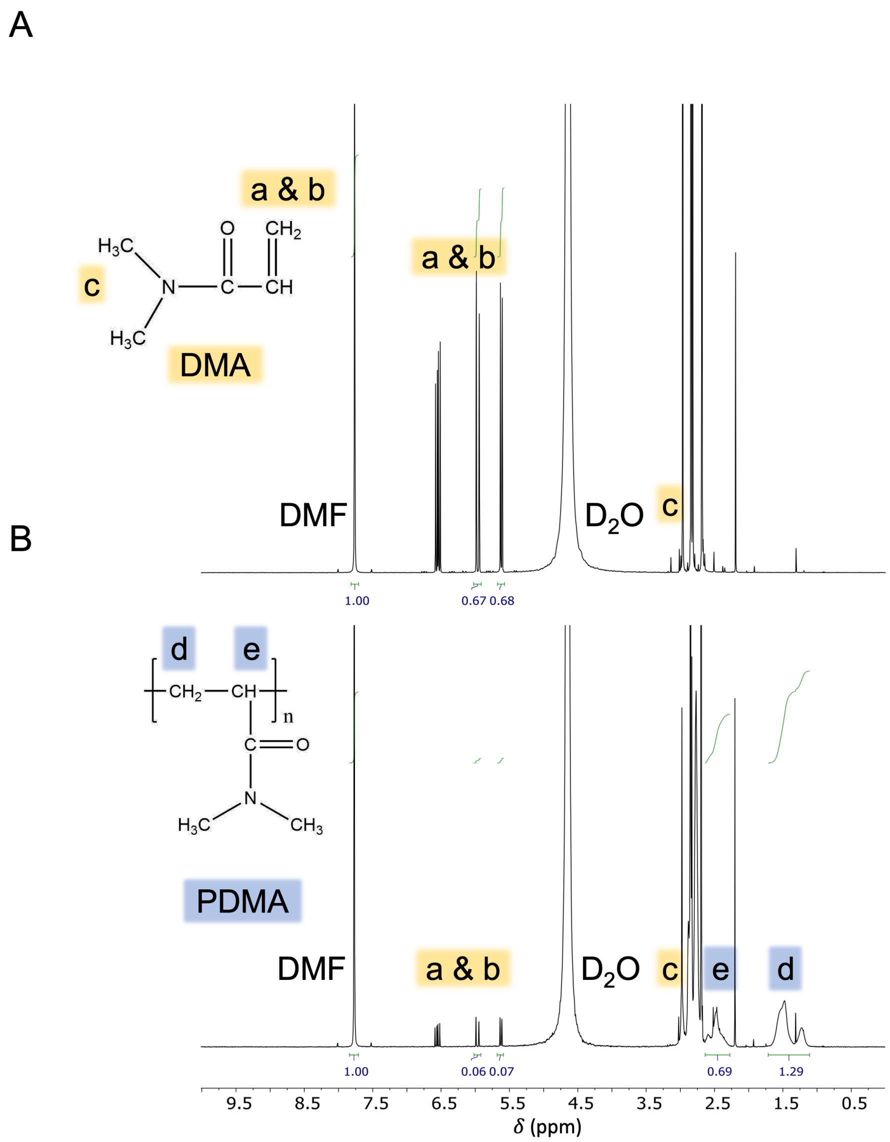

Figure 3.7: **PDMA formation monitored by ^{1}H NMR spectroscopy.**
The reaction was performed in a Br-PBS buffer with [DMA]/[HOBiB]/[$CuBr_2$]/[Me_6TREN] molar ratios of 2000/1/0.5/3, in the presence of SP (0.4 mM). Samples collected at predetermined time points were added into D_2O and then sent for NMR spectroscopy analysis immediately. **(A)** NMR spectrum of the sample collected before LED irradiation. **(B)** NMR spectrum of the sample collected after 30 min of LED irradiation.

The same reaction was repeated, with the monomer replaced with DMA, samples prior to the polymerization reaction (before LED irradiation) and after 30 min of reaction (after 30 min of LED irradiation) were collected and mixed with D_2O and sent for NMR spectroscopy analysis. Similarly, without LED irradiation, only DMA monomer can be detected in the reaction solution

(Fig. 3.7A), and after 30 min of reaction, the previously absent characteristic resonance peaks of PDMA can be observed in the spectra as displayed in Fig. 3.7B. By comparing the disappearance of vinyl peaks (peak 'd' in this case) against the DMF peak, we can know that after 30 min of LED irradiation, 91% of the monomer has been converted into polymer with an estimated molecular weight of 180 kDa. As a result, replacing the monomer with DMA still produced a polymer with a molecular weight above the detection limit. Therefore, this reaction can be adapted for surface reactions under iSCAT observation.

3.3.3 iSCAT monitoring of PDMA formation in real-time

The same reaction conditions were then applied to conduct surface-initiated PICAR ATRP. As introduced in the mechanism of PICAR ATRP, SP can initiate the reaction independently, without requiring any initiator, which leads to the loss of control of the reaction. Thus, alongside the surface initiator used in the reaction, HOBiB was added to the reaction solution. The reaction solution was prepared with [DMA]/[HOBiB]/[$CuBr_2$]/[Me_6TREN] with molar ratios of 2000/1/0.5/3 and the addition of 0.4 mM SP in Br-PBS buffer solution. A 150 µL reaction solution was added onto an initiator-modified coverslip (plasma-cleaned coverslips soaked in 17 nM surface initiator solution overnight). Before LED irradiation, dark particles can already be observed with iSCAT, and their contrast remained constant throughout the reaction, as shown in Figure 3.8A. The contrast of most particles observed at 800 s remained the same in the following time points (no observable variation can be seen in the stacks from 0 to 795s, which are not displayed here). To confirm that no polymer formation occurred before LED irradiation, a 150 µL reaction solution was sent for NMR spectroscopy analysis. The result, as shown in Figure 3.8B, confirms no polymer formation, indicating that the particles observed at this stage were not polymers. These particles may have been introduced from the reaction solution or contamination introduced during surface preparation, and since they remained static throughout the reaction, they can be considered as background and easily removed via data process. iSCAT recording started immediately after LED irradiation, and during the first 800 seconds, no observable changes in particle density or contrast were noted. After 800 seconds, as shown in Figure 3.8A, new particles gradually appeared on the surface, with their contrast changing from negative (dark) to positive (bright) over time. The contrast reversal observed here follows the same trend as the calibration curve, which will be discussed in detail in Chapter 4. The lagged time observed in the bulk reaction (Fig. 3.6) is also evident in the formation of particles. The particle formation started after the complete removal of oxygen from the solution. After recording, the reaction solution was withdrawn from the reaction chamber and sent for NMR spectroscopy analysis. Figure 3.8C indicates the successful formation of PDMA after 30 minutes of LED irradiation. The monomer conversion is approximately 79%, and the estimated molecular weight of the produced PDMA is 156 kDa, which is above the detection limit of iSCAT.

From Fig. 3.8A, it is evident that the detected particles generate strong signals comparable to the contrast observed in the AuNP standard from Chapter 2. This outcome is unexpected, as polymer particles with estimated molecular weights should typically yield much weaker scattering signals compared to AuNPs. As a result, before proceeding to data analysis, it is reasonable to confirm that the growing particles observed here are polymer particles. However, as the label-free technique, iSCAT cannot confirm these growing particles are PDMA polymers, thus more control reactions were conducted. The same reaction without monomer addition was repeated. As displayed in Fig. 3.9, even in the absence of DMA, particle growth was still observed. Based on the most commonly used method for metal nanoparticle (NP) preparation, we assume the reduction of Cu^{II} to Cu^{I} during the polymerization created an ideal condition for copper NP formation [123]. As a result, we assume particles observed in Fig. 3.8 and Fig. 3.9 were copper NPs. To further confirm this, the same control reaction was conducted without the addition of copper catalyst. Under these conditions, no particle formation can be observed. In addition, it can be noted that the presence of monomer also affect the formation of NPs. NPs formed without the addition of monomer (Fig 3.9) turn to be more uniform with lower contrast. We assume that the addition of DMA monomer affect the pH of the reaction solution, thus alter the formation of copper NPs. As a result, optimizing the reaction conditions to prevent the formation of NPs is necessary. This is particularly crucial for iSCAT monitoring because label-free detection poses a great challenge in differentiating between polymer particles and copper NPs. In addition, as the metallic NP, copper NPs produce much stronger scattering signals than soft matter like polymers. The presence of copper NPs poses a substantial challenge to the detection of weak scatters.

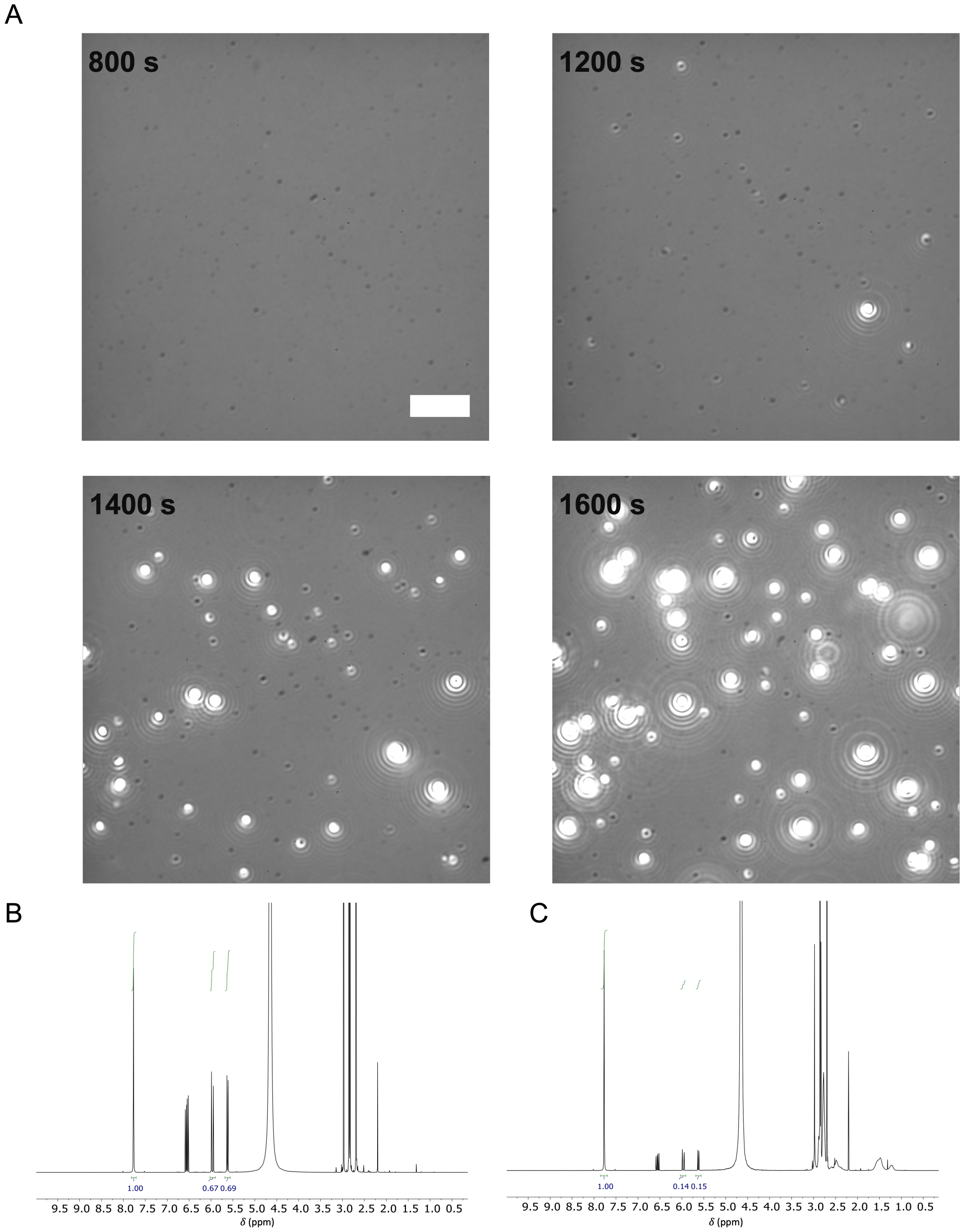

Figure 3.8: **Real-time iSCAT observation of individual polymer chain growth.** The reaction solution is composed of [DMA]/[HOBiB]/[$CuBr_2$]/[Me_6TREN] with molar ratios of 2000/1/0.5/3 and an addition of 0.4 mM SP. A laser power density of 0.004 mW µm^{-2} at 637 nm, exposure time 350 µs, and overall time-lapsed frame rate 5 s^{-1} were chosen. LED intensity was set to: 1.17 mW cm^{-2}. **(A)** Montage of iSCAT images collected during PICAR ATRP (scale bar: 3 µm). **(B)** NMR spectrum of sample collected before LED irradiation. **(C)** NMR spectrum of sample collected after 30 min of LED irradiation.

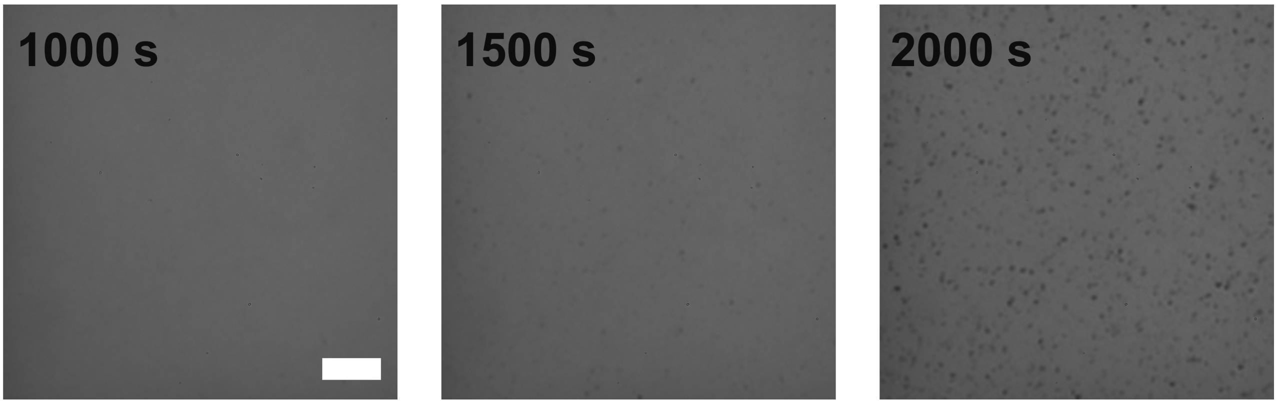

Figure 3.9: **Formation of copper nanoparticles.**
Reaction and recording conditions were kept the same as in Fig. 3.8, with no monomer addition. Montage of iSCAT images collected during PICAR ATRP without DMA addition (Scale bar: 3 µm). A laser power density of 4 µW µm^{-2} at 637 nm, a camera exposure time of 350 µs, and an overall time-lapsed frame rate of 5 s^{-1} were chosen. LED intensity was set to: 1.17 mW cm^{-2}.

3.4 Summary and future work

In this chapter, we first explored the reaction conditions in bulk that produce polymer with molecular weight above the detection limit of our setup. Then we tried to adapt these reaction conditions onto surface and observe individual polymer chain growth with iSCAT. However, under the reductive environment, copper NPs were also produced together with the polymers. This presents a challenge for our study. Firstly, as a label-free detection technique, iSCAT lacks specificity, making it unable to distinguish between the detected objects. Additionally, the metal NPs produce much stronger scattering signals compared to the polymer molecules. The presence of copper NPs further complicates the detection of polymer molecules. As a result, rather than continuing with the current project, we chose to first explore the potential for controlling NP formation using iSCAT. This approach may provide valuable insights into minimizing NP formation during polymerization, thereby offering guidance for designing optimal polymerization reaction conditions.

Meanwhile, metal-free polymerization reactions offer an alternative approach for this study [124–126]. In these studies, metal catalysts were replaced by photocatalysts which allows the polymerization to proceed upon photo irradiation in the presence of air.

Chapter 4

Real-time monitoring and control of nanoparticle formation

Under a reductive environment, metal ions in a higher oxidation state will be reduced to their lower state and undergo nucleation and autocatalytic growth which finally leads to the formation of nanoparticles. In Chapter 3, in the presence of sodium pyruvate, copper nanoparticles were generated upon LED irradiation. The successful observation of individual copper nanoparticle formation with iSCAT inspired us that it can be used to further explore the growth kinetics of individual nanoparticles. A systemic study of metallic nanoparticle kinetics not only provides improved reproducibility and scalability in engineering complex nanomaterials but also is useful for us to better understand this system and find a way to inhibit nanoparticle formation during polymerization.

This work has recently been published: Guo, Y., Walter, V., Vanuytsel, S., Parperis, C., Sengel, J. T., Weatherill, E. E., & Wallace, M. I. (2023). Real-Time Monitoring and Control of Nanoparticle Formation. *Journal of the American Chemical Society*, 145(29), 15809-15815.

4.1 Introduction

4.1.1 Importance of controlling nanoparticle size and growth in nanomaterial design

Reducing the size of a material to the nanoscale would give rise to new physicochemical properties that are significantly different from those of bulk substances [127]. Due to the unique size-dependent features, including mechanical, electromagnetic and optical properties [128], nanoparticles (NPs) have drawn much attention, offering significant advances; impacting areas as varied as catalysis [129–131], drug delivery [132–135], photothermal therapy [136, 137], and biosensing [138–141]. Given the intimate link between nanoscopic dimensions and their distinctive properties, precise control over NP size and size dispersity is critical to their effective applications [142–144]. As a result, designing complex NPs with specific properties necessitates a comprehensive understanding of NP growth and the means to control it.

4.1.2 Techniques for NP characterization

Despite the significant role that NPs have played in the development of iSCAT, iSCAT has not yet been applied for NP characterization. Compared to iSCAT, currently applied techniques are facing many limitations. For example, conventional techniques such as light scattering [145] and absorption spectroscopy [146] are commonly used in NP characterization, involving averaging over all the detected particles that appear in the sample, and therefore cannot fully capture the diversity of the objects. To reach a higher spatial resolution with the ability to resolve individual NPs. Electron microscopy was introduced, which can directly measure the size and morphology of individual NPs. However, as a solid-state technique, NPs are required to be separated from the solution and dried before imaging, which may lead to continued growth or agglomerate formation under the concentrated environment and poses a great challenge in kinetic application [147–149].

Numerous techniques have been devoted to bridging the gap between well-characterized (yet ensemble) kinetics and the nanoscopically-resolved (albeit static) imaging of single particles.

The same optical properties that provide ensemble-averaged readout of particle growth were also applied to individual NPs [150]. For instance, the growth and oxidation of gold nanorods can be monitored via the alteration in surface plasmon resonance induced by changes in their length [151, 152]. Although powerful, such methods rely on the presence of a length-dependent plasmon resonance. The application of photothermal microscopy offers a different route in NP characterization, involving the detection of the signal arising from temperature-induced refractive index changes. However, the low temporal resolution (order of the millisecond per pixel) limits its kinetic applications [36, 37]. Wide-field photothermal microscopy offered an improved acquisition rate but at the expense of some sensitivity [38–40]. Similarly, atomic force microscopy used to study AuNP growth is also limited by its relatively slow temporal resolution [153]. Looking forward, recent advances in liquid-cell electron microscopy provide one promising route to characterize NP *in situ* with exquisite spatial resolution [154, 155], but at the expense of complex, expensive instrumentation and low throughput.

4.1.3 iSCAT monitoring of individual NP formation in real-time

As repeatedly discussed in this thesis, iSCAT demonstrates the capability of real-time reporting on dynamic processes with both high sensitivity and high spatio-temporal resolution. Its inherent label-free capability enables it to monitor kinetics across a broad range of timescales, encompassing both rapid and slow processes. Combining the results acquired in Chapters 2 and 3 (the AuNP calibration curve and observation of copper nanoparticle formation during polymerization), it is fair to consider iSCAT as a potential technique that can be used for NP characterization as well as monitoring individual NP formation.

In this study, AuNPs, which are the most extensively researched NPs in various fields, were chosen as the model system to test our method. AuNPs are the most commonly used labels in iSCAT imaging, as they exhibit strong scattering efficiency which enables highly sensitive and real-time tracking at the nanoscale [66, 156]. Turkevich method was first chosen to prepare AuNPs. Within this method, sodium citrate serves as both a reducing agent and a capping agent during the formation of AuNPs [157, 158]. In addition, photoreduction is not a new concept for NP preparation [159–162]. To achieve further control over the AuNP formation, photo-initiation was then introduced to provide spatio-temporal control and ambient initiation of NP generation. From Chapter 3, we know that sodium pyruvate can be an efficient photoreductant in NP generation and was incorporated in this study as well.

4.1.4 Knietics of NP formation

The kinetics of NP formation is described by a model suggested by Finke and Watzky (hereafter the FW-model), known as two-step nucleation–autocatalysis [163]. It discusses the relation between particle diameter and kinetics in detail (Eq. 4.1):

$$D = D_\mathrm{f}\left(1 - \frac{k_1 + k_2[\mathrm{A}]_0}{k_2[\mathrm{A}]_0 + k_1 e^{(k_1+k_2[\mathrm{A}]_0)t}}\right)^{\frac{1}{3}}, \tag{4.1}$$

Where D is the diameter of an individual AuNP at a given time t, D_f is the final diameter of that AuNP, k_1 and k_2 are the rate constants for nucleation and autocatalytic growth of the corresponding AuNP, and $[\mathrm{A}]_0$ represents the initial gold precursor concentration used for the reaction. Fig. 4.1 gives an example of how the diameter of a single AuNP is expected to evolve with time.

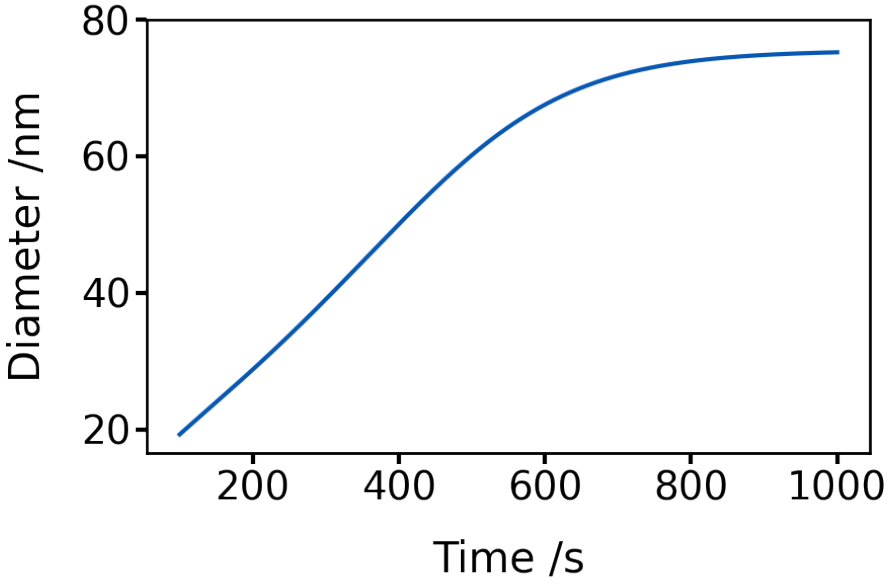

Figure 4.1: **Model representation: Temporal evolution of the particle diameter (D) with respect to time (t).**
For demonstration, $[\mathrm{A}]_0$, D_f, k_1 and k_2 with values of 0.35×10^{-3}, 75.5, 1.1×10^{-4}, and 25.3, respectively, were applied to Eq. 4.1.

As explained in Chapter 2 (Fig. 4.2), the relation between the iSCAT contrast and the diameter of the AuNPs is given by Eq. 2.3.

$$c = \beta^2 \sigma_{\text{scat}} - 2\beta \sqrt{\sigma_{\text{scat}}} \sin\varphi \tag{2.1}$$

$$\sigma_{\text{scat}} = \frac{8\pi^3}{3} \left(\frac{n_{\text{m}}}{\lambda}\right)^4 \alpha^2 = \frac{2\pi^5}{3} \left(\frac{n_{\text{m}}}{\lambda}\right)^4 \left(\frac{n_{\text{p}}^2 - n_{\text{m}}^2}{n_{\text{p}}^2 + 2n_{\text{m}}^2}\right)^2 D^6 = P_1 D^6 \tag{2.2}$$

$$c = \beta^2 P_1 D^6 - 2\beta \sqrt{P_1} D^3 \sin\varphi \tag{2.3}$$

Figure 4.2: **Revision of equations illustrating the relationship between iSCAT contrast and nanoparticle size (Chapter 2).**
c is contrast detected by iSCAT, σ_{scat} is particle scattering cross-section, β is a proportionality constant describing the instrument sensitivity, φ is the phase shift between reference and scattered fields, λ is the wavelength of illumination source, n_{p} and n_{m} are refractive indices of the particle and the surrounding medium, respectively, D is particle diameter and P_1 is an experimental parameter introduced to simplify the expression.

Combining Eq. 2.3 and Eq. 4.1, the relation between iSCAT contrast and kinetics can be established as illustrated by Eq. 4.2:

$$c = \beta^2 P_1 \left(D_{\text{f}}^3 \left(1 - \frac{k_1 + k_2[\text{A}]_0}{k_2[\text{A}]_0 + k_1 e^{(k_1 + k_2[\text{A}]_0)t}}\right)\right)^2 - 2\beta \sqrt{P_1} D_{\text{f}}^3 \left(1 - \frac{k_1 + k_2[\text{A}]_0}{k_2[\text{A}]_0 + k_1 e^{(k_1 + k_2[\text{A}]_0)t}}\right) \sin\varphi. \tag{4.2}$$

This equation describes how the real-time contrast for the individual NPs would be expected to evolve, with a distribution of individual rate constants that change with reaction conditions can be acquired.

This study proved that individual particle growth kinetics are well-described by the two-step nucleation–autocatalysis model reported previously. Furthermore, we successfully combined spatially patterned activation of the photoreductant sodium pyruvate with iSCAT microscopy to achieve fast, label-free monitoring and control of hundreds of AuNPs in real-time.

4.2 Materials and methods

4.2.1 Materials

Gold(III) chloride trihydrate ($HAuCl_4 \cdot 3H_2O$, $\geq$ 99.9%), sodium citrate tribasic dihydrate ($Na_3C_6H_9O_9 \cdot 2H_2O$), sodium pyruvate (SP, $C_3H_3NaO_3$, $\geq$ 99%) and poly(ethylene glycol) (PEG, averaged molecular weight: 10000 g mol^{-1}) were purchased from Merck and used as received.

4.2.2 iSCAT monitoring of AuNP growth

Instrument construction

An identical iSCAT setup employed in Chapter 2 for instrument calibration was also utilized to monitor the formation of AuNPs prepared via citrate reduction. For photo-initiated AuNP formation, 365 nm LED illumination was delivered via a liquid light guide (pE4000/pE1906, CoolLED, UK) placed 10 mm above the reaction chamber as shown in Fig. 4.3A. To achieve a patterned illumination, this 365 nm LED was replaced with 405 nm single mode diode laser epi-illumination with a spatial light modulator (SLM, SN 4719, Meadowlark Optics, USA) inserted into the iSCAT beam path via a dichroic filter (Di01-E405, Semrock) to deliver an 8 × 8 µm checkerboard pattern as shown in Fig. 4.3B.

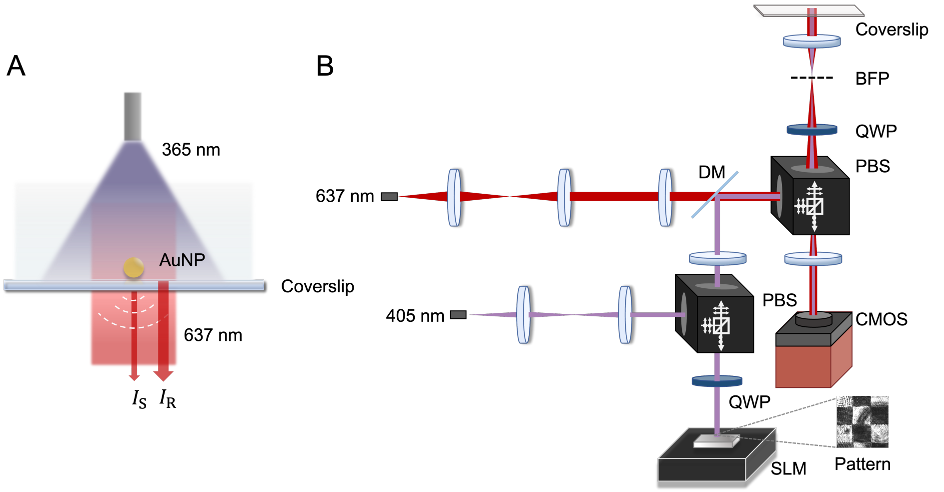

Figure 4.3: **Modified instrument setup for photocontrol of AuNP growth.** **(A)** Experiment setup for photocontrolled AuNP preparation. **(B)** iSCAT setup with a checkerboard pattern applied to the SLM. DM, dichroic mirror; PBS, polarizing beam splitter; QWP, quarter-wave plate; BFP, back focal plane; CMOS, complementary metal oxide semiconductor sensor.

Sample preparation

6 mM $HAuCl_4$ and 30 mM citrate/SP stock solutions were freshly prepared and stored on ice. The final concentration of $HAuCl_4$ and citrate/SP was varied by adjusting the volume of stock solutions added into each reaction to reach a final volume of 5 mL. To minimize AuNP formation before imaging, the reaction solution was mixed in a light-tight ice bath for 5 min. 150 µL of the reaction solution was then sealed in the reaction chamber using the second coverslip placed on top of the spacer (as shown in Fig. 3.2 in Chapter 3). Then the reaction chamber was placed above the iSCAT objective, with the focus adjusted onto the surface. For citrate reduction, a laser power density of 3 $\mu W\ \mu m^{-2}$ at 637 nm, a camera exposure time of 220 µs, and an overall time-lapsed frame rate of 1 s^{-1} were selected. For SP reduction, a laser power density of $0.37 \times 10^{-2}\ \mu W\ \mu m^{-2}$ at 637 nm, a camera exposure time of 100 ms and an overall time-lapsed frame rate of 2 s^{-1} were selected. The lower iSCAT laser power and longer exposure time in the SP experiments were chosen to minimize photoreduction of the absorption tail of the blue excitable SP by the longer (red) wavelength iSCAT beam.

4.3 Data analysis and fitting

Image analysis was performed using Python scripts developed in-house with the following steps. Please note that any modifications made in this data processing protocol compared to Chapter 2 have been highlighted in italics.

1. Image stacks were first cropped to remove the non-laser illumination area.
2. Dark counts subtraction was conducted by subtracting each frame by a frame recorded under the same conditions without laser illumination.
3. Laser intensity fluctuations were suppressed by dividing each frame by its modal pixel value.
4. *At the initial stage of the reaction, no particles are visible on the surface thus a static background (generally produced by interference between back reflections and imperfections in*

optical elements, nonuniform illumination, or nonuniform pixel response) can be obtained by applying a median average to these early frames (around 100 frames, depends on the reaction kinetics) as shown in Fig. 4.4 [164].

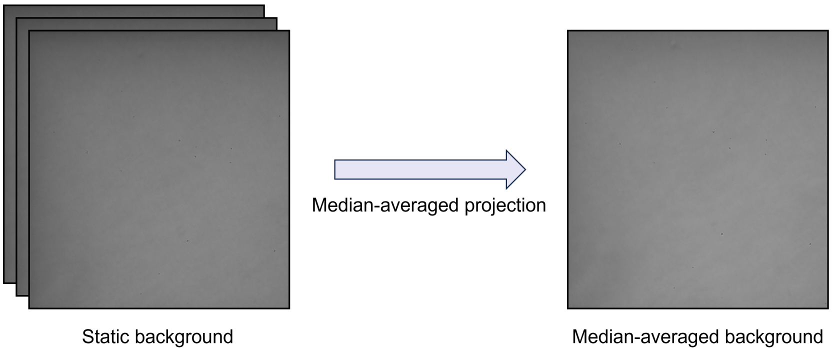

Figure 4.4: **Background estimation.**

5. *To eliminate the static signatures and improve sensitivity, we subtracted the median-averaged background generated in the last step from the image stacks. Subsequently, to convert image intensities into contrast values, the background-corrected image stacks were normalized via division with the median-averaged background. See more details in Fig. 4.5.*

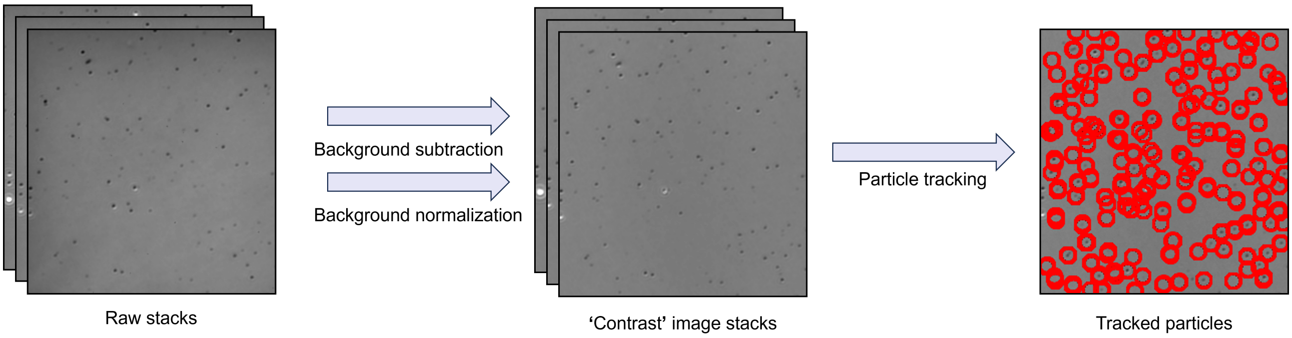

Figure 4.5: **Background correction, subtraction, and particle tracking.**

6. As shown in Fig. 4.5, particles can be located using the Python module TrackPy [73]. Particles were selected based on the following filtering conditions: the diameter of the circle used to detect and analyze spots was set to 21; a minimum separation between particles of 2× this diameter was specified; the minimum integrated brightness was set to 0.01 and a threshold with the value of 0.001 was applied. TrackPy returns information including the position and the size of tracked objects. A ROI was defined by using the

particle position as an origin and size as a diameter. Then within the ROI, the pixel value with the maximum absolute value was defined as contrast. As a result, from one recording over a hundred NP contrast evolution can be extracted as displayed in Fig. 4.6.

7. *The contrast evolution of each tracked particle can then be fitted to Eq. 4.2 using Scipy.optimize [76] with fixed parameters: In this case, the refractive indices of AuNPs* ($n_p = 0.18$) *and reaction solution (water,* $n_m = 1.33$) *are known, and* $\beta = 9.07 \times 10^7\ m^{-1}$ *has been determined from fitting the calibration curve in Chapter 2 (Fig. 2.3).*

8. *Fitted NP tracks were then filtered to exclude outliers corresponding to situations where two NPs were too close to be distinguished, or where the growth period was too short to provide enough data points for fitting.* k_1, k_2 *and* D_f *were restricted to positive values.* φ *was restricted between 0 to 2.3.*

9. *Once the fitting parameters of individual AuNPs, such as* k_1, k_2, D_f, *and* φ, *are extracted, plots with the distribution of these kinetic parameters under different reaction conditions can be generated (see examples in Fig. 4.9). Furthermore, by reintegrating* k_1, k_2, *and* D_f *into Equation 4.1, the diameter evolution over time can also be obtained (see examples in Fig. 4.7B).*

4.4 Results and discussion

4.4.1 Monitoring single AuNP growth

A typical NP growth experiment monitored by iSCAT can be conducted via the following procedure: 0.4 mM $HAuCl_4$ was mixed with 1 mM citrate solution on ice in the absence of light for 5 min. The mixture was then added to the chambered coverslip and sealed with the second coverslip before imaging (Fig. 3.2). Then the reaction chamber was placed above the iSCAT objective with focus adjusted onto the surface, followed by recording. A laser power density of 3 µW $µm^{-2}$ at 637 nm, an exposure time of 220 µs, and an overall time-lapsed frame rate of 1 s^{-1} were selected. With our setup, kinetics from over a hundred particles at a density of 0.5 particles per $µm^2$ can be acquired with a maximum temporal resolution of 100 µs. As shown in

Fig.4.6, 144 NPs contrast temporal evolution can be tracked simultaneously from one iSCAT recording. The contrast evolution of these particles, as illustrated in the figure, follows a similar trend. The variation in the starting time of growth can be attributed to nonuniform nucleation initiation.

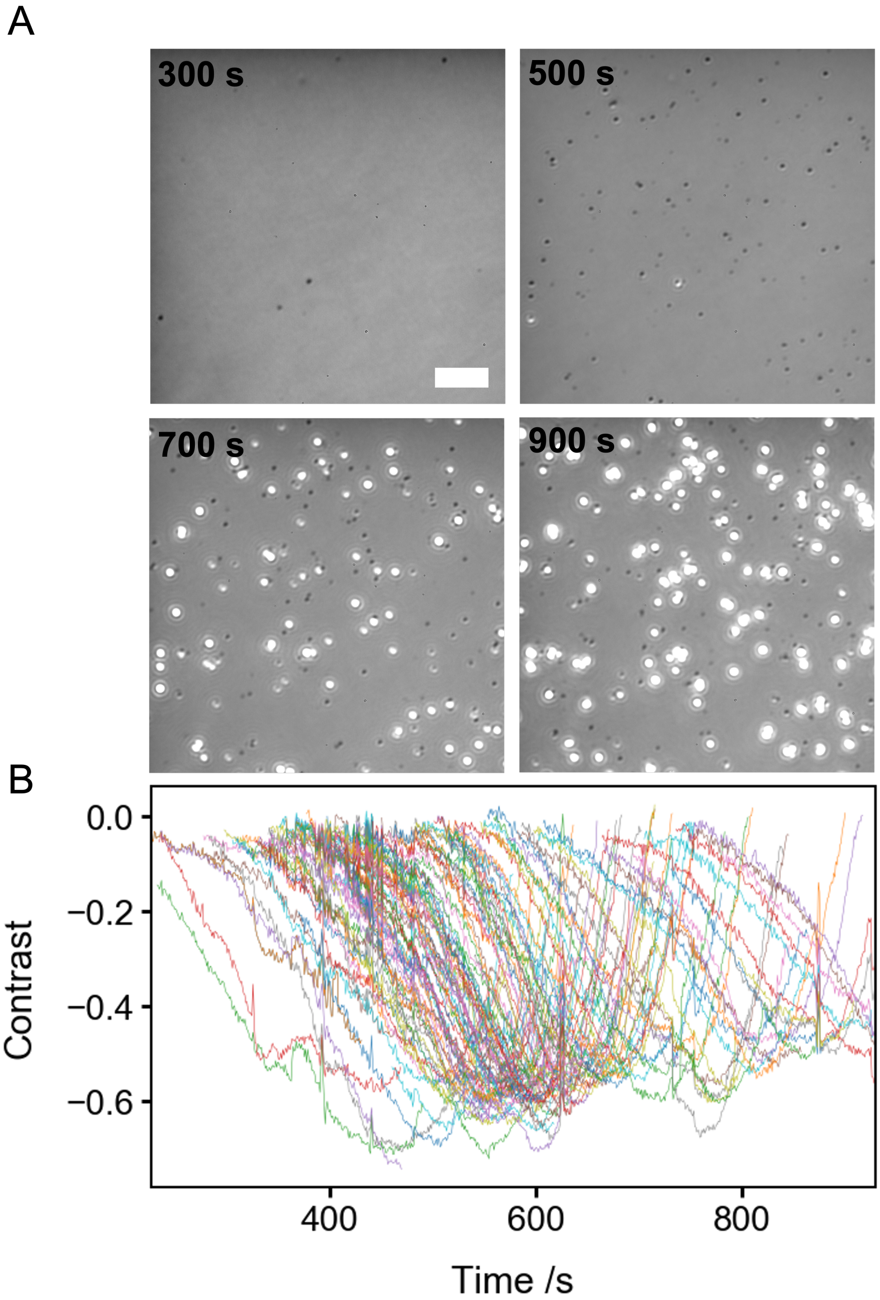

Figure 4.6: **iSCAT monitoring of individual AuNP growth.**
(A) Montage of images collected during AuNP growth using citrate as the reductant (scale bar 3 µm). As the size of the NPs increases, their contrast transitions from negative (dark) to positive (bright). When the contrast of the particle reaches a certain threshold, it saturates the camera under the imaging conditions, appearing as bright spots surrounded by a halo. **(B)** Contrast evolution of 144 AuNPs tracked from **A**.

The calibration curve in Chapter 2 displays a contrast reversal with the increase of NP size, which can also be observed in Fig. 4.6A and B. As shown in the snapshots taken from iSCAT recording across the reaction (Fig. 4.6A), as the reaction proceeds, dark particles gradually start to appear on the surface, and they become darker and darker before turning bright (the complete growth process is shown in Movie S1, provided in the appendix). In corresponding to the iSCAT contrast in Fig. 4.6B, they are first detected with contrast more negative than the overall background (dark spots) before becoming positive (bright spots). It should be noted that when a particle grows large enough, its contrast reaches a certain threshold that saturates the camera under the imaging conditions, causing it to appear as a bright spot surrounded by a halo as shown in Fig. 4.6A.

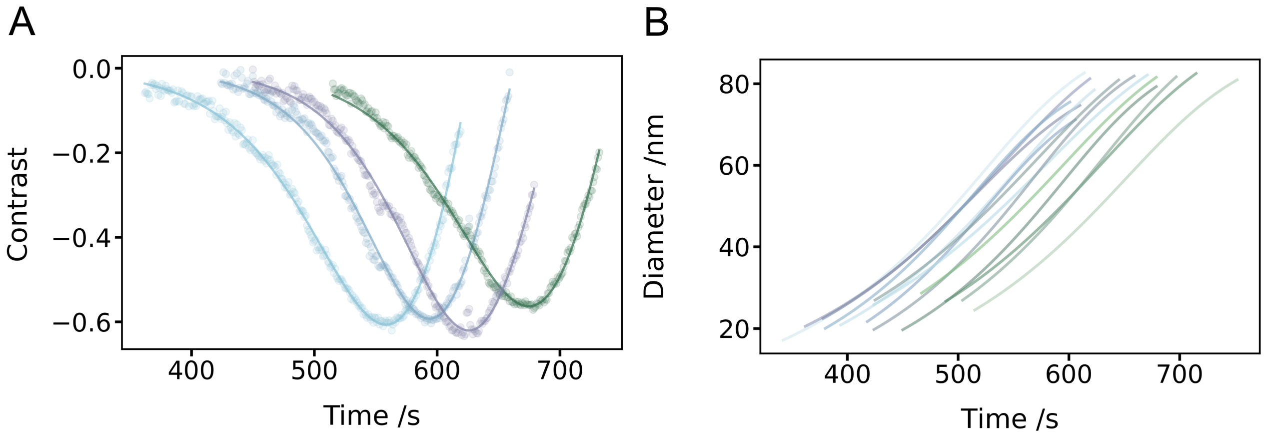

Figure 4.7: **Contrast and size evolution of individual AuNPs as the function of time.** **(A)** Contrast evolution of 4 particles fit to the FW-model (dots represent raw contrast reported by iSCAT, solid lines are fitted data, here are four examples taken from Fig. 4.6B). **(B)** Size evolution of 14 particles. Figure is taken from reference [13].

Fig. 4.7A displays four examples of individual AuNPs contrast evolution taken from Fig.4.6B. One data point in the curve represents the contrast of that AuNP at the corresponding time point. With the relationship between contrast and reaction kinetics having been previously established in Eq. 4.2, we can fit the data and extract the kinetic information of individual AuNPs. From the fitting results (solid line in Fig. 4.7A), we can know that NP growth kinetics are well-described by the FW-model. In addition, by incorporating the kinetic parameters obtained from the fitting into Eq. 4.1, we can acquire the evolution of the diameter of individual AuNPs as a function of time, as illustrated in Fig. 4.7B. It can be noticed that no growth information is displayed when the particle size exceeds 80 nm. This is because we selected imaging conditions to investigate the early stages of growth. Beyond 80 nm, the signal from individual NPs saturates the detector, and such data were excluded during processing.

Fig. 4.8 well explains why we can observe contrast reversal during particle growth. Increased particle size contributes to the change in the optical path length (from $L1$ to $L2$), thereby altering the travel distance of the scattering signal and ultimately causing a change in the phase shift ($\Delta\varphi_1$ to $\Delta\varphi_2$). Consequently, when a particle transitions from a small to a larger size, the interference between the scattering and reflecting signals shifts from destructive (dark) to constructive (bright).

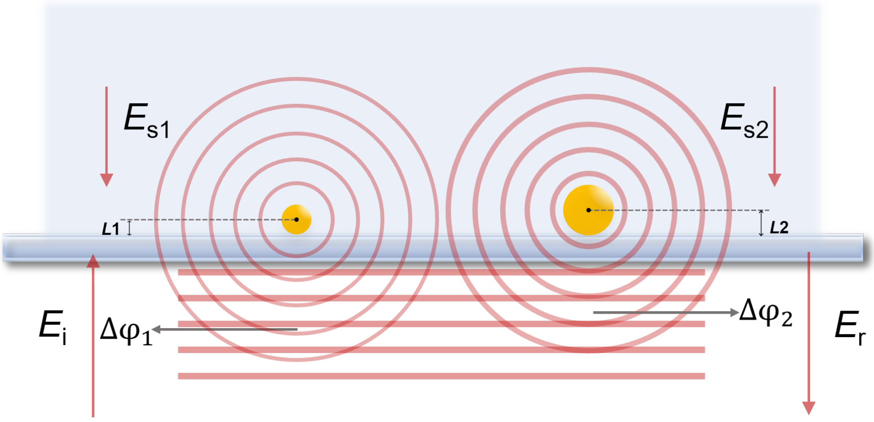

Figure 4.8: **The relation between particle size (D) and phase shift (φ).** E_i, E_s and E_r represent incident, scattered and reflected fields, respectively. $\Delta\varphi$ is the phase shift between the scattered and reflected fields and L is optical path lengths ($L1 < L2$, $E_{s1} < E_{s2}$).

In addition, this phenomenon can be explained mathematically, when the object of interest is relatively small, the second term in Eq. 2.3 dominates the iSCAT contrast calculation, resulting in the contrast becoming increasingly negative. However, as AuNPs gradually become larger (beyond approximately 60 nm), the pure scattering term gradually dominates the detected signal, leading to a positive contrast (bright spots). It is also worth mentioning that for wild-field iSCAT observation, the generation of interference signals requires the objects locate near/at the surface. It is undeniable that the surface may also contribute to the heterogeneity of the reaction. For example, in different regions of the coverslip, the microenvironments would vary. As a result, the interaction between each nanoparticle and surrounding molecules or external stimuli would also differ.

4.4.2 AuNP growth kinetics

Citrate reduction

With our method established, we can then examine the distribution of individual NP kinetics corresponding to the predictions of the FW-model. A series of experiments were conducted with varied reaction conditions. The impact of sodium citrate concentration on the autocatalytic growth rate constant (k_2) of individual NP formation was first studied. Each datum in Fig. 4.9A reports k_2 for a single AuNP produced from fitting with FW-mode. Meanwhile, fitting also produces the distribution of k_1, D_f and φ as shown in Fig. 4.9B to D. However, given our initial conditions, marked variation in these fitting parameters are not expected. Nevertheless, Fig. 4.9 highlights the underlying heterogeneity exists in the population of the kinetics of NP growth, which again proves the limitations of ensemble techniques.

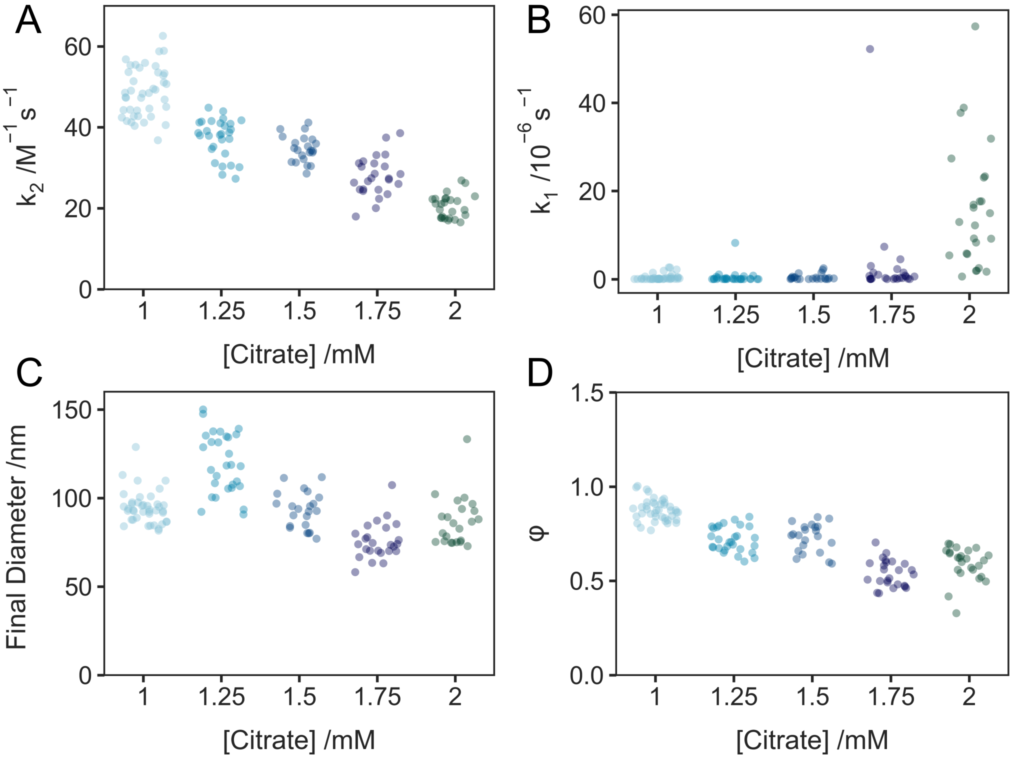

Figure 4.9: **AuNP preparation via citrate reduction: Citrate dependence.** $HAuCl_4$ concentration was fixed at 0.4 mM with citrate concentration varied from 1 to 2 mM. **(A)** Effect of citrate concentration on autocatalytic growth rate constant (k_2). **(B)** Effect of citrate concentration on nucleation rate constant (k_1). **(C)** Effect of citrate concentration on final diameter (D_f) of individual AuNPs. **(D)** Effect of citrate concentration on phase shift (φ) between reference and scattered field. **A** is taken from reference [13].

From Fig. 4.9A, a decrease in the modal rate constant for autocatalysis (k_2) with the increase of reductant concentration can be noted. The decrease in modal rate constant is perhaps at first glance unexpected: Increased reducing agent concentration commonly contributes to faster kinetics. However, this result is consistent with citrate's important role as a pH mediator in this reaction [165]; as a weak base, the increased citrate concentration leads to raised pH of the reaction solution. Under a high pH environment, the reactivity of Au (III) complexes would decrease, accompanied by a reduced formation rate of AuNPs [165, 166].

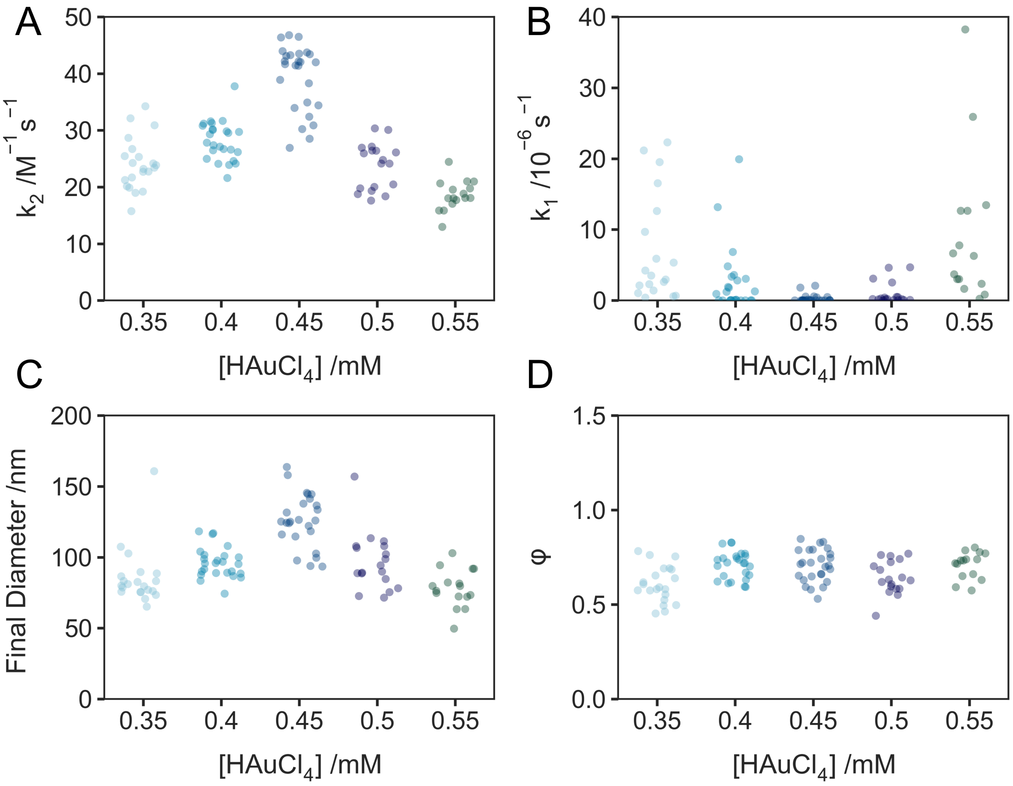

Figure 4.10: **AuNP preparation via citrate reduction: $HAuCl_4$ dependence.** Citrate concentration was fixed at 1.5 mM with $HAuCl_4$ concentration varied from 0.35 to 0.55 mM. **(A)** Effect of $HAuCl_4$ concentration on autocatalytic growth rate constant (k_2). **(B)** Effect of $HAuCl_4$ concentration on nucleation rate constant (k_1). **(C)** Effect of $HAuCl_4$ concentration on final diameter (D_f) of individual AuNPs. **(D)** Effect of $HAuCl_4$ concentration on phase shift (φ) between reference and scattered field. **A** is taken from reference [13].

Then the impact of gold precursor was investigated. When changing the $HAuCl_4$ concentration, the autocatalysis rate constant exhibits a complex behavior. As shown in Fig. 4.10A, 0.45 mM is a turning point before which the autocatalytic growth rate increases with the $HAuCl_4$ concentration. However, as the concentration of $HAuCl_4$ continues to rise, the concentration of citrate becomes the dominant factor in constraining the growth rate. As a result, k_2 finally decreases with the increase of precursor concentration.

Photocontrolled NP formation

While the reductive formation of AuNPs by citrate serves as a successful benchmark for testing our experiment, its kinetics are complicated by the dual role of citrate as both a reductant and a capping agent in the reaction. Achieving ensemble control of NP growth through changing the reductant concentration also necessitates precise timing and strict control of solution concentration. To achieve tight control over the NP formation at the individual NP level, the photocontrolled method initiated by SP was then introduced in this study.

To achieve photoinitiated NP formation, citrate was replaced with SP but with a lower concentration (0.35 mM SP *cf.* 1-2 mM citrate). The 365 nm LED irradiation was delivered by placing a liquid light guide 10 mm above the reaction chamber as shown in Fig. 4.3A. Similarly, the effect of reduction conditions and $HAuCl_4$ concentration were examined. Firstly, LED intensity was varied from 0.78 to 2.34 mW cm^{-2}, with both SP and $HAuCl_4$ concentration fixed. As expected (and in contrast to the case for citrate), Fig. 4.11A shows a growth rate dependence on LED intensity. Upon LED irradiation, the carbon–carbon bond in the pyruvate moiety undergoes homolytic cleavage, producing radicals to reduce Au^{3+} to its lower state. Higher LED intensity means faster reductant generation thus faster gold irons reduction. As a result, the increased LED intensity leads to faster AuNP formation. The distributions for other fitting parameters (k_1, D_f and φ) are also provided below (Fig. 4.11 B to D).

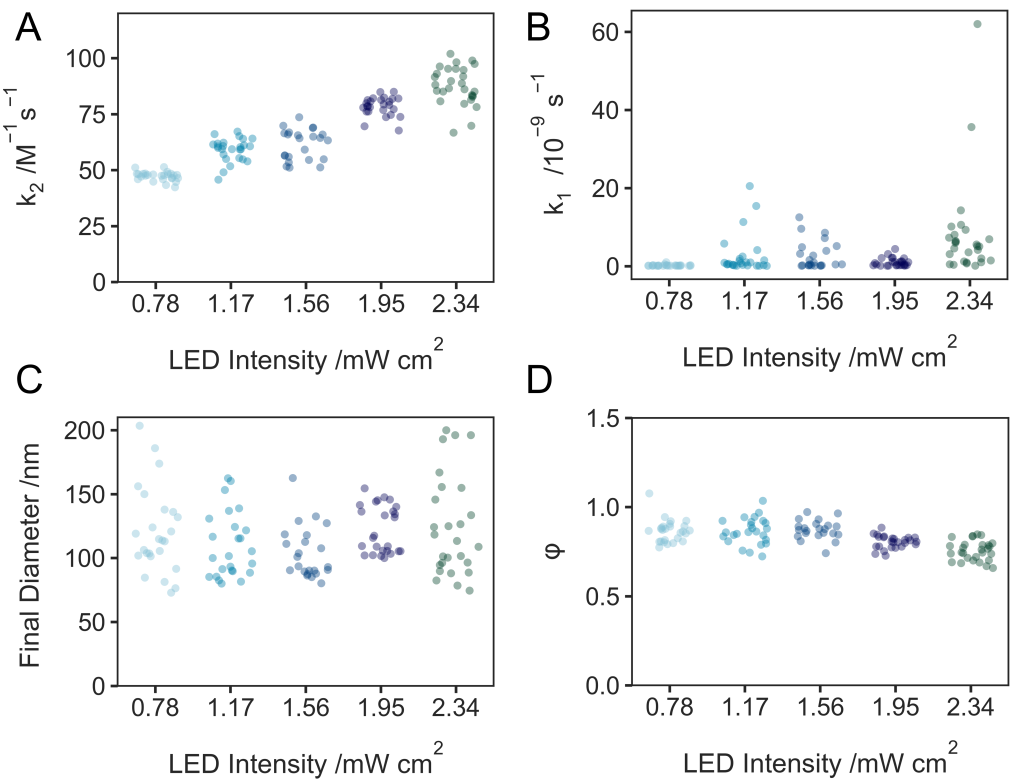

Figure 4.11: **SP photocontrol of AuNP formation: LED intensity dependence.** $HAuCl_4$ and SP concentration were fixed at 0.6 and 0.35 mM, separately. LED intensity was varied from 0.78 to 2.34 mW cm^{-2}. **(A)** Effect of LED intensity on autocatalytic growth rate constant (k_2). **(B)** Effect of LED intensity on nucleation rate constant (k_1). **(C)** Effect of LED intensity on final diameter (D_f). **(D)** Effect of LED intensity on phase shift (φ) between reference and scattered field. **A** is taken from reference [13].

Then the concentration of SP and LED intensity were fixed, and the impact of $HAuCl_4$ was explored. As shown in Fig. 4.12A, a similar trend in $HAuCl_4$ concentration dependence of k_2 as with citrate can be found (Fig. 4.10A). In this case, 0.5 mM becomes the truing point, before which an increase in k_2 can be observed followed by a decrease at higher $HAuCl_4$ concentrations. We hypothesize that the decrease in growth rate with increasing $HAuCl_4$ concentrations is due to the following mechanism: When the concentration of $HAuCl_4$ is relatively low, and the reducing agent concentration is fixed, fewer NPs are formed. Consequently, the concentration of reducing agent assigned to each NP at a certain time point is higher. However, as the concentration of $HAuCl_4$ increases, the concentration of reducing agent per NP decreases proportionally. This reduction in reducing agent concentration per NP at the same time period leads to a slower growth rate. However, as shown in Fig. 4.10C, higher gold precursor concentrations led to a larger final particle size. We assume that this is because, with a fixed LED intensity, the amount of reducing agent that can be generated within a certain time period remains constant, resulting in slower particle growth with higher $HAuCl_4$ concentration. However, given sufficient reaction time, enough reducing agent would be produced, eventually leading to a larger final particle size with higher $HAuCl_4$ concentration. The distributions for other fitting parameters are again provided below (Fig. 4.12 B to D).

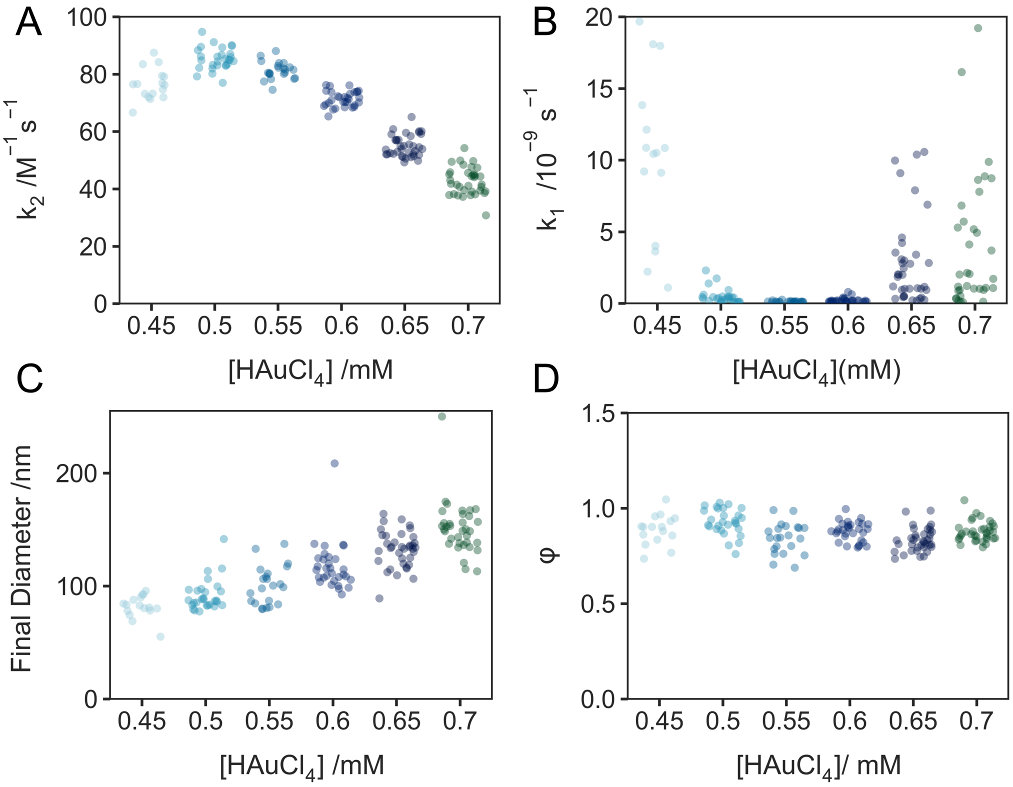

Figure 4.12: **SP photocontrol of AuNP formation: $HAuCl_4$ dependence.**
SP concentration was fixed at 0.35 mM with LED intensity maintained at 1.17 mW cm^{-2}, $HAuCl_4$ concentration was varied from 0.45 to 0.7 mM. **(A)** Effect of $HAuCl_4$ concentration on autocatalytic growth rate constant (k_2). **(B)** Effect of $HAuCl_4$ concentration on nucleation rate constant (k_1). **(C)** Effect of $HAuCl_4$ concentration on final diameter (D_f). **(D)** Effect of $HAuCl_4$ concentration on phase shift (φ) between reference and scattered field. **A** is taken from reference [13].

4.4.3 Spatio-temporal photocontrol of single NP growth

The use of SP also provides spatio-temporal control of AuNP formation. To exemplify this, the 365 nm LED illumination was replaced with 405 nm laser epi-illumination spatially-patterned using a SLM as shown in Fig. 4.3B.

Firstly, AuNP synthesis using SP was conducted under alternating 405 nm laser irradiation.

As shown in Fig. 4.13, the overall evolution of particle contrast was as expected: The contrast of the particle first becomes more negative before turning towards positive, which has already been observed in Fig. 4.7A. The growth of NPs can be controlled by switching on/off the illumination. As shown in Fig. 4.13B, the contrast of the monitored particle continues changing when the laser is on but stays relatively stable when the 405 nm illumination is switched off. This indicates that when the 405 nm laser was turned on, AuNP growth occurred continuously, but growth stopped relatively quick in the absence of 405 nm illumination.

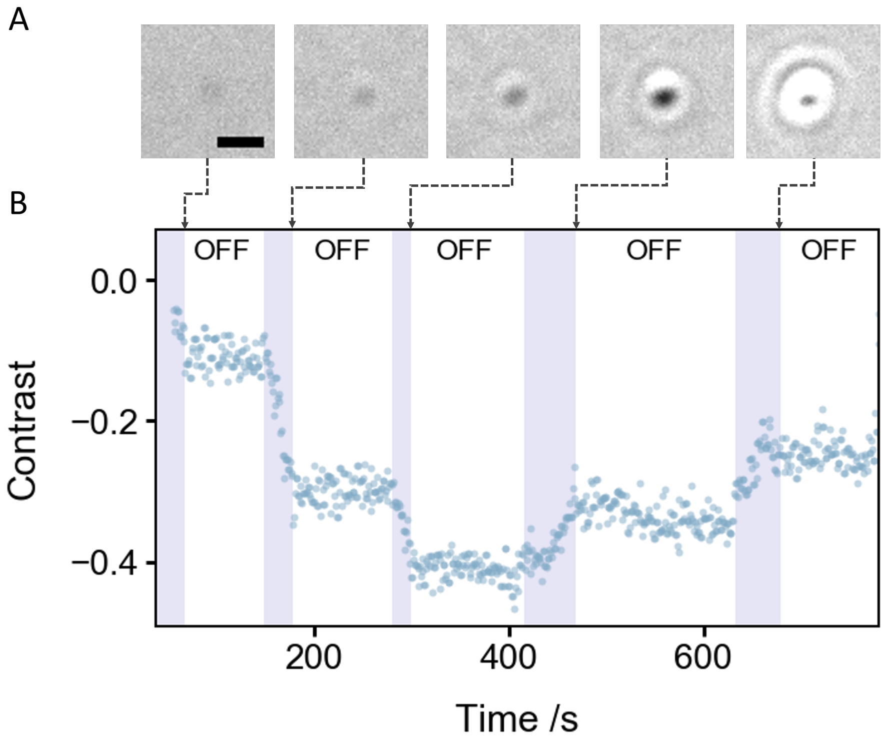

Figure 4.13: **Temporal photocontrol of AuNP growth.**
(A) Montage of images during a single AuNP growth with alternating 405 nm illumination (scale bar 500 nm). **(B)** Contrast evolution under the alternating irradiation. Exposure is indicated in purple. Figure is taken from reference [13].

Alongside temporal control, spatial control can also be achieved by applying a checkerboard pattern to the incident light path. Fig. 4.14 shows the result of displaying an 8 × 8 µm checkerboard pattern of 405 nm illumination on the coverslip surface. It can be noted that AuNPs growth was mainly concentrated at the 405 nm laser-exposed area. As a result, photocontrolled NP preparation allows us to control when and where the growth can occur.

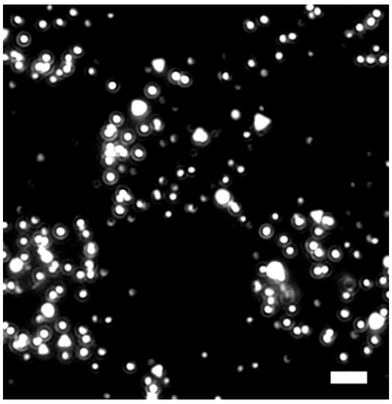

Figure 4.14: **Spatial photocontrol of AuNP growth.**
A checkerboard mask was applied to the 405 nm illumination, using a SLM (scale bar 2 µm). Figure is taken from reference [13].

4.4.4 The effect of capping agents

Capping agents play an essential role in NP synthesis by inhibiting the overgrowth of NPs and preventing aggregation and coagulation during formation [167]. Polyethylene glycol (PEG) is one of the most commonly used templating agents in AuNP preparation which improves the stability and biocompatibility of NPs [168]. By successfully employing SP as the reducing agent, we were able to separate the roles of the reductant and capping agent. As an illustrative example, we chose PEG with a molecular weight of 10 kDa (PEG10k) to investigate the impact of capping agent concentration on the photoinitiated AuNP formation. PEG10k with varied concentrations was added together with other reaction components before LED irradiation.

As illustrated in Fig. 4.15A, the increase of PEG10k concentration led to a continuous decrease in the autocatalytic growth rate constant (k_2), accompanied by an increase in the standard deviation. This effect may be attributed to the steric effects of the capping agent. By attaching to the surface of AuNPs, it prevents excessive growth and limits the availability of gold ions for NP growth. Furthermore, as depicted in Fig. 4.15B, the increased PEG10k concentration led to the expected reduction in the final NP diameter. This further validates our method in studying NP formation. The distributions for other fitting parameters are again provided following sections (Fig. 4.15C and D).

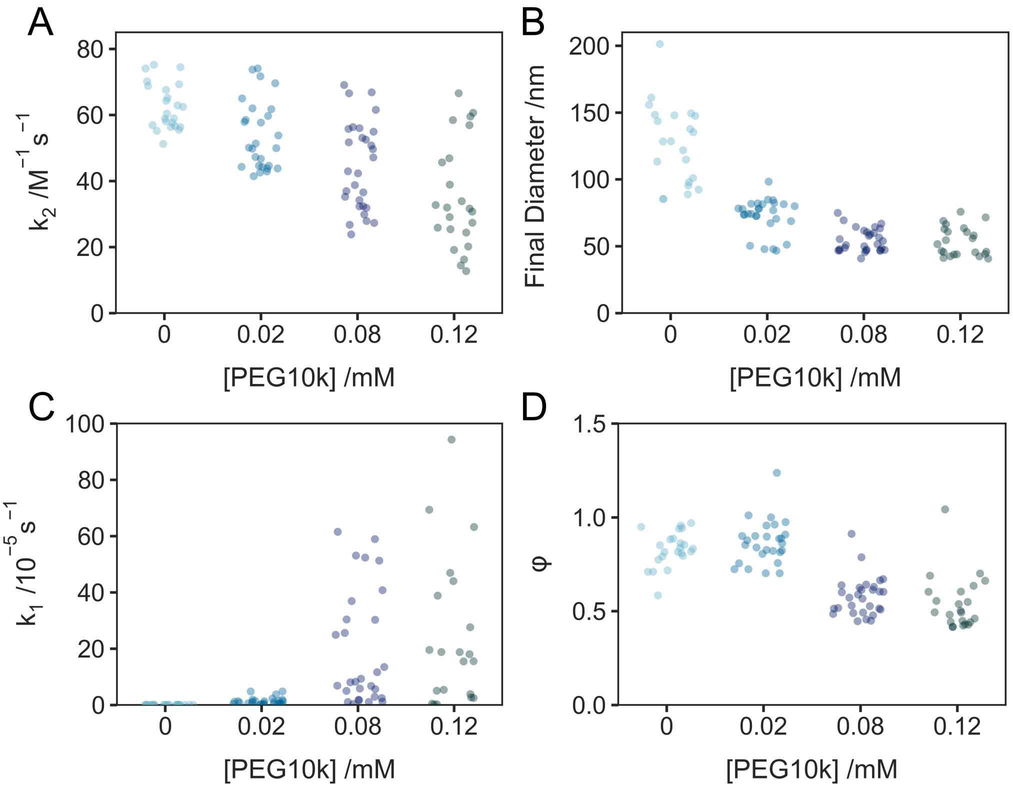

Figure 4.15: **The impact of adding PEG10k as a capping agent.**
SP and $HAuCl_4$ concentration were fixed at 0.35 and 0.6 mM, respectably, with LED intensity maintained at 1.95 mW cm^{-2}. PEG10 k concentration was varied from 0 to 0.12 mM. **(A)** Effect of PEG10k concentration on autocatalytic growth rate constant (k_2). **(B)** Effect of PEG10k concentration on the final particle diameter (D_f) of individual AuNPs. **(C)** Effect of PEG10k concentration on nucleation rate constant (k_1). **(D)** Effect of PEG10k concentration on phase shift between reference and scattered field (φ).

4.5 Summary and future work

Gold nanoparticle here is a representative model to test our method. Based on the imaging mechanism of iSCAT, it is also applicable to characterize other NPs and probe into their kinetics. Our results demonstrate that the combination of label-free iSCAT microscopy and spatio-temporal photoreductant control provides a straightforward way to study individual NP kinetics in real-time, irrespective of the optical properties of NP. The values of k_2 extracted in this study are consistent with those previously reported in other measurements of photochemically initiated AuNP growth [169, 170]. Overall, our method is validated by testing the FW-model and retrieving the particle-by-particle distribution of kinetic parameters. Taking into account the differences between our experimental conditions and those previously published, these parameters are broadly comparable [153, 169, 171].

The ability to design and synthesize new and more complex NPs is critical for advancing the field of nanotechnology and realizing the full potential of NPs for drug delivery, plasmonics, and smart materials. These experiments suggest a route for the quantitative monitoring and control required for future routes to precision engineering of individual NP properties. Tools such as these help better understand the properties of individual NPs, informing the design of more effective and targeted NPs for specific applications.

Chapter 5

Real-time monitoring of living crystallization-driven self-assembly

The research work presented in this chapter was a collaborative effort with PhD student Tianlai Xia, who is a member of Professor Rachel O'Reilly's group at the University of Birmingham. Tianlai Xia synthesized polymeric materials for the reaction, carried out the sample preparation and data analysis for kinetic studies, and characterized samples with AFM, TEM and CLSM. I conducted the *in situ* iSCAT observation of platelets growth experiments, kinetic sample characterization, data analysis, fitting and visualization. This chapter now has been drafted for a research article.

5.1 Introduction

5.1.1 Living crystallization-driven self-assembly (CDSA)

The preparation of monodisperse nanomaterials with precise morphological control based on soft matter is of great importance in current research [172, 173]. Block copolymers (BCPs), composed of a crystallizable core-forming block and a corona-forming block, have emerged as promising building blocks, paving the way for well-defined architectures with low interfacial curvature. When a poor solvent (e.g., ethanol) for the crystalline block is introduced, the core-forming block will undergo crystallization and dominates the micelle morphology, while the corona-forming block provides colloidal stabilization. Based on previous studies, a hypothetical organization of unimers within the platelets of our system can be speculated, as depicted in Figure 5.1A [174, 175]. This process is generally referred as crystallization-driven self-assembly (CDSA) [176–180]. In the early 2000s, a significant improvement was made to CDSA, which allows precise dimensional control to be applied during the assembly [181, 182]. As illustrated by Fig.5.1B, small and uniform crystallite micelles, which serve as seeds, can be generated through prolonged sonication of polydispersed cylinders synthesized via CDSA of BCPs. The fracture of the cylinder micelles follows a Gaussian scission model, where the micelle fragmentation rate decreases exponentially with the cylinder length [183]. As the core termini of individual seeds remains active, growth can be resumed from the active sites on the edge of uniform seeds. This offers a similar 'starting point' for growth upon further unimer addition. Therefore, by introducing uniform seeds as initiators into the reaction, size control can be effectively achieved during assembly. Due to the livingness of this system, this method was then termed as living CDSA, which allows myriads of nanostructures ranging from non-spherical particles to complex hierarchical architectures to be generated with unprecedented dimensional control [179, 182, 184–187]. As a result, functional materials generated through living CDSA are widely used in various fields such as drug delivery [184, 188–190], colloid stabilization [191, 192], catalysis [193–195], optoelectronics [196, 197] as well as information storage [198, 199].

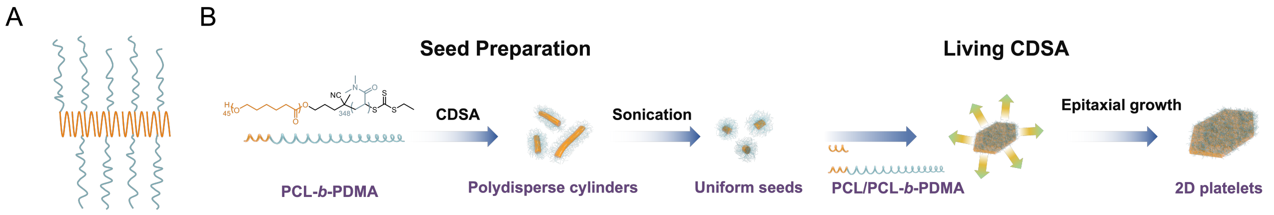

Figure 5.1: **Schematic illustration of living CDSA.**
(A) Schematic illustration of unimer organization within platelets. **(B)** Polydispersed 1D cylindrical micelles were prepared via CDSA. Then sonication was applied to these cylindrical micelles to generate seeds (small cylindrical micelles) with uniform size. Platelets with controlled size and dispersity can be prepared via living CDSA by adding unimer which contains homopolymer (HP, poly(ε-caprolactone), PCL_{45}) and block copolymer (BCP, poly(ε-caprolactone)-*b*-poly(*N,N*-dimethylacrylamide), PCL_{45}-*b*-PDMA_{348}) blends into the seed solution. *Figure prepared by Tianlai Xia.*

5.1.2 Techniques for characterizing CDSA kinetics

An in-depth understanding of CDSA growth kinetics offers considerable scope for the design and control of nanostructures with optimal properties. The majority of kinetic studies have focused on 1D fiber-like micelles formation which generally exhibits slow kinetics and takes several hours to days for complete formation [200–202]. Transmission electron microscopy (TEM) is one of the most commonly used techniques to report the size evolution of individual CDSA assemblies due to its exceptional resolution and widespread applicability [178, 201, 203–205]. However, as a static imaging technique, TEM loses its advantage in the context of studying reactions with fast kinetics. Similarly, AFM is also limited by acquisition speed. In addition, when the solution-phase AFM was employed to study the mechanism of interfacial seeded-growth of 1D micellar nanoparticles, tip-induced nanofiber fragmentation was observed, which means the reaction kinetic was complicated by the presence of new active interfaces [202].

The living CDSA process can be efficiently accelerated by modifying core crystalline chemistry. One study successfully showcased the 1D nanofiber can complete the assembly within 20 min by using BCPs with poly(cyclopentenylene-vinylene) (PCPV) core-forming block. In this study, confocal laser scanning microscopy (CLSM) has been used to visualize 1D nanofiber growth at 100 ms temporal resolution with 120 nm lateral spatial resolution [203]. Recently developed super-resolution microscopy techniques have sufficiently improved the spatial resolution. Single-molecule localization microscopy has been successfully used to characterize 1D nanofibers with 76 nm precision at 15 ms temporal resolution [206]. However, it is important to note that in addition to the previously discussed limitations of fluorescent labeling, such as photobleaching, photoblinking, and saturation, the incorporation of dye-labeled BCPs has an evident impact on the reaction kinetics [201].

5.1.3 iSCAT for CDSA research

To address the need for an *in situ* non-invasive label-free method of characterizing CDSA kinetics with high spatio-temporal resolution, here we apply iSCAT microscopy to track CDSA nanoplatelet assembly. As introduced in the former chapters, iSCAT exploits the interference between light scattered from an object of interest and a reference light generated from reflection at the interface between a glass coverslip and the sample solution to achieve a detection sensitivity capable of resolving particles tens of kDa in mass and larger [43–45]. It is an intrinsically label-free technique that can deliver high imaging speed (up to 1 MHz) [53], exploit optical super-resolution [18], and observe process over long observation times without photobleaching. iSCAT has been rapidly adopted for observing dynamic processes across a wide range of systems [13, 69, 207, 208]. Notably, iSCAT has been successfully used to monitor amyloidogenic protein aggregation and actin polymerization processes [50]. These biological fiber formation processes share many similarities with 1D fiber-like CDSA. Therefore, we reasoned that iSCAT is a promising method for monitoring the formation of CDSA nanoparticles.

In this chapter, the kinetics of 2D assemblies based on poly(ε-caprolactone) (PCL) were investigated. PCL has become a widely used polymeric material in biomedical fields due to its inherent biocompatibility and biodegradability [188, 209]. As the crystallinity of the core-forming block plays an essential role in determining the morphology of assemblies as well as kinetics, PCL_{45} was selected in this study. This is because high crystallinity (a high degree of polymerization) often leads to a rapid crystallization rate, which is commonly accompanied by self-nucleation and agglomeration. On the other hand, low crystallinity results in a slower crystallization rate, leading to irregular assembly shapes and an extended assembly process [210, 211]. As a result, to prepare 2D platelets, BCP (poly(ε-caprolactone)-*b*-Poly(N,N-dimethylacrylamide), PCL_{45}-*b*-$PDMA_{348}$) and homopolymer (HP, PCL_{45}) blends was used as unimer (Fig. 5.1). The inclusion of the HP facilitates a morphological transition from 1D to 2D [212].

Here, we exploit iSCAT to monitor the formation of 2D PCL-based platelets in real-time without the use of extrinsic labels. The impact of reaction parameters, such as unimer concentration, on platelet growth rate, size, and morphology was investigated. Furthermore, the contrast reported by iSCAT provides information about the unimer composition variations between each layer inside a multi-layered platelet. The distribution and growth kinetics of BCP and HP within a single platelet were also examined. To avoid confusion, it is important to clarify that when referring to ‘layers’ in this context, it denotes a radial arrangement, wherein each successive layer envelops the preceding one.

5.2 Materials and methods

5.2.1 Materials

Unless otherwise stated, all chemicals and solvents were used as received without further purification. Sodium ethanethiolate (90%) and borane tetrahydrofuran complex solution (1.0 M in THF) were purchased from Alfa Aesar. Carbon disulfide ($\geq$ 99%), solid iodine ($\geq$ 99%) and 4,4'-azobis(4-cyanovaleric acid) (ACVA, 98%) were purchased from Merck.

The synthesis of dual head chain transfer agent (CTA) of 2-cyano-5-hydroxypentan-2-yl ethyl carbonotrithioate (CPCLET) followed the method introduced by previous reports [188]. CTA and diphenylphosphate (DPP, 99%, Merck) were dried over P_2O_5 in a desiccator under static vacuum for 1 week before use. ε-caprolactone (99%, ACROS Organics) was vacuum distilled twice over CaH_2 before being introduced in the glovebox and used. 2,2'-azobis(2-methylpropionitrile) (AIBN, 98%, Merck) was recrystallized twice from methanol and stored at 4 °C in the dark. 1,4-dioxane (anhydrous, 99.8%) was purchased from Merck and used as received. *N,N*-dimethyl acrylamide (DMA, 99%, contains 500 ppm monomethyl ether hydroquinone as inhibitor) was purchased from Merck and was passed through a basic alumina plug to remove inhibitor before use. Dry solvents were used directly from a drying and degassing inert solvent tower system. Aminochloromaleimide (ACM) fluorescent dye was synthesized via the method reported previously [213].

5.2.2 Polymer synthesis and characterization

The following polymer materials were synthesized and characterized by Tianlai Xia.

Synthesis of PCL_{45}

In a nitrogen-filled glove box (oxygen and water content lower than 0.1 ppm), solutions of diphenylphosphate (DPP, 17.0 mg, 1 eq) in dry toluene (2.5 mL) and dual-head CTA (17.0 mg, 1 eq) in dry toluene (1 mL) were added to ε-caprolactone dry toluene solution (543.3 mg, 70 eq in 1.5 mL). After stirring for 6 h at room temperature, the solution was removed from the glove box, precipitated three times into cold diethyl ether dropwise, and collected by centrifugation. ^{1}H NMR (400 MHz, $CDCl_3$): δ (ppm): 4.10 (t, 2H, $C\boldsymbol{H}_2OCO$), 4.04 (t, 90H, $CH_2C\boldsymbol{H}_2O$), 3.62 (m, 2H, $C(CN)C\boldsymbol{H}_2CH_2$), 3.32 (q, 2H, $SC\boldsymbol{H}_2CH_3$), 2.28 (90H, $OCOC\boldsymbol{H}_2CH_2$), 1.86 (s, 3H, $C(CN)(C\boldsymbol{H}_3)CH_2$), 1.72-1.54 (180H, $OCOCH_2C\boldsymbol{H}_2CH_2C\boldsymbol{H}_2$), 1.45-1.28 (90H, $OCOCH_2CH_2C\boldsymbol{H}_2CH_2$). SEC (Chloroform, PMMA standard): M_n = 12.9 kg mol^{-1}, dispersity = 1.05.

To synthesize ACM-labeled PCL_{45}, ACM was coupled to the PCL_{45} polymer backbone by esterification. In a typical coupling reaction, PCL_{45} (100.0 mg, 1 eq), ACM (16.1 mg, 3 eq), 4-dimethylaminopyridine (DMAP) (2.3 mg, 1 eq) and *N,N'*-dicyclohexylcarbodiimide (DCC) (38.3 mg, 10 eq) were mixed together in an ampule with 2 mL $CHCl_3$. The solution was left stirring at room temperature for 2 days. The solution was then filtered with the filtrate precipitated in diethyl ether three times and the resultant polymer was dried under vacuum.

Synthesis of PCL_{45}-*b*-$PDMA_{348}$

PCL_{45} (100.0 mg, 1 eq), DMA (736.3 mg, 400 eq) and AIBN (0.3 mg, 0.1 eq) were dissolved in 1,4-dioxane (1 mL) and placed in an ampule. The solution was then freeze-pump-thawed three times and heated for 2 h at 70 °C. The reaction was quenched by immersion of the ampule in liquid nitrogen and the polymer was precipitated in ice-cold diethyl ether three times before being dried under vacuum and analyzed. SEC (chloroform, PMMA standard): M_n = 46.3 kg mol^{-1}, dispersity = 1.24.

To synthesize ACM-labeled PCL_{45}-*b*-$PDMA_{348}$, ACM was coupled to the PCL_{45}-*b*-$PDMA_{348}$ polymer backbone by esterification. In a typical coupling reaction, PCL_{45}-*b*-$PDMA_{348}$ (200 mg, 1 eq), ACM (4.3 mg, 3 eq), DMAP (0.6 mg, 1 eq) and DCC (10.3 mg, 10 eq) were mixed in an ampule with 2 mL $CHCl_3$. The solution was left stirring at room temperature for 2 days. The solution was then filtered, and the filtrate precipitated in diethyl ether three times and the resultant polymer was dried under vacuum.

NMR spectroscopy characterization

All ^{1}H NMR spectra were recorded on a Bruker 400 MHz (DPX-400) spectrometer. Chemical shift (δ) is reported in parts per million (ppm) relative to internal standard tetramethylsilane at

$\delta = 0$. Samples were prepared in deuterated chloroform ($CDCl_3$) and referenced to the residual non-deuterated signal of solvent ($CDCl_3$ at 7.26 ppm ^{1}H-NMR). The resonance multiplicities are described as s (singlet), d (doublet), t (triplet), q (quartet) or m (multiplet).

SEC characterization

SEC analysis was performed on an Agilent 1260 Infinity II system fitted with RI and ultraviolet (UV) detectors ($\lambda = 309$ and 360 nm), equipped with a PLGel 3 µm (50 × 7.5 mm guard column and two PLGel 5 µm (300 × 7.5 mm) mixed-D columns, mobile phase (eluent) using $CHCl_3$ with 0.5% triethylamine (TEA). Molecular weight (M_w) and molecular weight distributions were calibrated against poly(methyl methacrylate) (PMMA) standards and analyzed using Agilent SEC software.

5.2.3 Platelet preparation by living CDSA

Tianlai Xia synthesized the unimer and seeds used for platelet preparation and prepared the platelet samples for kinetic study. The platelet samples were then characterized via iSCAT by me.

Preparation of $\mathbf{PCL_{45}}$-*b*-$\mathbf{PDMA_{348}}$ seed solutions

20 mg BCP (PCL_{45}-*b*-$PDMA_{348}$) was dissolved into 4 mL ethanol to form 5 mg mL^{-1} BCPs solution. The samples were heated at 70 °C without stirring on a heating block for 3 h before cooling to room temperature and then aging for 5 days to yield micron-length polydisperse cylinders. The crystalline cylinders were then sonicated using a Bandelin Sonopuls sonication probe in a dry-ice/acetone bath for 20 min. The polymer solution was exposed to 60 cycles of 20 s bath sonication with an interval of 100 s to yield a short crystalline seed stock solution. For determination of the average length of the seed, a minimum number of 100 seeds were analyzed.

Bulk formation of $\mathbf{PCL_{45}}$:$\mathbf{PCL_{45}}$-*b*-$\mathbf{PDMA_{348}}$ Platelets

10 mg mL^{-1} unimer stock solution (PCL_{45}:PCL_{45}-*b*-$PDMA_{348}$ or PCL_{45}-ACM:PCL_{45}-*b*-$PDMA_{348}$-ACM) was prepared by mixing HPs (PCL_{45} or PCL_{45}-ACM) and BCPs (PCL_{45}-*b*-$PDMA_{348}$ or

PCL_{45}-*b*-$PDMA_{348}$-ACM) at a 1:1 weight ratio in a good solvent for PCL (THF or Chloroform). A working seed solution was prepared by diluting the stock seed solution in ethanol to form the targeted concentration, then 'aged' for at least 1 h. Then a small volume of unimer stock solution was added to the seed solution in a screw cap vial followed by shaking by hand for 5 s, the final unimer concentration was varied by adjusting the volume of stock solutions added to each reaction. At predetermined time points, 140 µL sample mixture was withdrawn and added to 140 µL of MQ water to quench the reaction, followed by subsequent analysis.

5.2.4 Comparison of analysis methods

Tianlai Xia conducted the platelet characterization via TEM, AFM, and CLSM. iSCAT characterization was conducted by me.

TEM characterization

Dry state TEM imaging was performed on JEOL 1400 Bio (1720/GB06) microscopy at an acceleration voltage of 80 kV. CDSA samples were deposited onto graphene oxide-coated copper grids which were then stained with an aqueous 1wt. % uranyl acetate (UA) solution for drying and microscopic analysis. For the determination of the average size of the platelets, a minimum number of 100 platelets were analyzed.

AFM characterization

AFM samples were prepared by drop casting 10 µL of assemblies in ethanol onto a mica silicon wafer which was treated by Sigmacote, followed by drying naturally in air. Imaging and analysis were performed on a JPK Nanowizard 4 system in quantitative imaging (QI) mode. The tips for the AFM analysis (PPP-NCHAuD) were purchased from NANOSENSORSTM, with resonance frequency (kHz) in the window of 204 - 497 and force constant in the range of 10 - 130. The AFM pictures and data were analyzed and collected using the JPK data processing software with QI mode. For the determination of the average size of the platelets, a minimum number of 100 platelets were analyzed.

CLSM characterization

FV3000 (Olympus) confocal microscope with an IX-81 inverted base (Olympus) and the 20× and 60× oil lens (Olympus) were used for imaging. The FV3000 system was driven with the FV31S-SW Viewer software platform (Olympus) with scan rates of 1 µs pixel^{-1} at 515 by 512 pixels to 1024 by 1024 pixels. For platelet characterization, ca. 100 platelets were traced manually using ImageJ.

iSCAT characterization

An identical iSCAT setup employed in Chapter 2 for instrument calibration was also utilized for CDSA studies (Fig. 2.1A). The procedure for cleaning the glass coverslip, silicone spacers, and constructing the reaction chamber has been explicitly introduced in Chapter 2.

PCL_{45}:PCL_{45}-*b*-$PDMA_{348}$ platelets synthesized in bulk were repeatedly spin-coating onto the cleaned coverslip at 3200 rpm for 15 seconds until the desired surface density was achieved. Then a spacer was placed onto the platelet-coated surface before the addition of methanol: water (30:70, v: v) solution and imaging. A laser power density of 2 µW µm^{-2} at 637 nm and a camera exposure time of 900 µs were selected. A minimum number of 100 platelets was analyzed to determine the average size.

5.2.5 Real-time 2D platelet growth monitored by iSCAT

50 µL of 0.1 µg mL^{-1} seed solution was spin-coated onto the cleaned coverslip twice at 3200 rpm for 50 seconds, immediately followed by 4000 rpm for 30 seconds. A cleaned plastic spacer was then placed onto the seed-coated coverslip to form a reaction chamber. This reaction chamber has then been mounted above the objective with the objective being adjusted to focus on the surface. Unimer stock solutions were diluted in methanol to achieve the targeted concentration and added into the reaction chamber, followed by iSCAT imaging immediately. A laser power density of 2 µW µm^{-2} at 637 nm, a camera exposure time of 800 µs, and an overall time-lapsed frame rate of 1.5 s^{-1} were selected.

Multi-layered platelets (2-layered and 4-layered platelets shown in Fig. 5.10 and Fig.

5.11, respectively.) were prepared by alternately adding PCL_{45}:PCL_{45}-*b*-$PDMA_{348}$ blends and PCL_{45}. Specifically, PCL_{45}:PCL_{45}-*b*-$PDMA_{348}$ blends were first added onto a seed-coated surface (prepared in accordance with the protocol introduced above) to form the first layer of the multi-layered platelet. After a period of growth, the reaction solution was removed from the chamber, followed by the addition of PCL_{45} solution, and this alternating sequence was repeated until the desired number of layers was achieved. Recording started immediately after each unimer addition. A laser power density of 4 µW μm^{-2} at 637 nm, a camera exposure time of 400 µs, and an overall time-lapsed frame rate of 1 s^{-1} were selected. Alternatively, multi-layered platelets (3-layered platelets shown in Fig. 5.9.) were also prepared using a sequential addition method similar to that described above. PCL_{45}:PCL_{45}-*b*-$PDMA_{348}$ blends with sequentially increasing unimer concentration were added at each step. A laser power density of 4 µW μm^{-2} at 637 nm, a camera exposure time of 400 µs, and an overall time-lapsed frame rate of 1 s $^{-1}$ were selected.

5.3 Data analysis

5.3.1 *in situ* iSCAT monitoring of platelets growth

Data preprocessing for image cropping, dark counts subtraction, and laser fluctuation removal was conducted using a Python script developed in-house, which has been explicitly introduced in Chapter 2 and Chapter 4. Then the Fiji image analysis software [214] was used to extract platelets morphological and dimensional information from the prepossessed image using following steps:

1. Stacks (Fig. 5.2A) were subtracted by a background corresponding to the median-average of around 10 frames corresponding to the image area prior to platelet growth (Fig. 5.2B), which generates the background corrected result as shown in Fig. 5.2C.

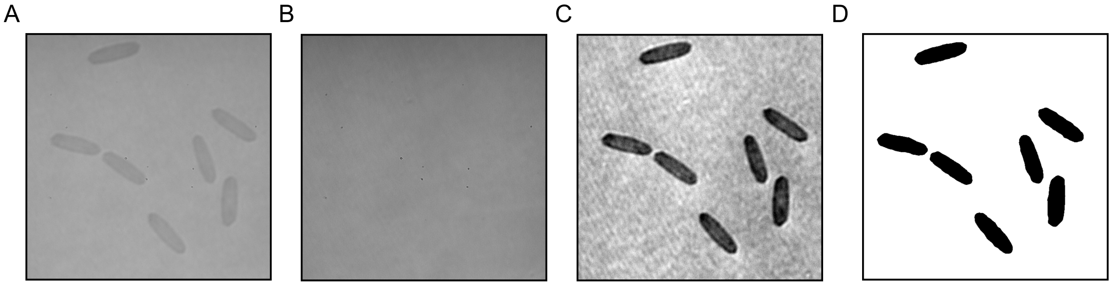

Figure 5.2: **Schematic illustration of CDSA data process.**
(A) Raw data. **(B)** Background generated from the median-average of 6 frames corresponding to the image area prior to platelet growth. **(C)** Data after background subtraction. **(D)** Data after applying a binary mask.

2. Frame averaging was conducted on some of the experiments (the details of averaging have been stated in each experiment).
3. A binary mask was created from a low-pass Gaussian filtered ($\sigma = 2$ px) replica of the image and used to isolate individual platelets as shown in Fig. 5.2D.
4. After setting the measurement scale, particle parameters, such as area, long/short axis length, and aspect ratio were then collected using the built-in 'Analyze Particle' function in Fiji.

5.3.2 Kinetic data analysis and fitting

Samples collected at predetermined time points were quenched with MQ water and spin-coated onto cleaned coverslips and sent for iSCAT characterization. A minimum number of 100 platelets were analyzed for each time point. Morphological and dimensional information was extracted using Fiji with similar protocol introduced above, only one modification was made for background subtraction. A background was selected by collecting a frame in the sample where no platelets were on the surface. Stacks were then subtracted by this background.

With the averaged area of platelets at each time point being extracted, the evolution of platelet area as the function of reaction time can be plotted. To extract kinetic information, kinetic data fitting was conducted via a Python script developed in-house. More details are provided in the following section, but in general, we fitted the size evolution data to Eq. 5.6

using Scipy.optimize [76], which produces a rate constant for each fitting. To conduct the fitting, the initial number of unimer (N_0) and the number of seeds (N_{seed}) can be calculated from initial unimer and seed concentration and fixed during the fitting. In addition, the contribution of one unimer molecule to the area of the platelets (B) is calculated from Eq. 5.5 and fixed during the fitting.

5.4 Results and discussion

5.4.1 Comparison of platelet characterization techniques

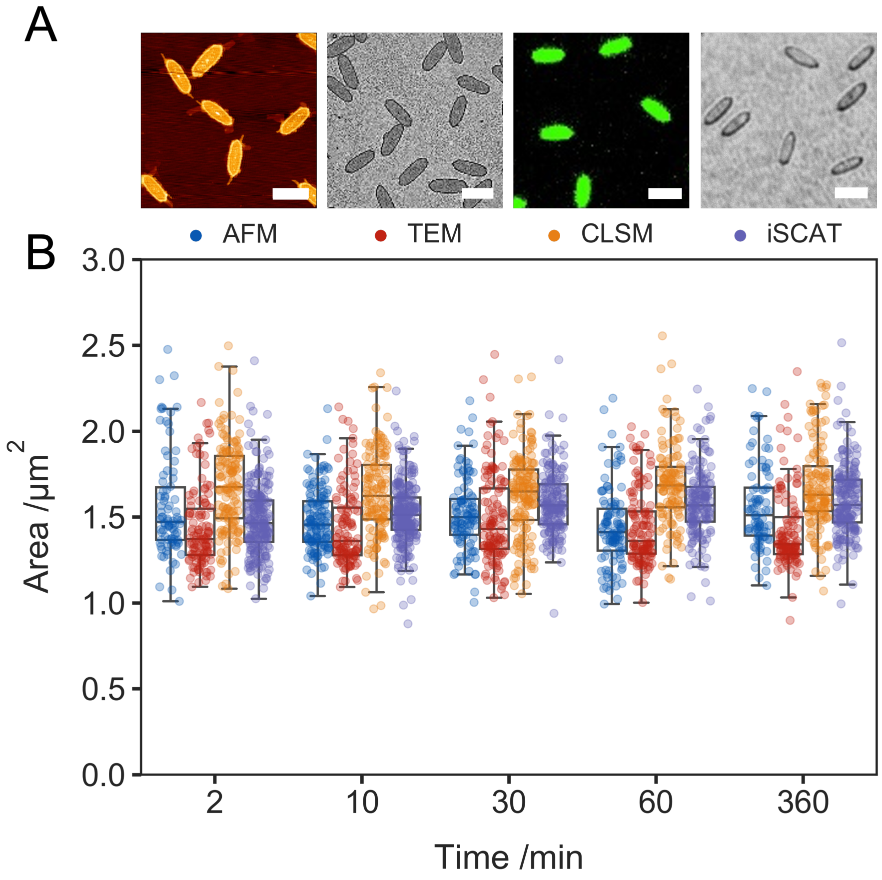

Figure 5.3: **Comparison of 2D platelet characterization methods.**
(A) PCL_{45}:PCL_{45}-*b*-$PDMA_{348}$ platelet samples collected after 6 h of growth (scale bar: 2 µm) characterized by AFM, TEM, CLSM, and iSCAT. (*AFM, TEM, and CLSM data were collected by Tianlai Xia*). **(B)** Comparison of PCL_{45}:PCL_{45}-*b*-$PDMA_{348}$ platelet area distributions over time measured with AFM, TEM, CLSM, and iSCAT.

To examine the ability of iSCAT to correctly identify and characterize CDSA assemblies, we compared platelet morphology and size information acquired from iSCAT with commonly used techniques, namely AFM, TEM, and CLSM. Assembly of platelets was initiated by adding 10 µL 10 mg mL^{-1} PCL_{45}:PCL_{45}-*b*-$PDMA_{348}$ 1:1 unimer blends into 1 mL 0.01 mg mL^{-1} seed ethanol solution followed by mixing via shaking. At predetermined time points, sample aliquots were withdrawn and quenched by water addition. Then the samples were sent for characterization by each technique (an extensive experimental protocol has been provided in the method section). From Fig. 5.3A and B, it is obvious that platelet morphology and area information extracted from AFM, TEM, CLSM, and iSCAT are consistent. Moreover, in this bulk reaction with higher unimer concentration (compared with surface growth), the platelet formation is rapid, with assembly finished within two minutes of our first time point. The rapid kinetics pose a significant challenge for TEM, AFM, and CLSM in observing the complete assembly process and capturing kinetic information due to their limited temporal resolution. As discussed before, iSCAT is known for its excellent spatio-temporal resolution. Consequently, it is sensible to apply iSCAT to real-time monitoring of the 2D platelet self-assembly process and probe into kinetic study.

5.4.2 Real-time monitoring of platelets formation

The following experiment was conducted as a proof-of-concept to demonstrate that iSCAT can be used as a powerful characterization method for monitoring the growth process of CDSA assemblies. Uniform cylindrical seeds (18-22 nm) were spin-coated onto the solvent-cleaned glass coverslip. The formation of hydrogen bonds occurred between the amide groups in the corona-forming block of the seeds and the hydroxyl groups on the glass surface, facilitating the adhesion of the seeds (and PCL_{45}:PCL_{45}-*b*-$PDMA_{348}$ platelets) to the surface. Then a plastic spacer was placed onto the coverslip to form a reaction chamber. PCL_{45}-*b*-$PDMA_{348}$ and PCL_{45} (1:1, w:w) unimer blends were dispensed in methanol, mixed well, and quickly added into the reaction chamber followed by iSCAT recording immediately. Fig. 5.4A shows a time series of iSCAT images collected during the epitaxial growth of individual platelets (the complete recording is provided in Appendix Movie S2). When exposed to methanol, the core-forming block of BCP (PCL_{45}-*b*-$PDMA_{348}$) and the HP (PCL_{45}) start to crystallize and gradually assemble

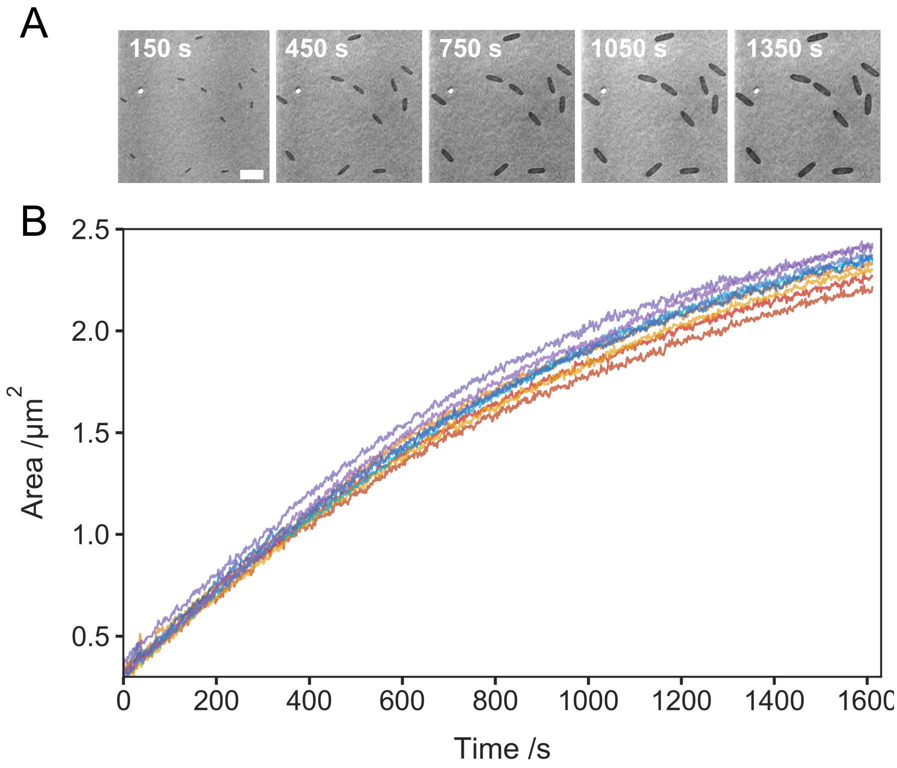

Figure 5.4: **Real-time label-free monitoring of individual platelets growth.** A 50 µL 0.1 µg mL^{-1} seed solution was spin-coated onto a cleaned coverslip (3200 rpm for 50s followed by 4000 rpm for 30s). 3.03 µg mL^{-1} PCL$_{45}$:PCL$_{45}$-*b*-PDMA$_{348}$ blends methanol solution was added onto the seeds-coated surface and iSCAT recording started with a laser power density of 2 µW µm^{-2} at 637 nm, a camera exposure time of 800 µs, and an overall time-lapsed frame rate of 1.5 s^{-1} were chosen. **(A)** Montage of iSCAT images collected during 2D platelet growth (scale bar: 3 µm). **(B)** Size evolution of 11 individual platelets.

onto the edges of seeds, resulting in a continuous increase in size and the formation of a uniform 2D structure. Following image segmentation and analysis, parameters describing the platelet morphology (e.g., area, long/short axis length, and aspect ratio) can be extracted and analyzed to yield the kinetics of individual platelet growth. As shown in Fig. 5.4B, the area evolution of 11 platelets can be tracked, exhibiting relatively uniform final platelet area (around 2.4 µm^2) and growth behavior. For reactions conducted on the surface, the unimer concentration was reduced (3.03 µg mL^{-1} in this case) to adjust the reaction kinetics to a more manageable scale in practical applications.

Kinetics can also be tracked at a much higher acquisition speed. The data shown in Fig. 5.5A and B were acquired from iSCAT recording collected immediately after unimer addition with the imaging speed of 100 Hz for 50 seconds. The fluctuations in the growth curve in Fig.

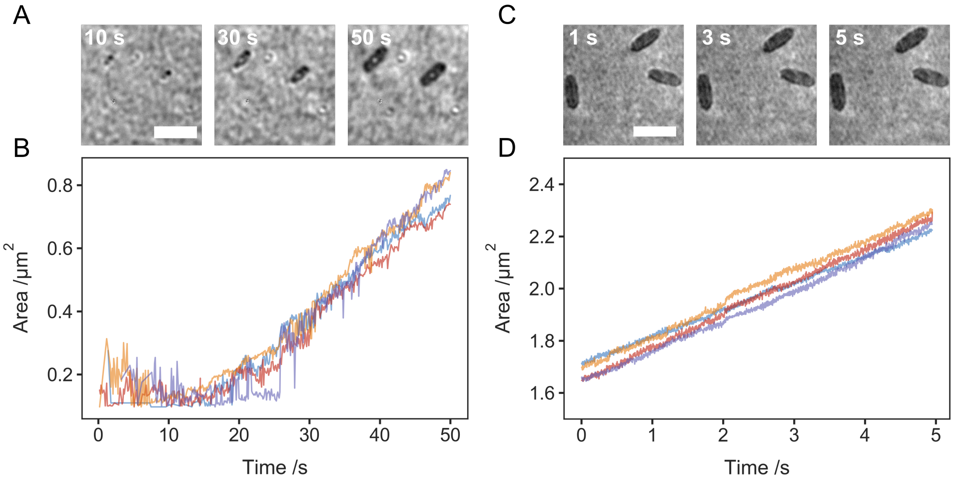

Figure 5.5: **High-Speed monitoring of platelet formation.**
(A) Montage of images collected from the initial stage of platelet growth (scale bar: 2 µm). **(B)** Size evolution of three platelets (50 µL 0.1 µg mL^{-1} seed solution was spin-coated onto the cleaned coverslip using the following protocol: 3200 rpm for 50 s, followed by 4000 rpm for 30 s. 5.56 µg mL^{-1} PCL_{45}:PCL_{45}-*b*-$PDMA_{348}$ blends in methanol was added onto the surface, followed by imaging immediately. Laser power density: 0.024 mW µm^{-2} at 637 nm; frame rate: 100 s^{-1}; exposure time 80 µs; 10 frame averaging). **(C)** Montage of images collected from the mid-stage of platelet growth (scale bar: 3 µm). **(D)** Size evolution of three platelets (50 µL 0.1 µg mL^{-1} seed solution was spin-coated onto the cleaned coverslip using the following protocol: 3200 rpm for 50 s, followed by 4000 rpm for 30 s. 2.78 µg mL^{-1}PCL_{45}:PCL_{45}-*b*-$PDMA_{348}$ blends in methanol was added onto the surface. Imaging starts from the mid-stage of platelet growth. Laser power density: 0.024 mW µm^{-2} at 637 nm; frame rate: 3000 s^{-1}; exposure time 80 µs).

5.5B are because the platelet size is relatively small at the initial stage and it is challenging to efficiently differentiate the signal from the background, which led to artifacts in the data analysis. Fig. 5.5C and D displays the data from iSCAT recording initiated after platelets had already formed on the surface, employing a 3 kHz imaging speed for 5 seconds. Despite the attainable high speed, it is important to note that, in practical applications, we diluted the unimer solution to adjust the reaction kinetics to a more manageable scale, which leads to an easier data collection. Where the reaction is exceptionally rapid, significant information may be lost during the interval between unimer addition and the commencement of recording. The incorporation of a flow system would address this issue, enabling the study of higher unimer concentrations and consequently faster reaction kinetics. We assume that under an optimal experiment setup, by fully utilizing the temporal resolution of iSCAT, we would be able to provide hidden kinetic information that inaccessible before. For example, with high imaging speed, we would be able to observe the contrast variations resulting from different unimer (e.g.,

PCL_{45} and PCL_{45}-*b*-$PDMA_{348}$) additions onto a single platelet.

5.4.3 Platelet kinetics

To quantify the kinetics of platelet growth, we examined the dependence of platelet size and morphology on unimer concentration, seed concentration, and solvent conditions. The model used in this study was established previously [215]. The overall rate equation is described by

$$\frac{dN_{\mathrm{t}}}{dt} = -k[4\pi B n_{\mathrm{a}}^2 (N_0 - N_{\mathrm{t}})]^{\frac{1}{2}} N_{\mathrm{t}}, \tag{5.1}$$

where N_{t} is the number of unimer molecules remaining in the reaction at time t, k is the overall rate constant, N_0 is the initial number of unimers, n_{a} is the number of unimers in the exposed areas per unit perimeter and B is the contribution of one unimer to the area of the platelet. The integration of Eq. 5.1 gives the following result:

$$N_{\mathrm{t}} = \frac{2N_0}{\cosh\left(2n_a\sqrt{\pi B N_0}\,(C_1 - kt)\right) + 1}, \tag{5.2}$$

by setting t to 0 and N_{t} to N_0, the integration constant (C_1) can be set to 0. To further simplify the equation, the effective rate constant (k') was then introduced and can be expressed as:

$$k' = 2n_a\sqrt{\pi B N_0} \times (-k), \tag{5.3}$$

and Eq. 5.2 can be further expressed as:

$$N_{\mathrm{t}} = \frac{2N_0}{\cosh(k't) + 1}. \tag{5.4}$$

The contribution of one unimer to the area of the platelet (B) can be calculated from:

$$B = \frac{A_{\mathrm{final}} \times N_{\mathrm{seed}}}{N_0}, \tag{5.5}$$

where A_{final} is averaged final platelet size, and N_{seed} is the number of seeds. We assume here that B is a constant and links the experimentally determined platelet area to the consumption of unimers. Consequently, the evolution of platelet size with time can therefore be established:

$$A_{\mathrm{t}} = \frac{B \cdot (N_0 - N_t)}{N_{\mathrm{seed}}} = \frac{BN_0}{N_{\mathrm{seed}}} \left(1 - \frac{2}{\cosh(k't) + 1}\right) \tag{5.6}$$

With the relation between platelet area and reaction time established, the platelet area evolution reported by iSCAT can then be fitted to Eq. 5.6 using Scipy.optimize [76], and the rate constant for each experiment can be extracted.

The effect of unimer concentration was first investigated and the results are shown in Fig. 5.6A. As expected, a higher initial unimer concentration leads to faster platelet growth and produces platelets with larger final surface areas; with a linear dependence of overall rate constant on unimer concentration (Fig. 5.6B), and an overall reaction order of 0.41. The deviation from simple first-order kinetics has been previously reported, which can be attributed to conformational effects on the BCP during assembly [201, 205]. Then the unimer concentration and solvent conditions were fixed, with the seed concentration varied from 0.01 to 0.045 µg mL^{-1}. As shown in Fig. 5.6C, the effective rate constant k' increases with seed concentration, and as the relative number of unimers assigned to each seed decreases, a higher seed concentration produces platelets with a smaller final area. Similar results were reported in a previous study [201]. Furthermore, the effect of the good solvent, tetrahydrofuran (THF), of the crystallizable core-forming block (PCL) was investigated. Fig. 5.6D illustrates the overall inhibitory effect of THF addition. We assume this is because the increase of good solvent content improves the solubility of PCL_{45} in the system, which in turn hinders its crystallizability. Thus, in an environment with elevated THF content, both BCP and HP will crystallize more slowly, thereby decelerating the assembly rate. Overall, we observe that the final size of platelets generated from fixed unimer and seed concentrations remains consistent, regardless of solvent compositions (from 0 to 3% of THF content). However, when the THF content reaches 5%, the final platelet area increases significantly. We hypothesize that as the THF content continues to increase, the seeds begin to dissolve, leading to an increase in total BCP concentration/decreased number of seeds and eventually resulting in larger final platelet sizes.

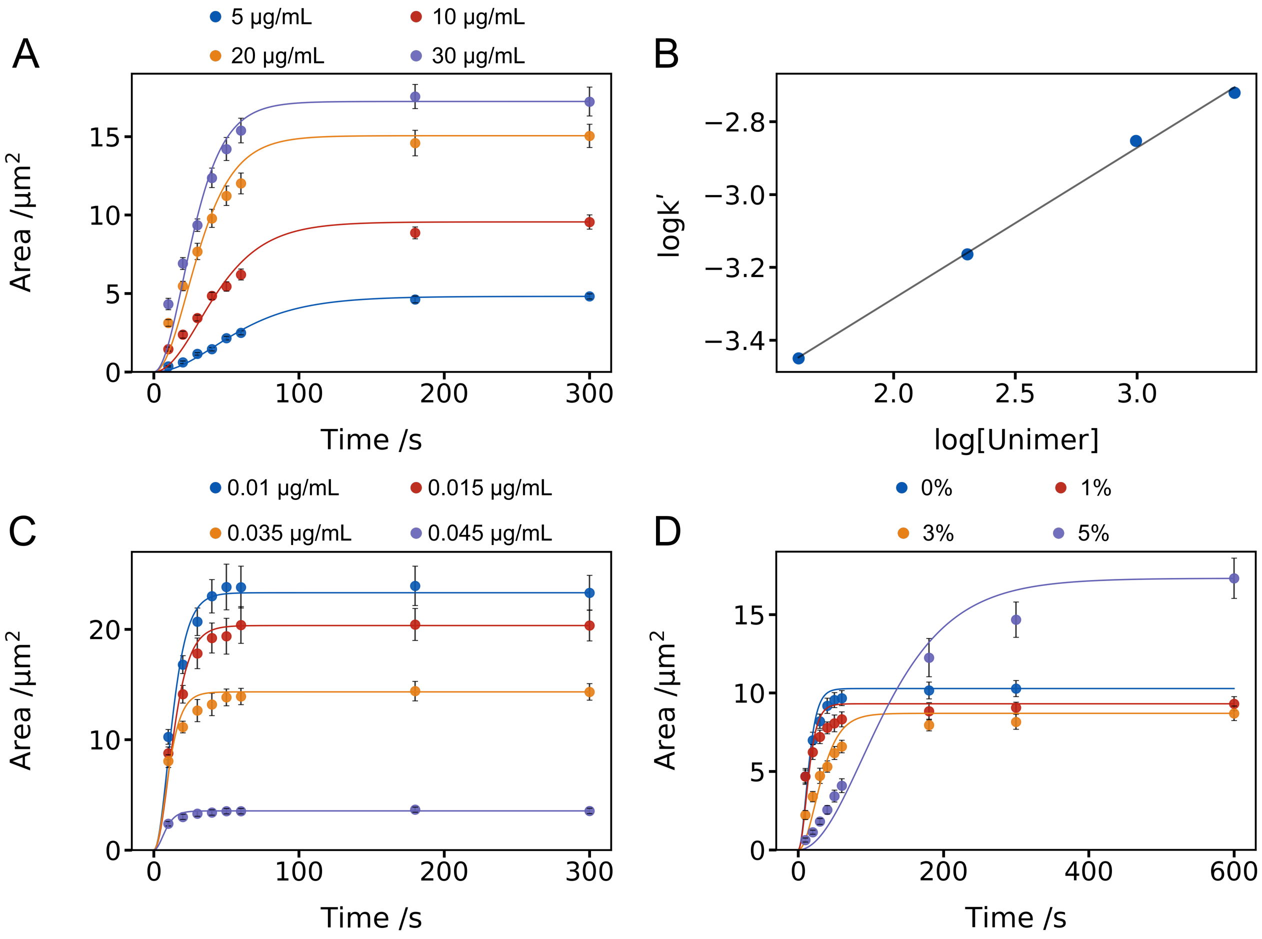

Figure 5.6: **Dependence of platelet kinetics on reaction conditions.** **(A)** Size evolution over time with concentrations of PCL_{45}:PCL_{45}-*b*-$PDMA_{348}$ (1:1, w:w) unimer varied from 5, 10, 20 to 30 µg mL^{-1}, while the seed concentration was fixed at 0.005 µg mL^{-1} (error bars represent the standard deviations of the platelet area distribution for each time point, as seen in the following kinetic plots). Rate constants extracted from the fitting for each unimer concentration (from low to high) are 0.032, 0.042, 0.058, 0.066 s^{-1}, respectively. **(B)** Plot of logk' versus log[Unimer], reaction order: 0.41. **(C)** Size evolution over time with the seed concentration varied from 0.01, 0.015, 0.035 to 0.045 µg mL^{-1}, while the unimer concentration was fixed at 60 µg mL^{-1}. Rate constants extracted from the fitting for each seed concentration (from low to high) are 0.139, 0.131, 0.17, 0.218 s^{-1}, respectively. **(D)** Size evolution as the function of time with THF content varied from 0, 1, 3 to 5%. Unimer and seed concentrations were fixed at 20 µg mL^{-1} and 0.015 µg mL^{-1}, separately. Rate constants extracted from the fitting for each THF content (from low to high) are 0.124, 0.123, 0.057, 0.015 s^{-1}, respectively.

5.4.4 Platelet morphology

In addition to the kinetics, the impact of unimer and seed concentrations as well as solvent composition on platelet morphology, such as the length of the long (L_1) and short (L_2) axes, and the aspect ratio (L_1:L_2) were also explored. Interestingly, alterations in the solvent composition of the system significantly impacted platelet morphology. As shown in Fig. 5.7A, the increase of THF content leads to the formation of elongated platelets. In Fig. 5.7B, where THF content varies from 0 to 5%, it is evident that the aspect ratio remains constant across time for a specific reaction condition. Additionally, it can also be noted that higher THF contents result in platelets with increased aspect ratios. Fig. 5.7C provides further insights, the preference for unimer addition along the long axis (L_1) becomes more pronounced with the increase of THF content.

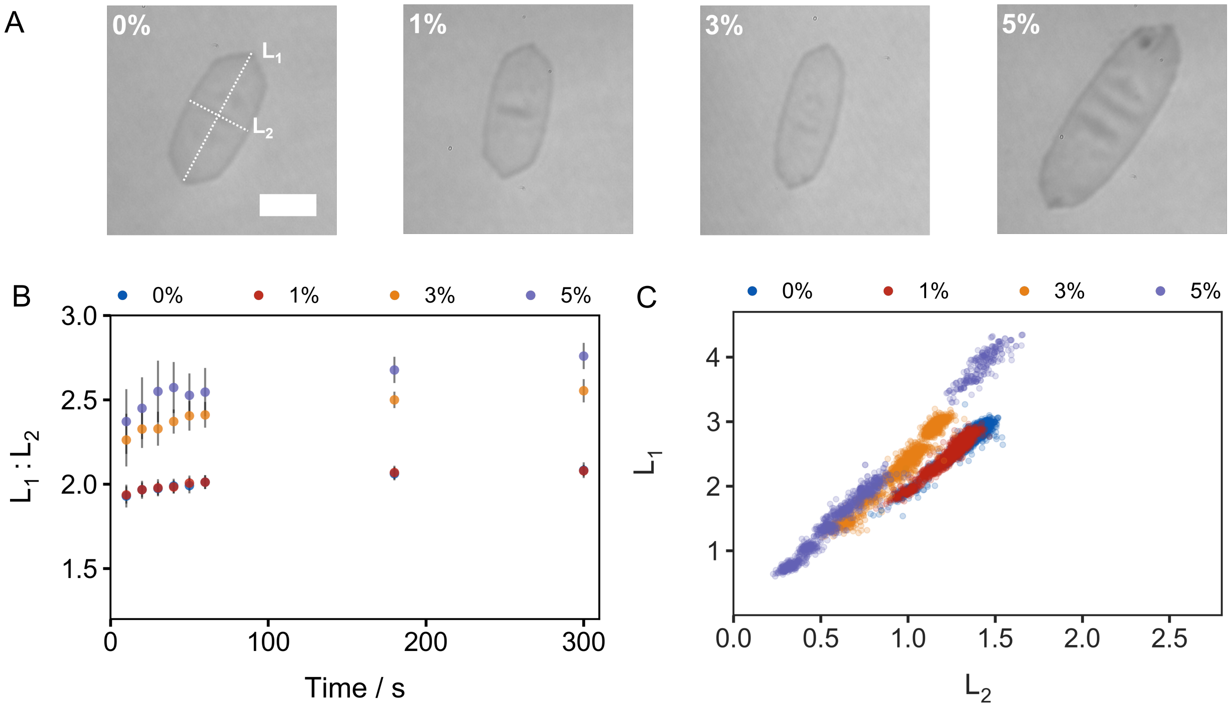

Figure 5.7: **Dependence of platelet morphology on solvent composition.** THF content varied from 0, 1, 3, to 5%, unimer and seed concentrations were fixed at 20 µg mL^{-1} and 0.015 µg mL^{-1}, separately. **(A)** Raw iSCAT images associated with the 300-second data points in **B** and **C** (scale bar: 2 µm). **(B)** Aspect ratio (L_1:L_2) evolution as the function of time with THF content varied from 0, 1, 3, to 5%. **(C)** The distribution of the length of the long (L_1) and short axis (L_2) of individual platelets with THF content varied from 0, 1, 3, to 5%.

In contrast to alterations in solvent composition, changes in unimer or seed concentration have a modest impact on platelet shape during assembly. As shown in Fig. 5.8, platelets with consistent aspect ratios (lower than those prepared under higher THF content) are generated, regardless of variations in unimer or seed concentration.

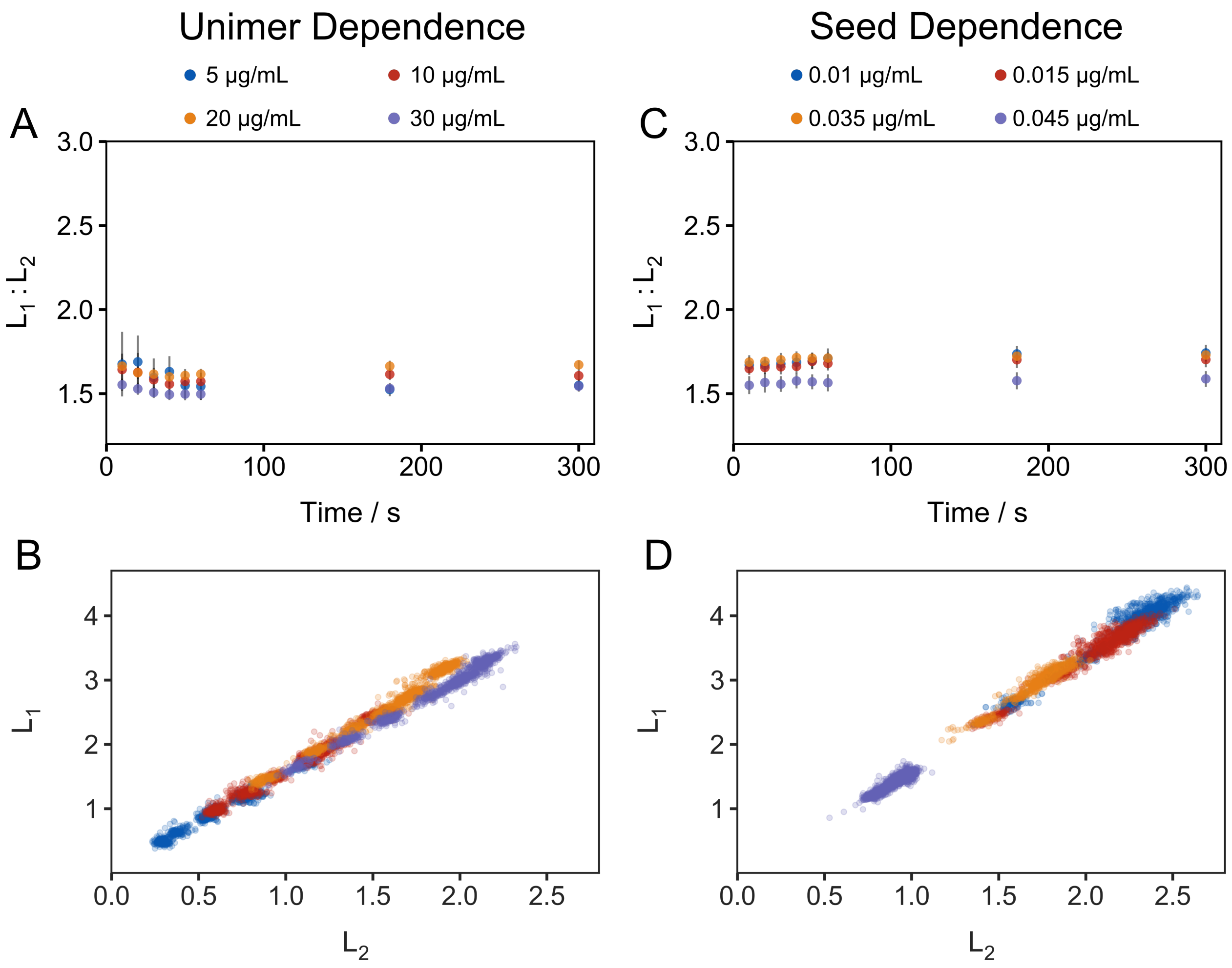

Figure 5.8: **Effects of unimer/seed concentrations on platelet morphology. Unimer dependence (column 1)**. Unimer PCL_{45}:PCL_{45}-*b*-$PDMA_{348}$ (1:1, w:w) concentration was varied from 5, 10, 20 to 30 μg mL^{-1}. Seed concentration was fixed at 0.005 μg mL^{-1}. **Seed dependence (column 2)**. Seed concentration was varied from 0.01, 0.015, 0.035 to 0.045 μg mL^{-1}. Unimer concentration was fixed at 60 μg mL^{-1}. **(A)** Aspect ratio (L_1:L_2) evolution as function of time with unimer PCL_{45}:PCL_{45}-*b*-$PDMA_{348}$ (1:1, w:w) concentration varied from 5, 10, 20 to 30 μg mL^{-1}. **(B)** The distribution of the length of the long (L_1) and short axis (L_2) of individual platelets with unimer PCL_{45}:PCL_{45}-*b*-$PDMA_{348}$ (1:1, w:w) concentration varied from 5, 10, 20 to 30 μg mL^{-1}. **(C)** Aspect ratio (L_1:L_2) evolution as the function of time with seed concentration varied from 0.01, 0.015, 0.035 to 0.045 μg mL^{-1}. **(D)** The distribution of the length of the long (L_1) and short axis (L_2) of individual platelets with seed concentration varied from 0.01, 0.015, 0.035 to 0.045 μg mL^{-1}.

5.4.5 Multi-layered platelet growth

In accordance with the concepts introduced in Chapter 1, the difference in refractive index between the platelet and its surrounding mediums gives rise to a scattering signal. This signal subsequently interacts with the reference signal stemming from interface reflections, ultimately forming the detected signal. In scenarios where the reaction medium remains the same, the reference signal can be considered as a constant. Any alterations in the composition or thickness of the platelet will lead to variations in refractive indices or optical path lengths (thus, phase shift), which finally contributes to the change of scattering signals. As a result, iSCAT is highly sensitive to the local changes in optical properties and can be used as a refractive index microscope. For instance, it has been successfully applied to study the formation of lipid bilayer [69] and nanoscopic lipid phase transition [70]. Consequently, we reasoned that it is possible to resolve BCP and HP distribution and composition variations within a single platelet using iSCAT as a label-free probe.

During living CDSA, the active core termini of platelets, allows them to function as seeds for epitaxial growth upon further unimer addition (Fig. 5.9A). Thus, 3-layered platelets can be prepared by sequential addition of PCL_{45}:PCL_{45}-*b*-$PDMA_{348}$ blends with increased unimer concentration for each layer (Movie S3 in Appendix). From the iSCAT images of platelets collected after the completion of each layer's growth (Figure 5.9A), one can observe that the boundaries between each layer are not sharply defined, albeit still identifiable. It can be noted that within each layer, the outermost boundary appeared discernably darker (larger negative contrast) compared to the center. We hypothesized that this effect is potentially caused by the nonuniform distribution of PCL_{45} and PCL_{45}-*b*-$PDMA_{348}$ because of crystallization rates difference [216, 217]. Following image segmentation and analysis, area evolution of three 3-layered platelets can be extracted and analyzed to yield the kinetics of individual multi-layered platelet growth. Fig. 5.9B illustrates that all three platelets display analogous growth behavior throughout each layer formation. We examined the growth kinetics of each layer by tracking the progression of the averaged area of these three platelets with successive additions. This data was synchronized with the corresponding time of addition, as depicted in Fig. 5.9C. The kinetic behavior for each growth step was unchanged from those determined in Fig. 5.6A: An increase in unimer concentration led to both a faster assembly rate and a greater increase in area. The rate constants extracted from this surface-growth platelet are comparable to those prepared in bulk (Fig. 5.6).

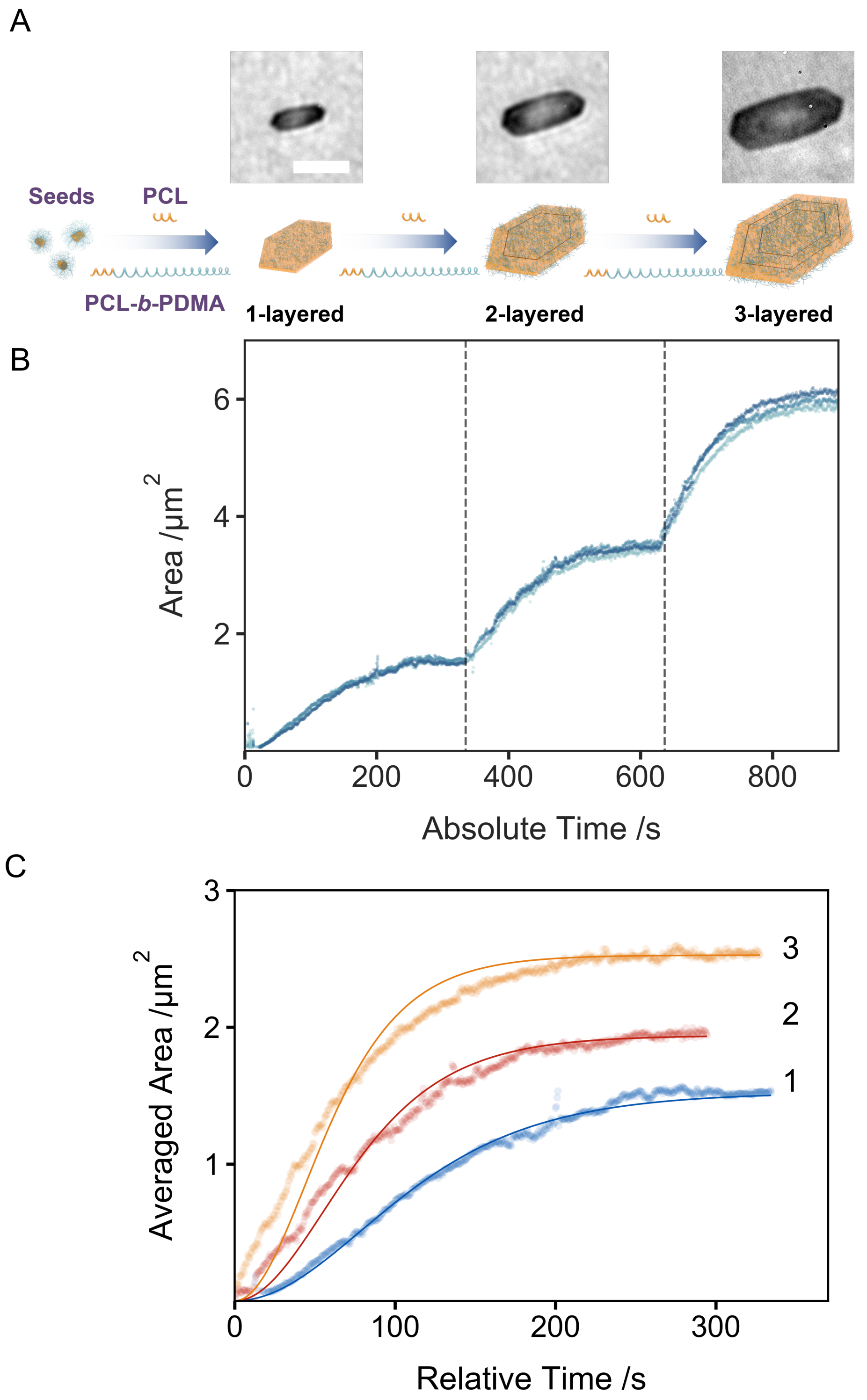

Figure 5.9: **iSCAT monitoring of 3-layered platelet formation.**
50 µL 0.1 µg mL^{-1} seed solution was spin-coated onto the surface, the PCL$_{45}$:PCL$_{45}$-*b*-PDMA$_{348}$ unimer solution was added at concentrations of 4.17, 5.56 and 8.33 µg mL^{-1} for each layer. **(A)** Schematic illustration of 3-layered platelet formation via living CDSA. Raw iSCAT images corresponding to each stage are provided (scale bar: 2 µm). **(B)** Evolution of three 3-layered platelet areas over time. **(C)** The averaged area evolution of three platelets in B, with the start point synchronized to the corresponding time of addition. Rate constants extracted from the fitting for each layer are 0.017, 0.024, 0.03 s^{-1}, respectively. *Figure A is prepared by Tianlai Xia.*

To confirm our hypothesis, 2-layered platelets were prepared by sequential addition of PCL_{45}:PCL_{45}-*b*-$PDMA_{348}$ blends and pure PCL_{45} with controlled PCL_{45} concentration (0.83 µg mL^{-1} for both layers), which means there have been variations in the unimer composition used for each layer (see more details in Fig. 5.10A). Again, a hypothetical organization of unimers within the 2-layered platelet has been displayed in Fig. 5.10B. Since there are numerous factors, such as crystallization temperature [174], that influence the thickness of lamellar platelets, our current results cannot validate this hypothesis. As shown in Fig. 5.10C, the first layer of platelet formed with PCL_{45}:PCL_{45}-*b*-$PDMA_{348}$ blends exhibits a higher (negative) iSCAT contrast (i.e., darker) compared to the second layer prepared from pure PCL_{45}. This difference in contrast was likely due to the increased thickness of platelet regions formed from PCL_{45}:PCL_{45}-*b*-$PDMA_{348}$ relative to pure PCL_{45}. To confirm this, the same sample was then sent for AFM measurement. As shown in Fig. 5.10E and F, the first layer formed with PCL_{45}:PCL_{45}-*b*-$PDMA_{348}$ blends is indeed thicker than the second layer formed with pure PCL_{45}. As a result, iSCAT contrast can act as an indicator to report the variation in unimer composition. Furthermore, this result elucidates the correlation between iSCAT contrast and platelet thickness. Through the integration of iSCAT and AFM data, we can construct a calibration curve delineating the relationship between platelet thickness and contrast for the platelets with similar refractive index. This approach offers a more efficient alternative for evaluating the morphological characteristics of platelets.

Upon closer examination of the AFM height profile of the first layer shown in Fig. 5.10E, it becomes evident that, in comparison to the outer region of the first layer, the height of the inner region is lower but more similar to the second layer. We assume this is caused by the nonuniform distribution of PCL_{45} and PCL_{45}-*b*-$PDMA_{348}$ because of crystallization rates difference, which has also been observed in the 3-layered platelet formation. Thus, the kinetics was examined. As illustrated by Fig. 5.10C, with the same PCL_{45} concentration (excluding PCL_{45} in the BCPs), the introduction of BCPs significantly slowed down the reaction. While the second layer prepared with pure PCL_{45} had completed its growth within the same reaction duration, the second layer prepared with PCL_{45}:PCL_{45}-*b*-$PDMA_{348}$ blends was still growing. Although it was impossible to reliably fit the data in this single experiment due to inadequate

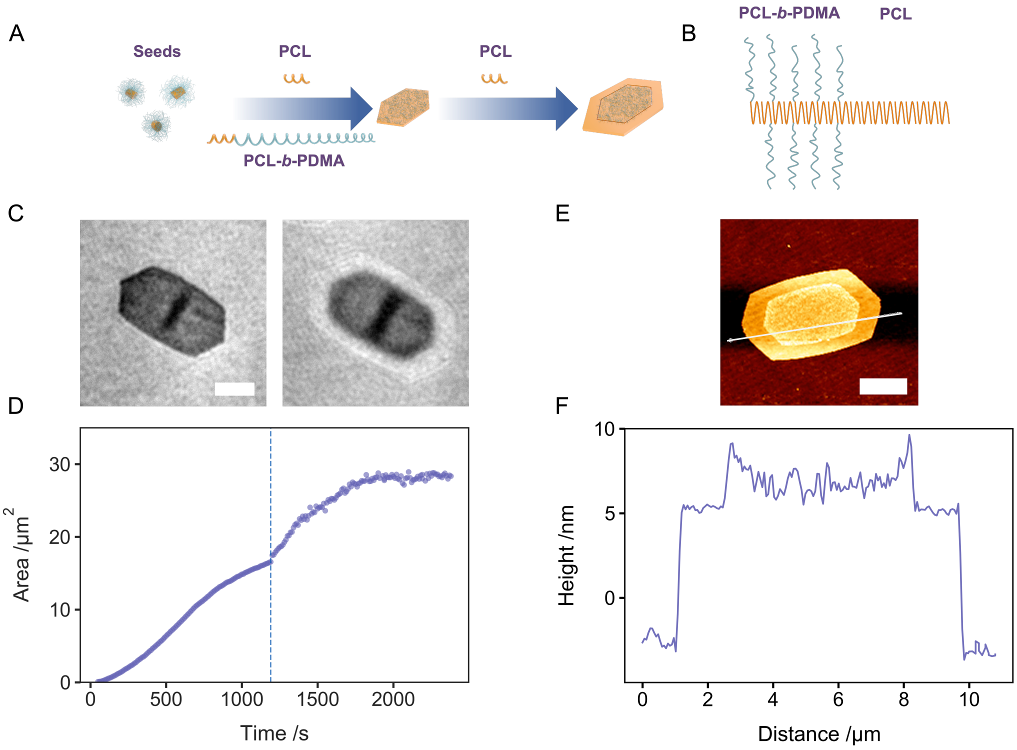

Figure 5.10: **iSCAT monitoring of 2-layered platelet formation.**
(A) Schematic illustration of 2-layered platelet formation using varied unimer composition for each layer via living CDSA. **(B)** Schematic illustration of unimer organization within a multilayered platelet. **(C)**Montage of iSCAT images during 2-layered platelet growth (scale bar: 2 μm). 50 μL 0.1 μg mL^{-1} seed solution was spin-coated onto the cleaned coverslip. To prepare the first layer 1.67 μg mL^{-1} PCL$_{45}$/PCL$_{45}$-*b*-PDMA$_{348}$ blends which contains 0.83 μg mL^{-1} PCL$_{45}$ was added onto the seed-coated surface. The second layer was prepared with 0.83 μg mL^{-1} pure PCL$_{45}$. **(D)** Size evolution of a 2-layered platelet. **(E)** AFM image of 2-layered platelet in B and C (scale bar: 3 μm). **(F)** Height profiles corresponding to the cross-section drawn in D. *AFM data were collected by Tianlai Xia.*

data collection for the first layer, the growth curve and size increase for each layer exhibited significant differences. Consequently, this result confirms that BCP and HP exhibit distinct kinetic behaviors, pure PCL$_{45}$ crystallizes faster than the unimer blends, so for the region prepared with the PCL$_{45}$:PCL$_{45}$-*b*-PDMA$_{348}$ blends (i.e., Fig. 5.9A and the first layer in Fig. 5.10B), PCL$_{45}$ dominates the crystallization and assembly once the seeds are introduced. When most of PCL$_{45}$ has been consumed, PCL$_{45}$-*b*-PDMA$_{348}$ takes over the reaction and assembles onto the platelet to form its outer region. As a result, the nonuniform distribution of PCL$_{45}$ and PCL$_{45}$-*b*-PDMA$_{348}$ can be reflected by iSCAT contrast variation.

Following this protocol, more complex architectures can be prepared. As shown in Fig. 5.11, by sequential addition of HP/BCP and HP, 4-layered platelets were successfully prepared (Movie

S4 in Appendix). These results further confirm the previously drawn assumption. From Fig. 5.11A, we can see that iSCAT contrast can report the variation of unimer composition between each layer, meanwhile, the nonuniform distribution of HP and BCP in the first layer can also be visualized through iSCAT contrast variation. Moreover, as can be seen in Fig. 5.11B, pure PCL_{45} exhibits kinetic behaviors different from PCL_{45} and PCL_{45}-*b*-$PDMA_{348}$ blends.

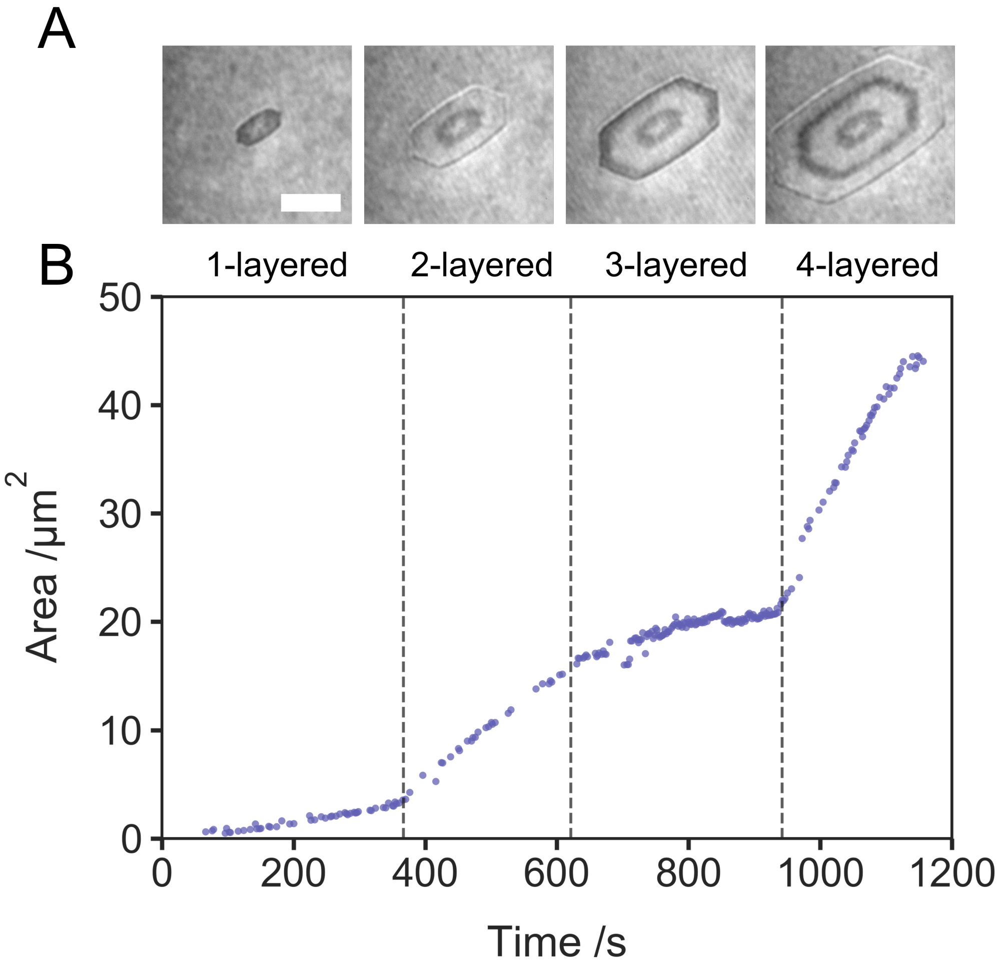

Figure 5.11: **Monitoring of 4-layered platelet formation.**
50 µL 0.1 µg mL^{-1} seed solution was spin-coated onto the surface, alternatingly addition of HP/BCP and HP unimer solution at concentrations of 1.67, 2.08, 3.33, and 4.17 µg mL^{-1} for each layer. **(A)** Montage of images collected during 4-layered platelet growth (scale bar: 3 µm). **(B)** Size evolution of a 4-layered platelet.

5.5 Summary and further work

In this study, iSCAT was successfully applied to monitor CDSA platelet formation under their native solution environment with sub-millisecond temporal resolution. Beyond its capabilities for real-time monitoring, iSCAT also holds significant promise as a potential technique for large batch sample characterization, offering advantages such as fast data collection, low cost, simple sample preparation, and high throughput.

This method has enabled us to quantify the dependence of living CDSA reaction kinetics and morphology on unimer concentration, seed concentration, and selective solubility. By adjusting the unimer-to-seed ratio, the final platelet dimension as well as the assembly rate can be controlled. Moreover, a change in solvent conditions can be used as an effective way to modify the morphology of the platelets. In addition, multi-layered platelet formation was also monitored in real-time. By combining iSCAT and AFM techniques, we were able to prove that differences in iSCAT contrast can provide detailed information in unimer composition inside a single platelet. This further indicated that iSCAT can be considered as a refractive index microscope, which can be used to report the changes in the optical properties of objects with high sensitivity. Lastly, it is also worth highlighting that the applications of iSCAT are not only limited to CDSA platelet characterization, similar self-assembly micelles ranging from 0D nanoparticles, 1D fibril structures to 2D platelet structures with refractive indices different from their surrounding medium might all be detected by iSCAT [67, 68, 218], which shows its potential as a characterization tool for material science.

Although iSCAT shows a great capability for *in situ* real-time monitoring platelet formation, in this study, the samples for the kinetic study were predominately prepared in bulk and then sent for iSCAT characterization. From our results shown above, it can be noted that seed concentration profoundly affects the reaction, which means for the *in situ* kinetics study, strict surface seed density control is required. Our current spin-coating protocol provides insufficient reproducibility in seed density to be reliably used for this purpose. Immobilizing seeds onto the plasma-cleaned glass coverslip via hydrogen bonds might be a solution. A preliminary test was conducted using seeds prepared with poly(ε-caprolactone)-*b*-poly(2-vinylpyridine) (P2VP) block copolymers, which can be attached to the surface and subsequently initiate assembly upon the unimer addition as shown in Fig. 5.12. However, as one can observe from this result, this experiment needs further optimization, such as adjusting the surface seed density or unimer concentration. However, due to time limitations, this experiment is listed as part of future work.

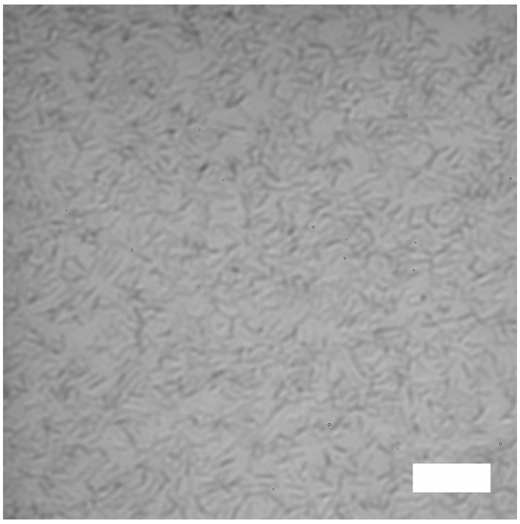

Figure 5.12: **Platelet growth initiated from surface-bonded P2VP seeds.**
P2VP seeds were immobilized onto the glass coverslip through hydrogen bonds, growth can be observed upon unimer addition (scale bar: 3 µm).

Chapter 6

Conclusions and future work

The emergence of optical single-molecule techniques allows researchers to zoom into the micro/nanoscale and characterize biological, chemical, and physical entities one at a time with extraordinary sensitivity, revealing a highly complex bigger picture of heterogeneous systems [1, 2, 13, 14, 68, 219–221]. For decades, fluorescence detection has been the mainstay for exploring various systems at the nanoscopic level, but this method also faces a series of fundamental labeling-related restrictions. By detecting light scattered by the nanoscopic objects, iSCAT offers label-free structural and dynamical characterization, which successfully bypasses labeling-related limitations. When an incident of light reaches a nanoobject, it will always scatter a portion of light as long as there is a refractive index difference between the objects and its surroundings [41]. This means a wide spectrum of subjects (from soft matter to nanoparticles) can be detected using this imaging scheme, leading to broad applications in different fields. Furthermore, this inherent scattering signal does not degrade over time, allowing unlimited observation time. Besides long measurement, high imaging speed (up to 1 MHz [53]) is also achievable, as the scattering rate can be increased via a stronger illumination intensity without suffering from saturation (but still restricted by the detector capability and photodamage to the sample). Furthermore, iSCAT can be readily implemented in existing fluorescence microscopy setup [52, 55], which not only broadens the application of both techniques but also enables a more in-depth and comprehensive investigation of various systems.

Nevertheless, iSCAT does come with certain limitations. Label-free detection is a doubleedged sword; it circumvents the limitations of fluorescent labeling but also loses its specificity. Any object with a refractive index different from the environment would produce a scattering signal, making it challenging to distinguish from the object of interest. Many actions can be taken to tackle this issue, for example, ingeniously designed control experiments to identify the object of interest, surface modification to increase the affinity of the subject to the imaging surface, or in combination with fluorescence imaging to pinpoint the target object. Furthermore, as introduced before, iSCAT imaging requires a reference beam generated by reflection from the interface, which requires the object of interest at or near that interface. However, by introducing an external arm to act as a reference field, confocal iSCAT was successfully used for 3D live cell imaging (more than 4 µm above the interface).

Despite the aforementioned limitations, the profound impact of iSCAT on a wide range of fields is undeniable. Since its invention, iSCAT has played a pivotal role in characterizing the structural and dynamic properties of various biological systems, ranging from single protein molecules [18, 50, 222] to viruses [54, 223], lipid membranes [53, 224], and live cells [52, 71]. However, its potential extends far beyond biology. The studies presented in this thesis successfully showcased its significant capabilities in expanding its applications into various fields. We first utilized iSCAT to monitor the growth of individual polymer molecules from the surface. However, due to the presence of strong scattering copper nanoparticles during polymerization, the observation single polymer chain formation was problematic. As the preliminary data has proved that we the observation of individual nanoparticle formation via iSCAT is achievable, we next explored the kinetic heterogeneity exists during particle formation. Then iSCAT was also successfully used to monitor the assembly process of block copolymer, which provides insights into 2D platelet formation.

To be more specific, in Chapter 3, iSCAT was employed to investigate the heterogeneous kinetic behavior of individual polymer chains prepared via photoinduced initiators for continuous activator regeneration atom transfer radical polymerization. Although we were unable to obtain optimized results due to time constraints, its successful application in studying biopolymer growth proved that iSCAT holds significant potential in monitoring the formation of synthetic polymers [50]. Furthermore, in Chapter 4, in combination of iSCAT microscopy with photoreductant spatio-temporal control, NP kinetics at the level of individual particles was explored in real-time. This not only reveals the hidden heterogeneity that exists in NP growth kinetics, but also provides useful information for designing and synthesizing new and more complex NPs, which is critical for advancing the field of nanotechnology and realizing the full potential of NPs for drug delivery, plasmonics, and smart materials. Besides reporting the dynamic evolution of subwavelength objects, iSCAT can also be used to monitor the formation of micron-sized nanoplatelets prepared with crystallizable polymeric materials via living crystallization-driven self-assembly. As discussed in Chapter 5, the application of iSCAT in the living CDSA study allows the 2D platelet/multi-layered platelet formation to be monitored with a high requisition rate (up to 3 kHz) in a label-free manner for the first time. Through this method, we explored the impact of key reaction parameters, such as unimer concentration, seed concentration, and solvent composition, on the platelet growth rate, size, and morphology. In addition, iSCAT was also used as a refractive index microscope in this study, any local refractive index changes can be sensitively reflected by the iSCAT contrast variations. As a result, iSCAT can readily detect changes in the composition of unimers used for preparing different layers of multi-layered platelets or the nonuniform distribution of block copolymer and homopolymer within a single platelet. Beyond its capabilities for real-time monitoring, iSCAT can also serve as an efficient characterization technique due to its fast data collection, low cost, simple sample preparation, and high throughput. It's worth mentioning again that subjects of study are not limited to 2D platelets; iSCAT can be adapted for various systems, ranging from 0D nanoparticles to 1D nanofibers, 2D platelets, and 3D structures. This versatility underscores its immense potential in the field of material science.

As we conclude our current investigation, it becomes evident that there is still more work that needs to be undertaken. Chapter 2 introduced the generation of a calibration curve for metal nanoparticles, similarly, a calibration curve for soft matter would be of great importance for future applications. The contrasts of proteins or polymers with a range of molecular weights can be extracted to establish the relationship between protein/polymer molecular weight and their iSCAT contrast. This relationship should follow a similar trend as demonstrated by the calibration curve in Chapter 2. Furthermore, to complete the work presented in Chapter 3, which aims to utilize iSCAT for monitoring the growth of individual polymer chains, it is important to minimize the formation of copper nanoparticles. This may be achieved through the modification of polymerization conditions for PICAR ATRP, such as adjusting the pH of the reaction solution or varying the ratio of reaction components. Meanwhile, metal-free photo-initiated polymerization [124–126] can also be considered as a potential model system to test our method.

Furthermore, as detailed in Chapter 5, our current investigations have been limited to the kinetics of CDSA platelets prepared in bulk solution. The *in situ* kinetic study of CDSA platelet formation from the surface remains unknown. By employing seeds capable of forming hydrogen bonds with the plasma-cleaned glass coverslip, we will be able to attain precise control over the surface seed density. This approach will allow iSCAT to monitor platelet formation under various reaction conditions in real-time and enable a deeper exploration of the kinetics of platelets formed from the surface, facilitating comparisons with our existing results. iSCAT has been widely applied to study the dynamics of various systems, such as lipid diffusion on membrane, protein aggregation and transportation of bioparticles on the cell surface [45]. This has successfully showcased its great potential in investigating fast dynamics. However, due to limitations with our current setup, the concentration of unimer was kept relatively low to manage reaction kinetics for data collection. Introducing a flow system to the setup can effectively address this issue and fully utilize the capabilities of iSCAT for fast imaging in studying rapid dynamics.

With our current setup, we can detect soft matters such as proteins and polymers with a sensitivity reaching up to 70 kDa. Additionally, we are able to successfully detect metal nanoparticles as small as 10 nm. To gain deeper insights into the initial stage of reaction kinetics, further enhancement of detection sensitivity is necessary. By adopting an optical arrangement to engineer the balance between scattered and reflected signal can be an effective method. For example, by implementing a partial reflector to a standard iSCAT experimental arrangement, the reflected light reaches to the detector can be selectively attenuates, which leads to increased interferometric contrast [225]. In addition, when combined with advancements in hardware and software, such as advanced optics, detector technologies, and machine learning, detection sensitivities and precision can be effectively improved to levels as low as a few kDa. This will bring research in both dynamic studies and quantitative analysis to a new level, with more formerly unreachable information being extracted. For example, for the study conducted in Chapter 3, with improved sensitivity single polymer particles with lower molecular weight can be detected (without the presence of metal nanoparticles). This advancement allows for the extraction of their kinetic information at earlier stages. Moreover, rapid dynamics of biological processes can be followed with higher imaging speed, sub-cellular structures can be visualized with higher precision and accurate molecular weight analysis of individual molecules can be achieved. In the meantime, the application of iSCAT should also be introduce into other fields such as coacervate formation and the assembly of membrane attack complexes on membranes.

In conclusion, the advantages of iSCAT lie in its extensive scope for future applications and its interdisciplinary nature, which have been successfully demonstrated in this study. With iSCAT being introduced into more fields, it will become a transformative approach for providing quantitative information on nanoscopic structure and dynamics.

References

[1] Jaime Ortega Arroyo and Philipp Kukura. Non-fluorescent schemes for single-molecule detection, imaging and spectroscopy. *Nature Photonics*, 10(1):11–17, 2016.

[2] Helen Miller, Zhaokun Zhou, Jack Shepherd, Adam JM Wollman, and Mark C Leake. Single-molecule techniques in biophysics: a review of the progress in methods and applications. *Reports on Progress in Physics*, 81(2):024601, 2017.

[3] Sungchul Hohng, Chirlmin Joo, and Taekjip Ha. Single-molecule three-color fret. *Biophysical Journal*, 87(2):1328–1337, 2004.

[4] Yann Gambin and Ashok A Deniz. Multicolor single-molecule fret to explore protein folding and binding. *Molecular BioSystems*, 6(9):1540–1547, 2010.

[5] Anna Löschberger, Sebastian van de Linde, Marie-Christine Dabauvalle, Bernd Rieger, Mike Heilemann, Georg Krohne, and Markus Sauer. Super-resolution imaging visualizes the eightfold symmetry of gp210 proteins around the nuclear pore complex and resolves the central channel with nanometer resolution. *Journal of Cell Science*, 125(3):570–575, 2012.

[6] Joanna Andrecka, Jaime Ortega Arroyo, Yasuharu Takagi, Gabrielle de Wit, Adam Fineberg, Lachlan MacKinnon, Gavin Young, James R Sellers, and Philipp Kukura. Structural dynamics of myosin 5 during processive motion revealed by interferometric scattering microscopy. *Elife*, 4:e05413, 2015.

[7] Zhen Liu, Dong Xing, Qian Peter Su, Yun Zhu, Jiamei Zhang, Xinyu Kong, Boxin Xue, Sheng Wang, Hao Sun, Yile Tao, et al. Super resolution imaging and tracking of protein-

protein interactions in sub diffraction cellular space. *Biophysical Journal*, 108(2):36a, 2015.

[8] Richard W Taylor, Reza Gholami Mahmoodabadi, Verena Rauschenberger, Andreas Giessl, Alexandra Schambony, and Vahid Sandoghdar. Interferometric scattering microscopy reveals microsecond nanoscopic protein motion on a live cell membrane. *Nature Photonics*, 13(7):480–487, 2019.

[9] Elio A Abbondanzieri, William J Greenleaf, Joshua W Shaevitz, Robert Landick, and Steven M Block. Direct observation of base-pair stepping by rna polymerase. *Nature*, 438(7067):460–465, 2005.

[10] Jeffrey R Moffitt, Yann R Chemla, David Izhaky, and Carlos Bustamante. Differential detection of dual traps improves the spatial resolution of optical tweezers. *Proceedings of the National Academy of Sciences*, 103(24):9006–9011, 2006.

[11] Bruno Samorì, G Zuccheri, and P Baschieri. Protein unfolding and refolding under force: methodologies for nanomechanics. *ChemPhysChem*, 6(1):29–34, 2005.

[12] Thomas Tischer, Robert Gralla-Koser, Vanessa Trouillet, Leonie Barner, Christopher Barner-Kowollik, and Cornelia Lee-Thedieck. Direct mapping of raft controlled macromolecular growth on surfaces via single molecule force spectroscopy. *ACS Macro Letters*, 5(4):498–503, 2016.

[13] Yujie Guo, Vivien Walter, Steven Vanuytsel, Christopher Parperis, Jason T Sengel, Eve E Weatherill, and Mark I Wallace. Real-time monitoring and control of nanoparticle formation. *Journal of the American Chemical Society*, 145(29):15809–15815, 2023.

[14] Donggeng Yu, Antonio Garcia IV, Suzanne A Blum, and Kevin D Welsher. Growth kinetics of single polymer particles in solution via active-feedback 3d tracking. *Journal of the American Chemical Society*, 144(32):14698–14705, 2022.

[15] William E Moerner. Single-molecule spectroscopy, imaging, and photocontrol: foundations

for super-resolution microscopy (nobel lecture). *Angewandte Chemie International Edition*, 54(28):8067–8093, 2015.

[16] Eric Betzig. Single molecules, cells, and super-resolution optics (nobel lecture). *Angewandte Chemie International Edition*, 54(28):8034–8053, 2015.

[17] Stefan W Hell. Nanoscopy with focused light. *Annalen der Physik*, 527(7-8):423–445, 2015.

[18] Marek Piliarik and Vahid Sandoghdar. Direct optical sensing of single unlabelled proteins and super-resolution imaging of their binding sites. *Nature Communications*, 5(1):4495, 2014.

[19] William E Moerner and Lothar Kador. Optical detection and spectroscopy of single molecules in a solid. *Physical Review Letters*, 62(21):2535, 1989.

[20] Rupsa Datta, Tiffany M Heaster, Joe T Sharick, Amani A Gillette, and Melissa C Skala. Fluorescence lifetime imaging microscopy: fundamentals and advances in instrumentation, analysis, and applications. *Journal of Biomedical Optics*, 25(7):071203–071203, 2020.

[21] Jeff W Lichtman and José-Angel Conchello. Fluorescence microscopy. *Nature Methods*, 2(12):910–919, 2005.

[22] Michael J Sanderson, Ian Smith, Ian Parker, and Martin D Bootman. Fluorescence microscopy. *Cold Spring Harbor Protocols*, 2014(10):pdb–top071795, 2014.

[23] Hellen C Ishikawa-Ankerhold, Richard Ankerhold, and Gregor PC Drummen. Advanced fluorescence microscopy techniques—frap, flip, flap, fret and flim. *Molecules*, 17(4):4047–4132, 2012.

[24] Subhasis Adhikari and Michel Orrit. Progress and perspectives in single-molecule optical spectroscopy. *The Journal of Chemical Physics*, 156(16), 2022.

[25] Peng Fei Gao, Gang Lei, and Cheng Zhi Huang. Dark-field microscopy: recent advances in accurate analysis and emerging applications. *Analytical Chemistry*, 93(11):4707–4726, 2021.

[26] Anne Straube. *Microtubule dynamics: methods and protocols*. Springer, 2011.

[27] Gavin Young and Philipp Kukura. Interferometric scattering microscopy. *Annual Review of Physical Chemistry*, 70:301–322, 2019.

[28] Weiqing Yang, Zhihong Wei, Yan Nie, and Yuxi Tian. Optical detection and imaging of nonfluorescent matter at the single-molecule/particle level. *The Journal of Physical Chemistry Letters*, 13(41):9618–9631, 2022.

[29] Shasha Chong, Wei Min, and X Sunney Xie. Ground-state depletion microscopy: detection sensitivity of single-molecule optical absorption at room temperature. *The journal of Physical Chemistry Letters*, 1(23):3316–3322, 2010.

[30] A Gaiduk, M Yorulmaz, PV Ruijgrok, and M Orrit. Room-temperature detection of a single molecule's absorption by photothermal contrast. *Science*, 330(6002):353–356, 2010.

[31] Philipp Kukura, Michele Celebrano, Alois Renn, and Vahid Sandoghdar. Single-molecule sensitivity in optical absorption at room temperature. *The Journal of Physical Chemistry Letters*, 1(23):3323–3327, 2010.

[32] David Boyer, Philippe Tamarat, Abdelhamid Maali, Brahim Lounis, and Michel Orrit. Photothermal imaging of nanometer-sized metal particles among scatterers. *Science*, 297(5584):1160–1163, 2002.

[33] Alexander Gaiduk, Paul V Ruijgrok, Mustafa Yorulmaz, and Michel Orrit. Detection limits in photothermal microscopy. *Chemical Science*, 1(3):343–350, 2010.

[34] Markus Selmke, Marco Braun, and Frank Cichos. Photothermal single-particle microscopy: detection of a nanolens. *Acs Nano*, 6(3):2741–2749, 2012.

[35] Meindert A van Dijk, Anna L Tchebotareva, Michel Orrit, Markus Lippitz, Stéphane Berciaud, David Lasne, Laurent Cognet, and Brahim Lounis. Absorption and scattering microscopy of single metal nanoparticles. *Physical Chemistry Chemical Physics*, 8(30):3486–3495, 2006.

[36] Stéphane Berciaud, Laurent Cognet, Gerhard A Blab, and Brahim Lounis. Photothermal heterodyne imaging of individual nonfluorescent nanoclusters and nanocrystals. *Phys Rev Lett*, 93(25):257402, Dec 2004.

[37] Laurent Cognet, Stéphane Berciaud, David Lasne, and Brahim Lounis. Photothermal methods for single nonluminescent nano-objects. *Analytical Chemistry*, 80(7):2288–2294, 2008.

[38] Pierre Vermeulen, Laurent Cognet, and Brahim Lounis. Photothermal microscopy: optical detection of small absorbers in scattering environments. *Journal of Microscopy*, 254(3):115–121, 2014.

[39] Subhasis Adhikari, Patrick Spaeth, Ashish Kar, Martin Dieter Baaske, Saumyakanti Khatua, and Michel Orrit. Photothermal microscopy: imaging the optical absorption of single nanoparticles and single molecules. *ACS Nano*, 14(12):16414–16445, 2020.

[40] Jung-Dae Kim, Dong Uk Kim, Chan Bae Jeong, Ilkyu Han, Ji Yong Bae, Hwan Hur, Ki-Hwan Nam, Sangwon Hyun, I Jong Kim, Kye-Sung Lee, et al. Wide-field photothermal reflectance spectroscopy for single nanoparticle absorption spectrum analysis. *Nanophotonics*, 10(13):3433–3440, 2021.

[41] Craig F Bohren and Donald R Huffman. *Absorption and scattering of light by small particles*. John Wiley & Sons, 2008.

[42] ASG Curtis. The mechanism of adhesion of cells to glass: a study by interference reflection microscopy. *The Journal of Cell Biology*, 20(2):199–215, 1964.

[43] Kalkbrenner Lindfors, Thomas Kalkbrenner, Patrick Stoller, and Vahid Sandoghdar. Detection and spectroscopy of gold nanoparticles using supercontinuum white light confocal microscopy. *Physical Review Letters*, 93(3):037401, 2004.

[44] Jaime Ortega-Arroyo and Philipp Kukura. Interferometric scattering microscopy (iscat): new frontiers in ultrafast and ultrasensitive optical microscopy. *Physical Chemistry Chemical Physics*, 14(45):15625–15636, 2012.

[45] Richard W Taylor and Vahid Sandoghdar. Interferometric scattering microscopy: seeing single nanoparticles and molecules via rayleigh scattering. *Nano Letters*, 19(8):4827–4835, 2019.

[46] Richard W Taylor and Vahid Sandoghdar. Interferometric scattering (iscat) microscopy and related techniques. In *Label-free super-resolution microscopy*, pages 25–65. Springer, 2019.

[47] Houman Mirzaalian Dastjerdi, Mahyar Dahmardeh, André Gemeinhardt, Reza Gholami Mahmoodabadi, Harald Köstler, and Vahid Sandoghdar. Optimized analysis for sensitive detection and analysis of single proteins via interferometric scattering microscopy. *Journal of Physics D: Applied Physics*, 55(5):054002, 2021.

[48] Lee Priest, Jack S Peters, and Philipp Kukura. Scattering-based light microscopy: from metal nanoparticles to single proteins. *Chemical Reviews*, 121(19):11937–11970, 2021.

[49] Kristỳna Holanová, Milan Vala, and Marek Piliarik. Optical imaging and localization of prospective scattering labels smaller than a single protein. *Optics & Laser Technology*, 109:323–327, 2019.

[50] Gavin Young, Nikolas Hundt, Daniel Cole, Adam Fineberg, Joanna Andrecka, Andrew Tyler, Anna Olerinyova, Ayla Ansari, Erik G Marklund, Miranda P Collier, et al. Quantitative mass imaging of single biological macromolecules. *Science*, 360(6387):423–427, 2018.

[51] Mahyar Dahmardeh, Houman Mirzaalian Dastjerdi, Hisham Mazal, Harald Köstler, and Vahid Sandoghdar. Self-supervised machine learning pushes the sensitivity limit in label-free detection of single proteins below 10 kda. *Nature Methods*, 20(3):442–447, 2023.

[52] Michelle Küppers, David Albrecht, Anna D Kashkanova, Jennifer Lühr, and Vahid Sandoghdar. Confocal interferometric scattering microscopy reveals 3d nanoscopic structure and dynamics in live cells. *Nature Communications*, 14(1):1962, 2023.

[53] Susann Spindler, Jens Ehrig, Katharina König, Tristan Nowak, Marek Piliarik, Hannah E Stein, Richard W Taylor, Elisabeth Garanger, Sébastien Lecommandoux, Isabel D Alves, et al. Visualization of lipids and proteins at high spatial and temporal resolution via interferometric scattering (iscat) microscopy. *Journal of Physics D: Applied Physics*, 49(27):274002, 2016.

[54] Philipp Kukura, Helge Ewers, Christian Müller, Alois Renn, Ari Helenius, and Vahid Sandoghdar. High-speed nanoscopic tracking of the position and orientation of a single virus. *Nature Methods*, 6(12):923–927, 2009.

[55] Yi-Teng Hsiao, Tsai-Ying Wu, Bo-Kuan Wu, Shi-Wei Chu, and Chia-Lung Hsieh. Spinning disk interferometric scattering confocal microscopy captures millisecond timescale dynamics of living cells. *Optics Express*, 30(25):45233–45245, 2022.

[56] Jaime Ortega Arroyo, Daniel Cole, and Philipp Kukura. Interferometric scattering microscopy and its combination with single-molecule fluorescence imaging. *Nature Protocols*, 11(4):617–633, 2016.

[57] J Ortega Arroyo, J Andrecka, KM Spillane, N Billington, Y Takagi, JR Sellers, and P Kukura. Label-free, all-optical detection, imaging, and tracking of a single protein. *Nano Letters*, 14(4):2065–2070, 2014.

[58] Matthew P McDonald, André Gemeinhardt, Katharina König, Marek Piliarik, Stefanie Schaffer, Simon VKöniglkl, Michael Aigner, Andreas Mackensen, and Vahid Sandoghdar. Visualizing single-cell secretion dynamics with single-protein sensitivity. *Nano Letters*, 18(1):513–519, 2018.

[59] Thomas L McMeekin, Mildred Wilensky, and Merton L Groves. Refractive indices of proteins in relation to amino acid composition and specific volume. *Biochemical and Biophysical Research Communications*, 7(2):151–156, 1962.

[60] Rita Strack. Scattering microscopy takes single-particle tracking to the next level. *Nature Methods*, 16(6):455–455, 2019.

[61] Richard W Taylor, Cornelia Holler, Reza Gholami Mahmoodabadi, Michelle Küppers, Houman Mirzaalian Dastjerdi, Vasily Zaburdaev, Alexandra Schambony, and Vahid Sandoghdar. High-precision protein-tracking with interferometric scattering microscopy. *Frontiers in Cell and Developmental Biology*, page 1194, 2020.

[62] Yi-Hung Liao, Chih-Hsiang Lin, Ching-Ya Cheng, Wai Cheng Wong, Jz-Yuan Juo, and Chia-Lung Hsieh. Monovalent and oriented labeling of gold nanoprobes for the high-resolution tracking of a single-membrane molecule. *ACS Nano*, 13(10):10918–10928, 2019.

[63] Hsiao-Mei Wu, Ying-Hsiu Lin, Tzu-Chi Yen, and Chia-Lung Hsieh. Nanoscopic substructures of raft-mimetic liquid-ordered membrane domains revealed by high-speed single-particle tracking. *Scientific Reports*, 6(1):20542, 2016.

[64] Aaron M Goldfain, Rees F Garmann, Yan Jin, Yoav Lahini, and Vinothan N Manoharan. Dynamic measurements of the position, orientation, and dna content of individual unlabeled bacteriophages. *The Journal of Physical Chemistry B*, 120(26):6130–6138, 2016.

[65] Sjoerd Stallinga and Bernd Rieger. Accuracy of the gaussian point spread function model in 2d localization microscopy. *Optics Express*, 18(24):24461–24476, 2010.

[66] Ying-Hsiu Lin, Wei-Lin Chang, and Chia-Lung Hsieh. Shot-noise limited localization of single 20 nm gold particles with nanometer spatial precision within microseconds. *Optics Express*, 22(8):9159–9170, 2014.

[67] Joanna Andrecka, Jaime Ortega Arroyo, Katie Lewis, Robert A Cross, and Philipp Kukura. Label-free imaging of microtubules with sub-nm precision using interferometric scattering microscopy. *Biophysical journal*, 110(1):214–217, 2016.

[68] Anna D Kashkanova, Martin Blessing, André Gemeinhardt, Didier Soulat, and Vahid Sandoghdar. Precision size and refractive index analysis of weakly scattering nanoparticles in polydispersions. *Nature Methods*, 19(5):586–593, 2022.

[69] Joanna Andrecka, Katelyn M Spillane, Jaime Ortega-Arroyo, and Philipp Kukura. Direct observation and control of supported lipid bilayer formation with interferometric scattering microscopy. *ACS Nano*, 7(12):10662–10670, 2013.

[70] Gabrielle De Wit, John SH Danial, Philipp Kukura, and Mark I Wallace. Dynamic label-free imaging of lipid nanodomains. *Proceedings of the National Academy of Sciences*, 112(40):12299–12303, 2015.

[71] Gabrielle de Wit, David Albrecht, Helge Ewers, and Philipp Kukura. Revealing compartmentalized diffusion in living cells with interferometric scattering microscopy. *Biophysical Journal*, 114(12):2945–2950, 2018.

[72] Adam Fineberg. *Interferometric scattering microscopy: from bacterial dynamics to molecular assembly.* PhD thesis, University of Oxford, 2019.

[73] Daniel B. Allan, Thomas Caswell, Nathan C. Keim, Casper M. van der Wel, and Ruben W. Verweij. soft-matter/trackpy: Trackpy v0.5.0, April 2021.

[74] Luke Melo, Angus Hui, Matt Kowal, Eric Boateng, Zahra Poursorkh, Edène Rocheron, Jake Wong, Ashton Christy, and Edward Grant. Size distributions of gold nanoparticles in solution measured by single-particle mass photometry. *The Journal of Physical Chemistry B*, 125(45):12466–12475, 2021.

[75] Volker Jacobsen, Patrick Stoller, Christian Brunner, Viola Vogel, and Vahid Sandoghdar. Interferometric optical detection and tracking of very small gold nanoparticles at a water-glass interface. *Optics Express*, 14(1):405–414, 2006.

[76] Pauli Virtanen, Ralf Gommers, Travis E. Oliphant, Matt Haberland, Tyler Reddy, David Cournapeau, Evgeni Burovski, Pearu Peterson, Warren Weckesser, Jonathan Bright, Stéfan J. van der Walt, Matthew Brett, Joshua Wilson, K. Jarrod Millman, Nikolay Mayorov, Andrew R. J. Nelson, Eric Jones, Robert Kern, Eric Larson, C J Carey, İlhan Polat, Yu Feng, Eric W. Moore, Jake VanderPlas, Denis Laxalde, Josef Perktold, Robert Cimrman, Ian Henriksen, E. A. Quintero, Charles R. Harris, Anne M. Archibald, Antônio H.

Ribeiro, Fabian Pedregosa, Paul van Mulbregt, and SciPy 1.0 Contributors. SciPy 1.0: Fundamental Algorithms for Scientific Computing in Python. *Nature Methods*, 17:261–272, 2020.

[77] Harender Singh Bisht and Alok Kumar Chatterjee. Living free-radical polymerization—a review. *Journal of Macromolecular Science, Part C: Polymer Reviews*, 41(3):139–173, 2001.

[78] Hassan Namazi. Polymers in our daily life. *BioImpacts: BI*, 7(2):73, 2017.

[79] Fabio di Lena and Krzysztof Matyjaszewski. Transition metal catalysts for controlled radical polymerization. *Progress in Polymer Science*, 35(8):959–1021, 2010.

[80] Dietrich Braun et al. Origins and development of initiation of free radical polymerization processes. *International Journal of Polymer Science*, 2009, 2009.

[81] Daniel Colombani. Chain-growth control in free radical polymerization. *Progress in Polymer Science*, 22(8):1649–1720, 1997.

[82] Bunichiro Yamada and Per B. Zetterlund. General chemistry of radical polymerization. In Krzysztof Matyjaszewski and Thomas P. Davis, editors, *Handbook of Radical Polymerization*. Wiley Online Library, 2002.

[83] Krzysztof Matyjaszewski and James Spanswick. Controlled/living radical polymerization. *Materials Today*, 8(3):26–33, 2005.

[84] Nghia P Truong, Glen R Jones, Kate GE Bradford, Dominik Konkolewicz, and Athina Anastasaki. A comparison of raft and atrp methods for controlled radical polymerization. *Nature Reviews Chemistry*, 5(12):859–869, 2021.

[85] Ronald W Nunes, John R Martin, and Julian F Johnson. Influence of molecular weight and molecular weight distribution on mechanical properties of polymers. *Polymer Engineering & Science*, 22(4):205–228, 1982.

[86] K. Balani, V. Verma, A. Agarwal, and R. Narayan. Physical, thermal, and mechanical properties of polymers. In K. Balani, V. Verma, A. Agarwal, and R. Narayan, editors, *Biosurfaces*. John Wiley & Sons, Inc., 2014.

[87] Veronika Kottisch, Dillon T Gentekos, and Brett P Fors. "shaping" the future of molecular weight distributions in anionic polymerization. *ACS Macro Letters*, 5(7):796–800, 2016.

[88] D Roy, CB Giller, TE Hogan, and CM Roland. The rheology and gelation of bidisperse 1, 4-polybutadiene. *Polymer*, 81:111–118, 2015.

[89] DG Hassell, J Embery, TCB McLeish, and MR Mackley. An experimental evaluation of the formation of an instability in monodisperse and polydisperse polystyrenes. *Journal of Non-Newtonian Fluid Mechanics*, 157(1-2):1–14, 2009.

[90] Anshuman Shrivastava. Polymerization. In Anshuman Shrivastava, editor, *Introduction to Plastics Engineering*, pages 17–48. William Andrew Publishing, 2018.

[91] RG Gilbert, M Hess, AD Jenkins, RG Jones, P Kratochvil, and RFT Stepto. Dispersity in polymer science. *Pure Appl. Chem*, 81(2):351–353, 2009.

[92] Richard Whitfield, Nghia P Truong, Daniel Messmer, Kostas Parkatzidis, Manon Rolland, and Athina Anastasaki. Tailoring polymer dispersity and shape of molecular weight distributions: methods and applications. *Chemical Science*, 10(38):8724–8734, 2019.

[93] Krzysztof Matyjaszewski. Mechanistic aspects of atom transfer radical polymerization. In *Controlled Radical Polymerization*, pages 258–283. American Chemical Society, 1998.

[94]) YK Chong, Tam PT Le, Graeme Moad, Ezio Rizzardo, and San H Thang. A more versatile route to block copolymers and other polymers of complex architecture by living radical polymerization: the raft process. *Macromolecules*, 32(6):2071–2074, 1999.

[95] Craig J Hawker, Anton W Bosman, and Eva Harth. New polymer synthesis by nitroxide mediated living radical polymerizations. *Chemical Reviews*, 101(12):3661–3688, 2001.

[96] Nicolay V Tsarevsky and Krzysztof Matyjaszewski. “green” atom transfer radical polymerization: from process design to preparation of well-defined environmentally friendly polymeric materials. *Chemical Reviews*, 107(6):2270–2299, 2007.

[97] Athina Anastasaki, Vasiliki Nikolaou, Gabit Nurumbetov, Paul Wilson, Kristian Kempe, John F Quinn, Thomas P Davis, Michael R Whittaker, and David M Haddleton. Cu (0)-mediated living radical polymerization: a versatile tool for materials synthesis. *Chemical Reviews*, 116(3):835–877, 2016.

[98] Jin-Shan Wang and Krzysztof Matyjaszewski. Controlled/” living” radical polymerization. atom transfer radical polymerization in the presence of transition-metal complexes. *Journal of the American Chemical Society*, 117(20):5614–5615, 1995.

[99] Charlotte Juel Fristrup, Katja Jankova, and Søren Hvilsted. Surface-initiated atom transfer radical polymerization—a technique to develop biofunctional coatings. *Soft Matter*, 5(23):4623–4634, 2009.

[100] Amir Khabibullin, Erlita Mastan, Krzysztof Matyjaszewski, and Shiping Zhu. Surface-initiated atom transfer radical polymerization. In Krzysztof Matyjaszewski and Nicolay V. Tsarevsky, editors, *Controlled Radical Polymerization at and from Solid Surfaces*, pages 29–76. Springer, 2016.

[101] Krzysztof Matyjaszewski and Jianhui Xia. Atom transfer radical polymerization. *Chemical Reviews*, 101(9):2921–2990, 2001.

[102] Devon A Shipp. Living radical polymerization: Controlling molecular size and chemical functionality in vinyl polymers. *Journal of Macromolecular Science, Part C: Polymer Reviews*, 45(2):171–194, 2005.

[103] Krzysztof Matyjaszewski. Atom transfer radical polymerization (atrp): current status and future perspectives. *Macromolecules*, 45(10):4015–4039, 2012.

[104] Marco Fantin, Abdirisak A Isse, Armando Gennaro, and Krzysztof Matyjaszewski. Un-

derstanding the fundamentals of aqueous atrp and defining conditions for better control. *Macromolecules*, 48(19):6862–6875, 2015.

[105] Cyrille Boyer, Nathaniel Alan Corrigan, Kenward Jung, Diep Nguyen, Thuy-Khanh Nguyen, Nik Nik M Adnan, Susan Oliver, Sivaprakash Shanmugam, and Jonathan Yeow. Copper-mediated living radical polymerization (atom transfer radical polymerization and copper (0) mediated polymerization): from fundamentals to bioapplications. *Chemical Reviews*, 116(4):1803–1949, 2016.

[106] Antonina Simakova, Saadyah E Averick, Dominik Konkolewicz, and Krzysztof Matyjaszewski. Aqueous arget atrp. *Macromolecules*, 45(16):6371–6379, 2012.

[107] Michiel Langerman and Dennis GH Hetterscheid. Fast oxygen reduction catalyzed by a copper (ii) tris (2-pyridylmethyl) amine complex through a stepwise mechanism. *Angewandte Chemie International Edition*, 58(37):12974–12978, 2019.

[108] VA Bhanu and K Kishore. Role of oxygen in polymerization reactions. *Chemical Reviews*, 91(2):99–117, 1991.

[109] Sajjad Dadashi-Silab, Sean Doran, and Yusuf Yagci. Photoinduced electron transfer reactions for macromolecular syntheses. *Chemical Reviews*, 116(17):10212–10275, 2016.

[110] Xiangcheng Pan, Mehmet Atilla Tasdelen, Joachim Laun, Thomas Junkers, Yusuf Yagci, and Krzysztof Matyjaszewski. Photomediated controlled radical polymerization. *Progress in Polymer Science*, 62:73–125, 2016.

[111] Mao Chen, Mingjiang Zhong, and Jeremiah A Johnson. Light-controlled radical polymerization: mechanisms, methods, and applications. *Chemical Reviews*, 116(17):10167–10211, 2016.

[112] Grzegorz Szczepaniak, Matylda Łagodzińska, Sajjad Dadashi-Silab, Adam Gorczyński, and Krzysztof Matyjaszewski. Fully oxygen-tolerant atom transfer radical polymerization triggered by sodium pyruvate. *Chemical Science*, 11(33):8809–8816, 2020.

[113] Chunming Liu, Susil Baral, Kai Gu, Xianwen Mao, and Peng Chen. Real-time single-polymer growth towards single-monomer resolution. *Trends in Chemistry*, 3(4):318–331, 2021.

[114] Dominik Wöll, Hiroshi Uji-i, Tobias Schnitzler, Jun-ichi Hotta, Peter Dedecker, Andreas Herrmann, Frans C De Schryver, Klaus Müllen, and Johan Hofkens. Radical polymerization tracked by single molecule spectroscopy. *Angewandte Chemie International Edition*, 47(4):783–787, 2008.

[115] Maritza G. Neira-Velázquez, Juan T. Rodríguez-Hernández, Emilio Hernández-Hernández, and Ana R. Y. Ruiz-Martínez. Polymer molecular weight measurement. In *Handbook of Polymer Synthesis, Characterization, and Processing*, pages 355–366. Wiley Online Books, 2013.

[116] André M Striegel. Size-exclusion chromatography: smaller, faster, multi-detection, and multi-dimensions. *Analytical and Bioanalytical Chemistry*, 390(1):303–305, 2008.

[117] Eric S Tillman, Amanda C Roof, Steven M Palmer, Beth Ann Zarko, Caton C Goodman, and Alissa M Roland. Synthesis of chromophore-labeled polymers and their molecular weight determination using uv–vis spectroscopy. *Journal of chemical education*, 83(8):1215, 2006.

[118] Chunming Liu, Kaori Kubo, Endian Wang, Kyu-Sung Han, Feng Yang, Guanqun Chen, Fernando A Escobedo, Geoffrey W Coates, and Peng Chen. Single polymer growth dynamics. *Science*, 358(6361):352–355, 2017.

[119] Quinn T Easter and Suzanne A Blum. Single turnover at molecular polymerization catalysts reveals spatiotemporally resolved reactions. *Angewandte Chemie International Edition*, 56(44):13772–13775, 2017.

[120] Quinn T Easter, Antonio Garcia IV, and Suzanne A Blum. Single-polymer–particle growth kinetics with molecular catalyst speciation and single-turnover imaging. *ACS Catalysis*, 9(4):3375–3383, 2019.

[121] Rong Ye, Xiangcheng Sun, Xianwen Mao, Felix S Alfonso, Susil Baral, Chunming Liu, Geoffrey W Coates, and Peng Chen. Optical sequencing of single synthetic polymers. *Nature Chemistry*, pages 1–8, 2023.

[122] Guo-Feng Luo, Wei-Hai Chen, and Xian-Zheng Zhang. 100th anniversary of macromolecular science viewpoint: poly (n-isopropylacrylamide)-based thermally responsive micelles. *ACS Macro Letters*, 9(6):872–881, 2020.

[123] Michaela Corina Crisan, Mocan Teodora, and Mocan Lucian. Copper nanoparticles: Synthesis and characterization, physiology, toxicity and antimicrobial applications. *Applied Sciences*, 12(1):141, 2021.

[124] Benjaporn Narupai, Zachariah A Page, Nicolas J Treat, Alaina J McGrath, Christian W Pester, Emre H Discekici, Neil D Dolinski, Gregory F Meyers, Javier Read de Alaniz, and Craig J Hawker. Simultaneous preparation of multiple polymer brushes under ambient conditions using microliter volumes. *Angewandte Chemie International Edition*, 57(41):13433–13438, 2018.

[125] Emre H Discekici, Christian W Pester, Nicolas J Treat, Jimmy Lawrence, Kaila M Mattson, Benjaporn Narupai, Edward P Toumayan, Yingdong Luo, Alaina J McGrath, Paul G Clark, et al. Simple benchtop approach to polymer brush nanostructures using visible-light-mediated metal-free atom transfer radical polymerization. *ACS Macro Letters*, 5(2):258–262, 2016.

[126] Nicolas J Treat, Hazel Sprafke, John W Kramer, Paul G Clark, Bryan E Barton, Javier Read de Alaniz, Brett P Fors, and Craig J Hawker. Metal-free atom transfer radical polymerization. *Journal of the American Chemical Society*, 136(45):16096–16101, 2014.

[127] Kiyoshi Nogi, Makio Naito, and Toyokazu Yokoyama. *Nanoparticle technology handbook*. Elsevier, 2012.

[128] V Chandrakala, Valmiki Aruna, and Gangadhara Angajala. Review on metal nanoparticles as nanocarriers: Current challenges and perspectives in drug delivery systems. *Emergent Materials*, 5(6):1593–1615, 2022.

[129] Masatake Midorigaoka Haruta, Tetsuhiko Kobayashi, Hiroshi Sano, and Nobumasa Yamada. Novel gold catalysts for the oxidation of carbon monoxide at a temperature far below 0 °c. *Chemistry Letters*, 16:405–408, 1987.

[130] Masatake Haruta. Size-and support-dependency in the catalysis of gold. *Catalysis today*, 36(1):153–166, 1997.

[131] Mark Turner, Vladimir B Golovko, Owain PH Vaughan, Pavel Abdulkin, Angel Berenguer-Murcia, Mintcho S Tikhov, Brian FG Johnson, and Richard M Lambert. Selective oxidation with dioxygen by gold nanoparticle catalysts derived from 55-atom clusters. *Nature*, 454(7207):981–983, 2008.

[132] Feng Wang, Yu-Cai Wang, Shuang Dou, Meng-Hua Xiong, Tian-Meng Sun, and Jun Wang. Doxorubicin-tethered responsive gold nanoparticles facilitate intracellular drug delivery for overcoming multidrug resistance in cancer cells. *ACS Nano*, 5(5):3679–3692, 2011.

[133] Shanta Dhar, Weston L Daniel, David A Giljohann, Chad A Mirkin, and Stephen J Lippard. Polyvalent oligonucleotide gold nanoparticle conjugates as delivery vehicles for platinum (iv) warheads. *Journal of the American Chemical Society*, 131(41):14652–14653, 2009.

[134] Erik C Dreaden, Sandra C Mwakwari, Quaovi H Sodji, Adegboyega K Oyelere, and Mostafa A El-Sayed. Tamoxifen- poly (ethylene glycol)- thiol gold nanoparticle conjugates: enhanced potency and selective delivery for breast cancer treatment. *Bioconjugate Chemistry*, 20(12):2247–2253, 2009.

[135] David A Giljohann, Dwight S Seferos, Andrew E Prigodich, Pinal C Patel, and Chad A Mirkin. Gene regulation with polyvalent sirna- nanoparticle conjugates. *Journal of the American Chemical Society*, 131(6):2072–2073, 2009.

[136] Laura C Kennedy, Lissett R Bickford, Nastassja A Lewinski, Andrew J Coughlin, Ying Hu, Emily S Day, Jennifer L West, and Rebekah A Drezek. A new era for cancer treatment: gold-nanoparticle-mediated thermal therapies. *Small*, 7(2):169–183, 2011.

[137] Nardine S Abadeer and Catherine J Murphy. Recent progress in cancer thermal therapy using gold nanoparticles. *Nanomaterials and Neoplasms*, pages 143–217, 2021.

[138] Ralph A Sperling, Pilar Rivera Gil, Feng Zhang, Marco Zanella, and Wolfgang J Parak. Biological applications of gold nanoparticles. *Chemical Society Reviews*, 37(9):1896–1908, 2008.

[139] Xiaohua Huang and Mostafa A El-Sayed. Gold nanoparticles: Optical properties and implementations in cancer diagnosis and photothermal therapy. *Journal of Advanced Research*, 1(1):13–28, 2010.

[140] Michael Kitching, Meghana Ramani, and Enrico Marsili. Fungal biosynthesis of gold nanoparticles: mechanism and scale up. *Microbial Biotechnology*, 8(6):904–917, 2015.

[141] David A Giljohann, Dwight S Seferos, Weston L Daniel, Matthew D Massich, Pinal C Patel, and Chad A Mirkin. Gold nanoparticles for biology and medicine. *Spherical Nucleic Acids*, pages 55–90, 2020.

[142] Luis M Liz-Marzán. Tailoring surface plasmons through the morphology and assembly of metal nanoparticles. *Langmuir*, 22(1):32–41, 2006.

[143] Günter Schmid. *Clusters and colloids: from theory to applications*. John Wiley & Sons, 2008.

[144] Muzahidul I Anik, Niaz Mahmud, Abdullah Al Masud, and Maruf Hasan. Gold nanoparticles (gnps) in biomedical and clinical applications: A review. *Nano Select*, 3(4):792–828, 2022.

[145] BN Khlebtsov and NG Khlebtsov. On the measurement of gold nanoparticle sizes by the dynamic light scattering method. *Colloid Journal*, 73(1):118–127, 2011.

[146] Wolfgang Haiss, Nguyen TK Thanh, Jenny Aveyard, and David G Fernig. Determination of size and concentration of gold nanoparticles from uv- vis spectra. *Analytical Chemistry*, 79(11):4215–4221, 2007.

[147] Mario M Modena, Bastian Rühle, Thomas P Burg, and Stefan Wuttke. Nanoparticle characterization: what to measure? *Advanced Materials*, 31(32):1901556, 2019.

[148] Eric E Finney and Richard G Finke. Nanocluster nucleation and growth kinetic and mechanistic studies: A review emphasizing transition-metal nanoclusters. *Journal of Colloid and Interface Science*, 317(2):351–374, 2008.

[149] Rute F Domingos, Mohamed A Baalousha, Yon Ju-Nam, M Marcia Reid, Nathalie Tufenkji, Jamie R Lead, Gary G Leppard, and Kevin J Wilkinson. Characterizing manufactured nanoparticles in the environment: multimethod determination of particle sizes. *Environmental Science & Technology*, 43(19):7277–7284, 2009.

[150] Jana Olson, Sergio Dominguez-Medina, Anneli Hoggard, Lin-Yung Wang, Wei-Shun Chang, and Stephan Link. Optical characterization of single plasmonic nanoparticles. *Chem Soc Rev*, 44(1):40–57, Jan 2015.

[151] Jan Becker, Olaf Schubert, and Carsten Sönnichsen. Gold nanoparticle growth monitored in situ using a novel fast optical single-particle spectroscopy method. *Nano Lett*, 7(6):1664–9, Jun 2007.

[152] Jing Cheng, Yang Liu, Xiaodong Cheng, Yan He, and Edward S Yeung. Real time observation of chemical reactions of individual metal nanoparticles with high-throughput single molecule spectral microscopy. *Anal Chem*, 82(20):8744–9, Oct 2010.

[153] Peter Georgiev, Assya Bojinova, Bistra Kostova, Denitsa Momekova, Thomas Bjornholm, and Konstantin Balashev. Implementing atomic force microscopy (afm) for studying kinetics of gold nanoparticle's growth. *Colloids and Surfaces A: Physicochemical and Engineering Aspects*, 434:154–163, 2013.

[154] See Wee Chee, Utkarsh Anand, Geeta Bisht, Shu Fen Tan, and Utkur Mirsaidov. Direct observations of the rotation and translation of anisotropic nanoparticles adsorbed at a liquid-solid interface. *Nano Lett*, 19(5):2871–2878, 05 2019.

[155] Yucheng Zhang, Debora Keller, Marta D Rossell, and Rolf Erni. Formation of au nanoparticles in liquid cell transmission electron microscopy: From a systematic study to engineered nanostructures. *Chem Mater*, 29(24):10518–10525, Dec 2017.

[156] Katelyn M Spillane, Jaime Ortega-Arroyo, Gabrielle de Wit, Christian Eggeling, Helge Ewers, Mark I Wallace, and Philipp Kukura. High-speed single-particle tracking of gm1 in model membranes reveals anomalous diffusion due to interleaflet coupling and molecular pinning. *Nano Letters*, 14(9):5390–5397, 2014.

[157] John Turkevich, Peter Cooper Stevenson, and James Hillier. A study of the nucleation and growth processes in the synthesis of colloidal gold. *Discussions of the Faraday Society*, 11:55–75, 1951.

[158] Judith Kimling, Maryrita Maier, Berta Okenve, Vassilios Kotaidis, H Ballot, and Anton Plech. Turkevich method for gold nanoparticle synthesis revisited. *The Journal of Physical Chemistry B*, 110(32):15700–15707, 2006.

[159] HH Huang, XP Ni, GL Loy, CH Chew, KL Tan, FC Loh, JF Deng, and GQ Xu. Photochemical formation of silver nanoparticles in poly (n-vinylpyrrolidone). *Langmuir*, 12(4):909–912, 1996.

[160] Y Zhou, CY Wang, YR Zhu, and ZY Chen. A novel ultraviolet irradiation technique for shape-controlled synthesis of gold nanoparticles at room temperature. *Chemistry of Materials*, 11(9):2310–2312, 1999.

[161] Masafumi Harada and Syoko Kizaki. Formation mechanism of gold nanoparticles synthesized by photoreduction in aqueous ethanol solutions of polymers using in situ quick scanning x-ray absorption fine structure and small-angle x-ray scattering. *Crystal Growth & Design*, 16(3):1200–1212, 2016.

[162] H Du Toit, TJ Macdonald, H Huang, IP Parkin, and A Gavriilidis. Continuous flow synthesis of citrate capped gold nanoparticles using uv induced nucleation. *RSC Advances*, 7(16):9632–9638, 2017.

[163] Murielle A Watzky, Eric E Finney, and Richard G Finke. Transition-metal nanocluster size vs formation time and the catalytically effective nucleus number: a mechanism-based treatment. *Journal of the American Chemical Society*, 130(36):11959–11969, 2008.

[164] Ching-Ya Cheng and Chia-Lung Hsieh. Background estimation and correction for high-precision localization microscopy. *ACS Photonics*, 4(7):1730–1739, 2017.

[165] Xiaohui Ji, Xiangning Song, Jun Li, Yubai Bai, Wensheng Yang, and Xiaogang Peng. Size control of gold nanocrystals in citrate reduction: the third role of citrate. *Journal of the American Chemical Society*, 129(45):13939–13948, 2007.

[166] DanV Goia and Egon Matijević. Tailoring the particle size of monodispersed colloidal gold. *Colloids and Surfaces A: Physicochemical and Engineering Aspects*, 146(1-3):139–152, 1999.

[167] Rabia Javed, Muhammad Zia, Sania Naz, Samson O Aisida, Noor ul Ain, and Qiang Ao. Role of capping agents in the application of nanoparticles in biomedicine and environmental remediation: recent trends and future prospects. *Journal of Nanobiotechnology*, 18:1–15, 2020.

[168] José Alberto Zamora-Justo, Paulina Abrica-González, Guillermo Rocael Vázquez-Martínez, Alejandro Muñoz-Diosdado, José Abraham Balderas-López, and Miguel Ibáñez-Hernández. Polyethylene glycol-coated gold nanoparticles as dna and atorvastatin delivery systems and cytotoxicity evaluation. *Journal of Nanomaterials*, 2019:1–11, 2019.

[169] Collin J Rodrigues, Julian A Bobb, Mallory G John, Sergey P Fisenko, M Samy El-Shall, and Katharine Moore Tibbetts. Nucleation and growth of gold nanoparticles initiated by nanosecond and femtosecond laser irradiation of aqueous [aucl 4]-. *Physical Chemistry Chemical Physics*, 20(45):28465–28475, 2018.

[170] Laysa M Frias Batista, Victoria Kathryn Meader, Katherine Romero, Karli Kunzler, Fariha Kabir, Amazin Bullock, and Katharine Moore Tibbetts. Kinetic control of [aucl4]- photochemical reduction and gold nanoparticle size with hydroxyl radical scavengers. *The Journal of Physical Chemistry B*, 123(33):7204–7213, 2019.

[171] Silviya Simeonova, Peter Georgiev, Kai S Exner, Lyuben Mihaylov, Diana Nihtianova, Kaloian Koynov, and Konstantin Balashev. Kinetic study of gold nanoparticles synthesized in the presence of chitosan and citric acid. *Colloids and Surfaces A: Physicochemical and Engineering Aspects*, 557:106–115, 2018.

[172] Felix H Schacher, Paul A Rupar, and Ian Manners. Functional block copolymers: nanostructured materials with emerging applications. *Angewandte Chemie International Edition*, 51(32):7898–7921, 2012.

[173] Yiyong Mai and Adi Eisenberg. Self-assembly of block copolymers. *Chemical Society Reviews*, 41(18):5969–5985, 2012.

[174] Tian Zhou, Hao Qi, Lin Han, Dmitri Barbash, and Christopher Y Li. Towards controlled polymer brushes via a self-assembly-assisted-grafting-to approach. *Nature Communications*, 7(1):11119, 2016.

[175] Wenxian Hu, Maryam Safari, Yong Zhou, Ricardo A Pérez-Camargo, Guoming Liu, Alejandro J M
”uller, and Dujin Wang. Comonomer inclusion in single crystals of isodimorphic random copolymers of butylene succinate and ε-caprolactone. *Macromolecules*, 56(13):5058–5067, 2023.

[176] Sylvia Ganda and Martina H Stenzel. Concepts, fabrication methods and applications of living crystallization-driven self-assembly of block copolymers. *Progress in Polymer Science*, 101:101195, 2020.

[177] Liam MacFarlane, Chuanqi Zhao, Jiandong Cai, Huibin Qiu, and Ian Manners. Emerging applications for living crystallization-driven self-assembly. *Chemical Science*, 12(13):4661–4682, 2021.

[178] John R Finnegan, David J Lunn, Oliver EC Gould, Zachary M Hudson, George R Whittell, Mitchell A Winnik, and Ian Manners. Gradient crystallization-driven self-assembly: cylindrical micelles with “patchy” segmented coronas via the coassembly of linear and

brush block copolymers. *Journal of the American Chemical Society*, 136(39):13835–13844, 2014.

[179] Zachary M Hudson, Charlotte E Boott, Matthew E Robinson, Paul A Rupar, Mitchell A Winnik, and Ian Manners. Tailored hierarchical micelle architectures using living crystallization-driven self-assembly in two dimensions. *Nature Chemistry*, 6(10):893–898, 2014.

[180] Maria Inam, Graeme Cambridge, Anaïs Pitto-Barry, Zachary PL Laker, Neil R Wilson, Robert T Mathers, Andrew P Dove, and Rachel K O'Reilly. 1d vs. 2d shape selectivity in the crystallization-driven self-assembly of polylactide block copolymers. *Chemical Science*, 8(6):4223–4230, 2017.

[181] Xiaosong Wang, Gerald Guerin, Hai Wang, Yishan Wang, Ian Manners, and Mitchell A Winnik. Cylindrical block copolymer micelles and co-micelles of controlled length and architecture. *science*, 317(5838):644–647, 2007.

[182] Joe B Gilroy, Torben Gädt, George R Whittell, Laurent Chabanne, John M Mitchels, Robert M Richardson, Mitchell A Winnik, and Ian Manners. Monodisperse cylindrical micelles by crystallization-driven living self-assembly. *Nature Chemistry*, 2(7):566–570, 2010.

[183] Gérald Guérin, Hai Wang, Ian Manners, and Mitchell A Winnik. Fragmentation of fiberlike structures: sonication studies of cylindrical block copolymer micelles and behavioral comparisons to biological fibrils. *Journal of the American Chemical Society*, 130(44):14763–14771, 2008.

[184] Ali Nazemi, Charlotte E Boott, David J Lunn, Jessica Gwyther, Dominic W Hayward, Robert M Richardson, Mitchell A Winnik, and Ian Manners. Monodisperse cylindrical micelles and block comicelles of controlled length in aqueous media. *Journal of the American Chemical Society*, 138(13):4484–4493, 2016.

[185] Torben Gädt, Nga Sze Ieong, Graeme Cambridge, Mitchell A Winnik, and Ian Manners.

Complex and hierarchical micelle architectures from diblock copolymers using living, crystallization-driven polymerizations. *Nature Materials*, 8(2):144–150, 2009.

[186] Huibin Qiu, Yang Gao, Charlotte E Boott, Oliver EC Gould, Robert L Harniman, Mervyn J Miles, Stephen ED Webb, Mitchell A Winnik, and Ian Manners. Uniform patchy and hollow rectangular platelet micelles from crystallizable polymer blends. *Science*, 352(6286):697–701, 2016.

[187] Zaizai Tong, Yujie Xie, Maria C Arno, Yifan Zhang, Ian Manners, Rachel K O'Reilly, and Andrew P Dove. Uniform segmented platelet micelles with compositionally distinct and selectively degradable cores. *Nature Chemistry*, pages 1–8, 2023.

[188] Maria C Arno, Maria Inam, Zachary Coe, Graeme Cambridge, Laura J Macdougall, Robert Keogh, Andrew P Dove, and Rachel K O'Reilly. Precision epitaxy for aqueous 1d and 2d poly (ε-caprolactone) assemblies. *Journal of the American Chemical Society*, 139(46):16980–16985, 2017.

[189] Steven TG Street, Yunxiang He, Xu-Hui Jin, Lorna Hodgson, Paul Verkade, and Ian Manners. Cellular uptake and targeting of low dispersity, dual emissive, segmented block copolymer nanofibers. *Chemical Science*, 11(32):8394–8408, 2020.

[190] Sylvia Ganda, Chin Ken Wong, and Martina H Stenzel. Corona-loading strategies for crystalline particles made by living crystallization-driven self-assembly. *Macromolecules*, 54(14):6662–6669, 2021.

[191] Hongjing Dou, Mei Li, Yan Qiao, Robert Harniman, Xiaoyu Li, Charlotte E Boott, Stephen Mann, and Ian Manners. Higher-order assembly of crystalline cylindrical micelles into membrane-extendable colloidosomes. *Nature Communications*, 8(1):426, 2017.

[192] Maria Inam, Joseph R Jones, Maria M Perez-Madrigal, Maria C Arno, Andrew P Dove, and Rachel K O'Reilly. Controlling the size of two-dimensional polymer platelets for water-in-water emulsifiers. *ACS Central Science*, 4(1):63–70, 2018.

[193] Bin Dong, David L Miller, and Christopher Y Li. Polymer single crystal as magnetically recoverable support for nanocatalysts. *The Journal of Physical Chemistry Letters*, 3(10):1346–1350, 2012.

[194] Judith Schöbel, Christian Hils, Anne Weckwerth, Mathias Schlenk, Carina Bojer, Marc CA Stuart, Josef Breu, Stephan Förster, Andreas Greiner, Matthias Karg, et al. Strategies for the selective loading of patchy worm-like micelles with functional nanoparticles. *Nanoscale*, 10(38):18257–18268, 2018.

[195] Jia Tian, Yifan Zhang, Lili Du, Yunxiang He, Xu-Hui Jin, Samuel Pearce, Jean-Charles Eloi, Robert L Harniman, Dominic Alibhai, Ruquan Ye, et al. Tailored self-assembled photocatalytic nanofibres for visible-light-driven hydrogen production. *Nature Chemistry*, 12(12):1150–1156, 2020.

[196] Xu-Hui Jin, Michael B Price, John R Finnegan, Charlotte E Boott, Johannes M Richter, Akshay Rao, S Matthew Menke, Richard H Friend, George R Whittell, and Ian Manners. Long-range exciton transport in conjugated polymer nanofibers prepared by seeded growth. *Science*, 360(6391):897–900, 2018.

[197] Osama El-Zubir, Emily L Kynaston, Jessica Gwyther, Ali Nazemi, Oliver EC Gould, George R Whittell, Benjamin R Horrocks, Ian Manners, and Andrew Houlton. Bottom-up device fabrication via the seeded growth of polymer-based nanowires. *Chemical Science*, 11(24):6222–6228, 2020.

[198] Zachary M Hudson, David J Lunn, Mitchell A Winnik, and Ian Manners. Colour-tunable fluorescent multiblock micelles. *Nature communications*, 5(1):3372, 2014.

[199] Xiaoyu Li, Yang Gao, Charlotte E Boott, Dominic W Hayward, Robert Harniman, George R Whittell, Robert M Richardson, Mitchell A Winnik, and Ian Manners. “cross” supermicelles via the hierarchical assembly of amphiphilic cylindrical triblock comicelles. *Journal of the American Chemical Society*, 138(12):4087–4095, 2016.

[200] Wei-Na He, Bing Zhou, Jun-Ting Xu, Bin-Yang Du, and Zhi-Qiang Fan. Two growth

modes of semicrystalline cylindrical poly (ε-caprolactone)-b-poly (ethylene oxide) micelles. *Macromolecules*, 45(24):9768–9778, 2012.

[201] Charlotte E Boott, Erin M Leitao, Dominic W Hayward, Romain F Laine, Pierre Mahou, Gerald Guerin, Mitchell A Winnik, Robert M Richardson, Clemens F Kaminski, George R Whittell, et al. Probing the growth kinetics for the formation of uniform 1d block copolymer nanoparticles by living crystallization-driven self-assembly. *ACS Nano*, 12(9):8920–8933, 2018.

[202] Robert L Harniman, Samuel Pearce, and Ian Manners. Exploring the "living" growth of block copolymer nanofibers from surface-confined seeds by in situ solution-phase atomic force microscopy. *Journal of the American Chemical Society*, 144(2):951–962, 2022.

[203] Sanghee Yang and Tae-Lim Choi. Rapid formation and real-time observation of micron-sized conjugated nanofibers with tunable lengths and widths in 20 minutes by living crystallization-driven self-assembly. *Chemical Science*, 11(32):8416–8424, 2020.

[204] Jiangping Xu, Hang Zhou, Qing Yu, Ian Manners, and Mitchell A Winnik. Competitive self-assembly kinetics as a route to control the morphology of core-crystalline cylindrical micelles. *Journal of the American Chemical Society*, 140(7):2619–2628, 2018.

[205] Sanghee Yang, Sung-Yun Kang, and Tae-Lim Choi. Semi-conducting 2d rectangles with tunable length via uniaxial living crystallization-driven self-assembly of homopolymer. *Nature Communications*, 12(1):2602, 2021.

[206] Charlotte E Boott, Romain F Laine, Pierre Mahou, John R Finnegan, Erin M Leitao, Stephen ED Webb, Clemens F Kaminski, and Ian Manners. In situ visualization of block copolymer self-assembly in organic media by super-resolution fluorescence microscopy. *Chemistry–A European Journal*, 21(51):18539–18542, 2015.

[207] Rees F Garmann, Aaron M Goldfain, and Vinothan N Manoharan. Measurements of the self-assembly kinetics of individual viral capsids around their rna genome. *Proceedings of the National Academy of Sciences*, 116(45):22485–22490, 2019.

[208] Maria A Lebedeva, Elena Palmieri, Philipp Kukura, and Stephen P Fletcher. Emergence and rearrangement of dynamic supramolecular aggregates visualized by interferometric scattering microscopy. *ACS Nano*, 14(9):11160–11168, 2020.

[209] Xu Zhang, Guanhao Chen, Bowen Zheng, Zhengwei Wan, Liping Liu, Lingyuan Zhu, Yujie Xie, and Zaizai Tong. Uniform two-dimensional crystalline platelets with tailored compositions for ph stimulus-responsive drug release. *Biomacromolecules*, 24(2):1032–1041, 2023.

[210] Jing Wang, Yan Lu, and Yongming Chen. Fabrication of 2d surface-functional polymer platelets via crystallization-driven self-assembly of poly (ε-caprolactone)-contained block copolymers. *Polymer*, 160:196–203, 2019.

[211] Renhua Deng, Xi Mao, Samuel Pearce, Jia Tian, Yifan Zhang, and Ian Manners. Role of competitive crystallization kinetics in the formation of 2d platelets with distinct coronal surface patterns via seeded growth. *Journal of the American Chemical Society*, 144(41):19051–19059, 2022.

[212] Georgios Rizis, Theo GM van de Ven, and Adi Eisenberg. "raft" formation by two-dimensional self-assembly of block copolymer rod micelles in aqueous solution. *Angewandte Chemie*, 126(34):9146–9149, 2014.

[213] Yujie Xie, Jonathan T Husband, Miquel Torrent-Sucarrat, Huan Yang, Weisheng Liu, and Rachel K O'Reilly. Rational design of substituted maleimide dyes with tunable fluorescence and solvafluorochromism. *Chemical Communications*, 54(27):3339–3342, 2018.

[214] Johannes Schindelin, Ignacio Arganda-Carreras, Erwin Frise, Verena Kaynig, Mark Longair, Tobias Pietzsch, Stephan Preibisch, Curtis Rueden, Stephan Saalfeld, Benjamin Schmid, et al. Fiji: an open-source platform for biological-image analysis. *Nature Methods*, 9(7):676–682, 2012.

[215] Chengyan Zhang, Jiaping Lin, Liquan Wang, and Liang Gao. 2d liquid-crystallization-driven self-assembly of rod–coil block copolymers: Living growth and self-similarity. *The Journal of Physical Chemistry Letters*, 13(26):6215–6222, 2022.

[216] Bin Fan, Rui-Yang Wang, Xiang-Yue Wang, Jun-Ting Xu, Bin-Yang Du, and Zhi-Qiang Fan. Crystallization-driven co-assembly of micrometric polymer hybrid single crystals and nanometric crystalline micelles. *Macromolecules*, 50(5):2006–2015, 2017.

[217] Zhen Li, Yufei Zhang, Libin Wu, Wei Yu, Thomas R Wilks, Andrew P Dove, Hong-ming Ding, Rachel K O'Reilly, Guosong Chen, and Ming Jiang. Glyco-platelets with controlled morphologies via crystallization-driven self-assembly and their shape-dependent interplay with macrophages. *ACS Macro Letters*, 8(5):596–602, 2019.

[218] Keith J Mickolajczyk, Elisabeth Geyer, Tae Kim, Luke Rice, and William O Hancock. Direct observation of individual tubulin dimers binding to growing microtubules. *Biophysical Journal*, 116(3):156a–157a, 2019.

[219] Felix Ritort. Single-molecule experiments in biological physics: methods and applications. *Journal of Physics: Condensed Matter*, 18(32):R531, 2006.

[220] Mark C Leake. The physics of life: one molecule at a time, 2013.

[221] Sivaraman Subramanian, Hsin-Yu Wu, Tom Constant, Jolly Xavier, and Frank Vollmer. Label-free optical single-molecule micro-and nanosensors. *Advanced Materials*, 30(51):1801246, 2018.

[222] André Gemeinhardt, Matthew P McDonald, Katharina König, Michael Aigner, Andreas Mackensen, and Vahid Sandoghdar. Label-free imaging of single proteins secreted from living cells via iscat microscopy. *JoVE (Journal of Visualized Experiments)*, (141):e58486, 2018.

[223] Helge Ewers, Volker Jacobsen, Enrico Klotzsch, Alicia E Smith, Ari Helenius, and Vahid Sandoghdar. Label-free optical detection and tracking of single virions bound to their receptors in supported membrane bilayers. *Nano Letters*, 7(8):2263–2266, 2007.

[224] Susann Spindler, Jeremias Sibold, Reza Gholami Mahmoodabadi, Claudia Steinem, and Vahid Sandoghdar. High-speed microscopy of diffusion in pore-spanning lipid membranes. *Nano Letters*, 18(8):5262–5271, 2018.

[225] Daniel Cole, Gavin Young, Alexander Weigel, Aleksandar Sebesta, and Philipp Kukura. Label-free single-molecule imaging with numerical-aperture-shaped interferometric scattering microscopy. *ACS Photonics*, 4(2):211–216, 2017.

Appendix

Movie S1

Raw data of AuNP growth monitored by iSCAT microscopy. As NPs grow, they are first detected with contrast more negative than the overall background (dark spots) before becoming positive (bright spots). We also observed that for some particles, as the particle becomes very large, the AuNP detaches from the surface. 0.4 mM $HAuCl_4$ and 1 mM citrate were used (scale bar 2 µm). A laser power density of 3 µW $µm^{-2}$ at 637 nm, a camera exposure time of 220 µs, and an overall time-lapsed frame rate of 1 s^{-1} were chosen. This movie corresponds to the data in Fig. 4.6 and Fig. 4.7.

Movie S2

Raw movie of platelet growth monitored by iSCAT microscopy (scale bar: 3 µm). A 50 µL 0.1 µg mL^{-1} seed solution was spin-coated onto a cleaned coverslip (3200 rpm for 50s followed by 4000 rpm for 30s). PCL_{45}:PCL_{45}-b-$PDMA_{348}$ blends in THF were then diluted with methanol to achieve a final concentration of 3.03 µg mL^{-1}. 150 µL unimer methanol solution was added onto the seeds-coated surface and iSCAT observation started immediately. A laser power density of 2 µW $µm^{-2}$ at 637 nm, a camera exposure time of 800 µs, and an overall time-lapsed frame rate of 1.5 s^{-1} were chosen. This movie corresponds to the data in Fig. 5.4.

Movie S3

Raw data of three-layered platelet growth monitored by iSCAT microscopy (scale bar: 2 µm). 50 µL 0.1 µg mL^{-1} seed solution was spin-coated onto the cleaned coverslip twice (3200 rpm for 50 s followed by 4000 rpm for 30 s). PCL_{45}:PCL_{45}-b-$PDMA_{348}$ blends methanol solution was added sequentially with concentration of 4.17, 5.56 and 8.33 µg mL^{-1} for each layer. A laser power density of 4 µW $µm^{-2}$ at 637 nm, a camera exposure time of 400 µs, and an overall time-lapsed frame rate of 1 s^{-1} were chosen. This movie corresponds to the data in Fig. 5.9.

Movie S4

Raw data of four-layered platelet growth monitored by iSCAT microscopy (scale bar: 2 µm). 50 µL 0.1 µg mL^{-1} seed solution was spin-coated onto the cleaned coverslip twice (3200 rpm for 50s followed by 4000 rpm for 30s). Layer 1: 150 µL 1.67 µg mL^{-1} PCL$_{45}$:PCL$_{45}$-*b*-PDMA$_{348}$ methanol solution; Layer 2: 150 µL 2.08 µg mL^{-1} PCL$_{45}$ unimer methanol solution; Layer 3: 150 µL 3.33 µg mL^{-1} PCL$_{45}$:PCL$_{45}$-*b*-PDMA$_{348}$ methanol solution; Layer 4: 150 µL 4.17 µg mL^{-1} PCL$_{45}$ unimer methanol solution. A laser power density of 4 µW µm^{-2} at 637 nm, a camera exposure time of 400 µs, and an overall time-lapsed frame rate of 1 s^{-1} were chosen. This movie corresponds to the data in Fig. 5.11.